WIND-BLOWN SAND: THRESHOLD OF MOTION

A Dissertation

by

CHRISTY MICHELLE SWANN

Submitted to the Office of Graduate and Professional Studies of
Texas A&M University
in partial fulfillment of the requirements for the degree of

DOCTOR OF PHILOSOPHY

Chair of Committee,	Douglas J. Sherman
Co-Chair of Committee,	Christopher Houser
Committee Members,	Vatche Tchakerian
	Steve DiMarco
Head of Department,	David Cairns

December 2014

Major Subject: Geography

ABSTRACT

The fluid threshold for wind-blown sand is the minimum shear velocity required to initiate grain movement by the force of the wind alone, and is used to predict dust emission and landform change in sandy environments. R.A. Bagnold derived the most commonly cited model of the threshold from a set of wind tunnel experiments. He visually observed the fluid threshold by measuring flow conditions corresponding to the initiation of bedload movement, a mode of transport that occurs prior to saltation. His model was developed using unimodal grain size populations and requires only the average size to predict the threshold. However, field environments often exhibit non-unimodal surface populations. The fluid threshold for mixed size surfaces in fluvial environments corresponds to the coarsest grain size, not the average, resulting in a larger threshold shear velocity to initiate movement. Larger thresholds yield smaller transport rates and could explain the consistent over-prediction of aeolian transport models. Yet, the fluid threshold of mixed size sands has not been tested in an aeolian field environment. This is due to the previous inability to separate the bedload from saltation.

The purpose of this research is to test Bagnold's model of the fluid threshold in a field environment composed of dry, naturally mixed grain sizes in Jericoacoara, Brazil. A bedload trap was designed to separate bedload from saltation, and the initiation of bedload and near surface flow conditions were measured simultaneously. Field observations were compared to Bagnold's model as well as other models of the fluid threshold.

Observed fluid thresholds did not vary with average grain size for the mixed size population. The thresholds for finer and coarser bedload samples were approximately equal to the Bagnold-predicted threshold for coarser grains. All models tested under predicted the threshold for finer grains. These results suggest the fluid threshold for mixed size sands corresponds to the coarsest grain size fraction, similar to the results found in fluvial

environments. Threshold shear velocity predicted using the coarsest grain size will result in smaller predicted transport rates and may reduce the over prediction typically found in aeolian field environments.

DEDICATION

To my niece Layna, my nephew Bladen, and all curious minds -

may life take you to the most unexpected of places and exploration always be in your feet

ACKNOWLEDGEMENTS

TABLE OF CONTENTS

LIST OF FIGURES

LIST OF TABLES

CHAPTER I

INTRODUCTION

1.1 Research statement

The purpose of this research is to test Bagnold's (1936) model of the fluid threshold on an open-air surface composed of a mixed size grain population. Bagnold's model is compared to field observations measured under relatively simple surface conditions (e.g. dry, flat and without vegetation) in Jericoacoara, Brazil. Field observations are also compared to the models of Fletcher (1976), Greeley and Iversen (1985), Nickling (1988), Shao and Lu (2000), and Kok and Renno (2006) in addition to a model developed in this study. The results of this work will highlight potential errors in the fluid threshold that may contribute to the over prediction of transport rates in field environments.

1.2 Conceptual framework and significance

The threshold of motion for wind-blown sand marks the point at which particles on a sandy surface are initiated by the force of the wind (Bagnold, 1936, 1937a, 1937b; Shields, 1936; Chepil, 1945a, 1945b; Kawamura, 1951; Belly, 1964; Greeley and Iversen, 1985). This threshold is critical to environmental, anthropogenic and geomorphic processes on Earth and/or other planetary bodies (e.g. Mars, Venus, and Titan). Two overarching processes describe the criticality of the threshold: (1) dust emission and (2) landform change over time.

Dust emissions are largely generated from aeolian saltation (Gillette et al., 1974; Gillette, 1979; Shao et al., 1993; Andreae, 1996; Marticorena et al., 1997; Kok and Renno, 2008), a process only occurring once the fluid threshold for wind-blown sand has been exceeded. At that point, saltating particles bombard the surface breaking conglomerates of dust particles.

Dust particles are subsequently suspended for days to weeks, and potentially years (Andreae, 1996). Dust emissions make up the largest portion of tropospheric aerosols, causing backscattering and absorbing solar radiation (Andreae, 1996; Schönfeldt, 2004; Tegen et al., 2004; Kok and Renno, 2008). This has recently raised concerns regarding global climate fluctuations, specifically the unknown heating/cooling effects from dust aerosols and the potential onset of desertification (Andreae, 1996; Marticorena et al., 1997). In these scenarios, the threshold of motion is used to predict the frequency and intensity of dust emissions for future climate scenarios (Tegen et al., 2004; Kurosaki and Mikami, 2007) and balance global energy budgets (Andreae, 1996). In addition to global climatic fluctuations, dust emissions pose a public health hazard as the suspension of particulate matter often surpasses US-EPA National Ambient Air Quality Standards and EU Limit Values for Air Quality (Ozer et al., 2006). To monitor and forecast public health concerns, the threshold is often used to quantify reductions in air quality at a local and regional scale (Draxler et al., 2001).

The threshold of motion is also fundamental to predicting landform change over time in both natural and developed sandy environments. Landform change is largely predicated on the gradient of transport and transport models often incorporate the threshold in the form of threshold shear velocity (Bagnold, 1936; Fletcher, 1976; Greeley and Iversen, 1985; Nickling, 1988; Shao and Lu, 2000; Kok and Renno, 2006) or threshold wind speed (Stout and Zobeck, 1997; Schönfeldt, 2004; Davidson-Arnott et al., 2005; Barchyn and Hugenholtz, 2010) to predict: dune mobility and migration (Fryberger and Dean, 1979; Thomas et al., 2005; Lorenz et al., 2006), coastal dune dynamics (Davidson-Arnott et al., 2005; Bauer et al., 2009), and/or erosion of agricultural fields (Chepil, 1945a, 1945b; Gillette, 1988; Zobeck and van Pelt, 2006). Transport models use an exponential function of the threshold shear velocity (Bagnold, 1936;

Kawamura, 1951; Owen, 1964; Lettau and Lettau, 1977), and as a result, small errors in threshold shear velocity result in large errors in model predictions.

Most models over predict the observed rate of transport in field environments (Sherman et al., 1998; Dong et. al., 2003; Sherman et al., 2011). Sherman et al. (1996) compared field observations to the most commonly cited transport models (Bagnold, 1936, 1937a; Kawamura, 1951; Zingg, 1953; Kadib, 1965; Lettau & Lettau, 1977) and found discrepancies on the order of 300% within each model, and up to 700% between Bagnold (1937a), Lettau and Lettau (1977), and Kawamura (1951). The largest differences between predicted and observed transport rates occur at the early stages of transport and have been attributed to errors in the threshold of motion (Ellis and Sherman, 2013).

Models predicting the threshold for wind-blown sand in natural environments are rooted in the original wind tunnel work of Bagnold (1936). He introduced an empirically-calibrated model of the threshold using shear velocity, u_*: a height independent variable that represents the momentum transfer from the boundary layer to the surface. Modeling the threshold using shear velocity provided Bagnold with a universally-applicable, height independent variable characterizing the boundary layer conditions necessary to set particles into motion. Using visual observations of particle entrainment, Bagnold resolved the threshold shear velocity, u_{*t}, required to initiate grain movement:

$$u_{*t} = A \sqrt{gd \left(\frac{\rho_s - \rho}{\rho} \right)} \tag{1}$$

where g is the gravitational constant, d is the average grain size, and ρ_s and ρ are the densities of the grain and air, respectively. Threshold shear velocity is the shear velocity required to entrain particles by the fluid alone (coined the 'fluid' or 'static' threshold where $A = 0.1$), or sustain movement from both the fluid force and the impact of other grains (referred to as the 'impact' or 'dynamic' threshold where $A = 0.08$). However, fundamental discrepancies are

embedded in the methods, deduction, and interpretation of Bagnold's threshold experiments. For example, some of the more critical methodological errors include the inability to separate bedload from saltation, Bagnold's visual demarcation of the threshold, the use of an unknown number of velocity profiles to derive shear velocity, inconsistent derivation of the A parameter, and Lagrangian spatial averaging of non-simultaneous velocities.

When tested in wind tunnels, Bagnold's model of the fluid threshold under predicts the threshold shear velocity necessary to move particles by the fluid alone (Chepil, 1945b; Lyles and Krauss, 1971; Nickling, 1988; Dong et al., 2003), with the greatest discrepancy between 45-75% of observed shear velocities (Lyles and Krauss, 1971; Dong et al., 2003) (Figure 1). In these experiments, the A parameter varies by -10% to 100% of Bagnold's $A = 0.1$ (Chepil, 1945b; Lyles & Krauss, 1971; Nickling, 1988; Dong et al., 2003) (Figure 2). These studies suggest the fluid threshold shear velocity is larger than Bagnold's (1936) model. Similar results have been found in fluvial settings where the fluid threshold of a mixed grain population corresponds to the largest size fraction and the threshold for the finer grain fractions are considerably under predicted (Parker and Klingeman, 1982; Wiberg and Smith, 1982; Wilcock, 1988; Wilcock, 1993). This phenomenon in fluvial literature is referred to as the equal mobility concept. A larger predicted threshold shear velocity would decrease predicted transport rates and reduce over prediction at the early stages of movement.

Prior to this work, bedload transport had not been captured separately from saltation. The inability to separate bedload from saltation precluded testing of Bagnold's model in a field environment. Additionally, field environments are often made up of mixed size grain populations. The aim of this research is to test Bagnold's model under relatively simple field conditions with a mixed size grain population. This research directly measures bedload

transport and boundary layer conditions to test Bagnold's model of the fluid threshold in a field environment composed of naturally mixed sand.
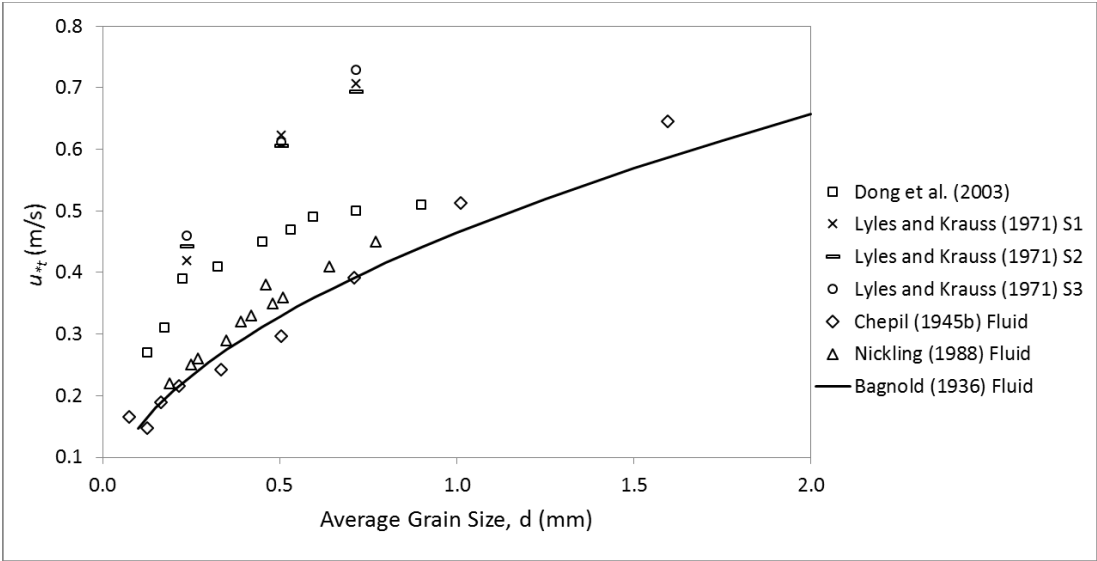
Figure 1: Threshold shear velocity plotted against average grain diameter for wind tunnel experiments observing the fluid threshold.
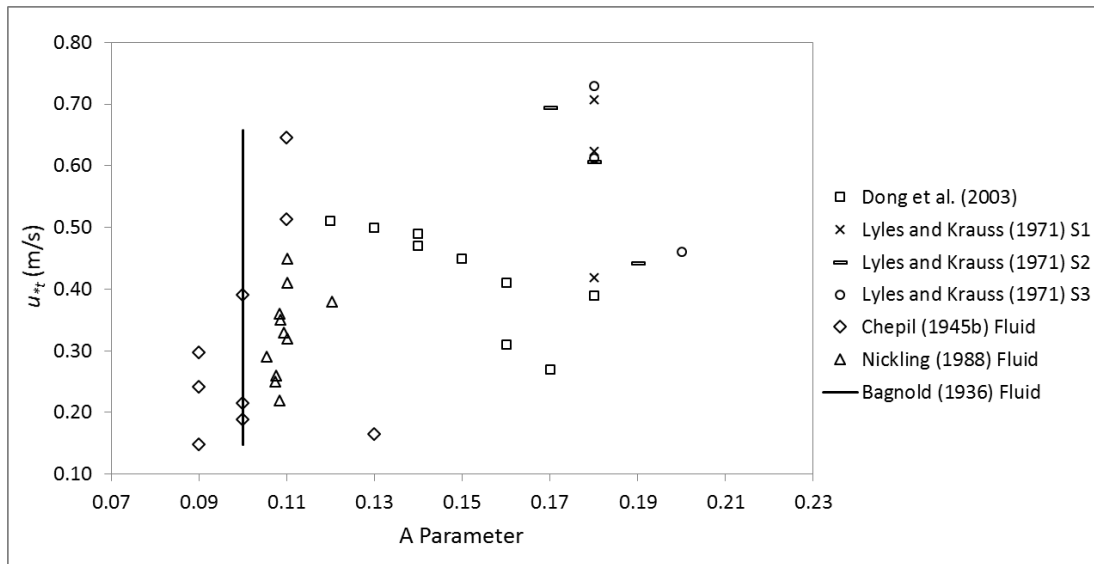
Figure 2: Threshold shear velocity plotted against Bagnold's (1936) *A* constant showing significant discrepancy between selected studies.

1.3 Research hypotheses and objectives

The following hypotheses will be tested in order to test Bagnold's (1936) model of the fluid threshold in a field environment:

I.   Bagnold's (1936) predicted fluid threshold shear velocity is not equivalent to observed threshold shear velocity at the initiation of bedload on a surface with a mixed size grain population

II.   Bagnold's (1936) *A* is not 0.1 at the initiation of bedload on a surface with a mixed size grain population

The following objectives must be completed to test the hypotheses:

I.   Identify a bare, flat, dry sandy surface with a mixed size grain population and wind speeds below and above the fluid threshold of motion

II.   Obtain field observations of bedload transport and near surface flow conditions

III.   Calculate threshold shear velocity from wind observations corresponding to the initiation of bedload

IV.   Evaluate the A parameter using observed fluid threshold shear velocities by rearranging Equation 1 to solve for A:

$$A = \frac{u_{*t}}{\sqrt{gd\left(\frac{\rho_s - \rho}{\rho}\right)}} \tag{2}$$

V.   Compare Bagnold's (1936) fluid u_{*t} to observed u_{*t}

VI.   Develop a model of the fluid threshold shear velocity based on observations and bedload grain size distribution characteristics

VII.   Compare field observations of the fluid threshold to the model developed in Objective VI, Bagnold (1936) and the models of Fletcher (1976), Greeley and Iversen (1985), Nickling (1988), Shao and Lu (2000) and Kok and Renno (2006)

CHAPTER II

LITERATURE REVIEW

Predicting the transport rate, Q, over a flat surface of dry, cohesionless sand requires only the average grain size and shear velocity. Above the threshold these variables are used in transport models (Table 1) to predict the rate of sand movement, and u_{*t} is often incorporated as an exponential function. However, significant discrepancies have been found between predicted and observed transport rates (Sherman et al., 1996, 1998; Dong et al., 2003; Sherman et al., 2011; Ellis and Sherman, 2013). Field-based studies have focused on increasing the predictive power of transport models by uncovering errors between predicted and observed rates (Li et al., 2010; Sherman et al., 2011, 2013a). These studies have decreased the discrepancy between predicted and observed Q by using recalibrated coefficients, *C'$_K$ and C'$_{KA}$*. Sherman et al. (2013) recalibrated model coefficients and successfully reduced root mean squared errors in transport models by an order of magnitude. In addition to recalibration of model coefficients, Bauer et al. (1992) elucidated errors associated with the derivation of shear velocity and found a 10% discrepancy in u_* can result in 30% error in model prediction. They suggest using statistically significant velocity profiles ($\rho < 0.01$) with $r^2 > 0.98$ to reduce error. Yet even with these steps to reduce error, the largest discrepancies occur at small transport rates (Ellis and Sherman, 2013). The following sections describe near surface airflow and the resulting forces acting on a particle, inconsistency in the definition of the fluid threshold, and Bagnold's (1936) derivation of threshold shear velocity.

Table 1 Aeolian sand transport models that incorporate threshold shear velocity

Reference	Transport Model	Values of Coefficients		
		C	[ff] C'_K	[ff] C'_{KA}
Kawamura (1951)	$Q = C \dfrac{\rho}{g}(u_* - u_{*t})(u_* + u_{*t})^2$	2.78	0.70	1.27
Owen (1964)	$Q = \left(C + \dfrac{\omega}{3u_*}\right)\left(1 - \dfrac{u_{*t}^2}{u_*^2}\right)\left(\dfrac{\rho u_*^3}{g}\right)$	0.25	0.21	0.34
Lettau and Lettau (1977)	$Q = C \sqrt{\dfrac{d}{D}} \dfrac{\rho}{g}(u_* - u_{*t})u_*^2$	6.7[†]	1.20	2.47
Sørensen (1991)	$Q = C\rho u_*(u_* - u_{*t})(u_* + 7.6u_{*t} + 205)$	0.0014	-	-
C is a coefficient specific to each individual model, D is a reference grain diameter, typically 0.25 mm from Bagnold (1936) and ω is the fall velocity of a sand particle. [†] Universal constant for sands as reported by Sherman et al. (2013a) [re]Recalibrated values are from Sherman et al. (2013a)				

2.1 Thresholds in aeolian sand transport

2.1.1 Near surface airflow

Nearly all open-air flows are turbulent. As a fluid flows over a surface, the fluid undergoes a horizontal and vertical deformation imparted by the frictional resistance of the surface (Prandtl, 1925; Stull, 1988). The vertical deformation extends logarithmically from the

surface, where fluid velocity is zero, to a transition point where the fluid is no longer affected by the friction from the surface. This turbulent region of airflow is the boundary layer.

Within the boundary layer there are two overlapping zones: an inner (closer to the surface) layer and an outer (closer to free stream velocity) layer. The inner layer can be further subdivided into three regions: a viscous sublayer, a turbulence-generation layer, and an outer region (Middleton and Southard, 1978; Bauer et al., 1992). The viscous sub-layer is immediately adjacent to the solid boundary and dominated by viscosity-shearing flow. This layer ranges in thickness from a fraction of a millimeter to a few millimeters thick and has compressed, laminar-like flow (Middleton and Southard, 1978; Greeley and Iversen, 1985). This region was once called the 'laminar sub-layer', but significant viscosity-driven stress and velocity fluctuations frequently exist, hence the currently accepted terminology, viscous sub-layer. Immediately above the viscous sublayer, turbulent structures begin to form from strong shearing forces. This marks the turbulence-generation, or 'buffer' layer. In this region, fluid shear generates small turbulent eddies. Horizontal shearing planes lower in elevation and speed constantly exchange equal and opposite forces with adjacent, faster, higher in elevation shearing planes (Middleton and Southard 1978). Here, the slope of the vertical velocity profile is logarithmic. This interaction, occurring from the outer region to the viscous sublayer (when present) transfers fluid momentum towards the surface. Shear stress imparts the net fluid force to particles resting on the surface via shearing within the boundary layer (Bauer et al., 1992). Once the fluid force exceeds the resisting forces holding the particles in place, particles begin to move.

Characterizing shear stress imparted on surface particles requires knowledge concerning the degree of vertical deformation in the boundary layer and can be measured using velocity profiles. Steeper velocity profiles indicate a greater shear stress. However, it is difficult to measure shear stress on the surface and shear velocity is used as a surrogate for τ:

$$u_* \equiv \sqrt{\frac{\tau}{\rho}}$$ (3)

Shear velocity can be derived from the velocity profile above the viscous sub-layer that is characterized using the von Kármán-Prandtl model of flow over a solid boundary, known as the Law-of-the-Wall:

$$\frac{u_z}{u_*} = \frac{1}{K} \log\left(\frac{z}{z_0}\right)$$ (4)

where u is the velocity of the fluid at height z and K is the von Kármán constant of 0.4. The roughness length, z_0, is found by extrapolating the velocity profile to zero.

2.1.2 Forces on a particle

The fluid forces exerted on any given particle at rest are governed by the type of flow around a particle. Osborne Reynolds characterized the motion of a fluid using the Reynolds number, Re (Reynolds, 1883):

$$Re = \frac{ul}{\nu}$$ (5)

where ν is the kinematic viscosity and l is a characteristic length which was originally derived based on pipe diameter, but for fluvial transport studies was adapted to the depth of a river channel. A second type of Reynolds number was derived to characterize the small turbulent eddies generated on the lee side of a particle, the particle Reynolds number, Re_p:

$$Re_p = \frac{u_* d}{\nu}$$ (6)

At small particle Reynolds numbers ($Re_p < 3.5$), flow is laminar and lacks the momentum to create significant pressure differences between the windward and lee sides of a particle (Figure 3a). Nearly all flows involving the movement of sand particles are turbulent (Bagnold, 1936; Shields, 1936) and are characterized by large Reynolds numbers, ($Re_p > 3.5$).

Two fluid forces arise from turbulent flow moving over a particle (Figure 3c): drag, F_D, and lift, F_L. Fluid drag is a result of the pressure difference around a particle in turbulent flow (Figure 3c). The drag force is a function of the wind velocity and the particle's cross-sectional area exposed to flow, A_1:

$$F_D = \frac{1}{2}\rho u^2 C_D A_1 \tag{7}$$

where C_D is a drag coefficient. C_D is a dimensionless number depending on the resistance of a particle to the fluid:

$$C_D = \frac{2F_D}{\rho u^2 A_1} \tag{8}$$

The pressure difference between the upwind and downwind face of a particle increases with area exposed to flow, and results in an increase in the fluid drag acting on a particle, (Figure 3b). Lift arises from pressure differences between the base and top of the particle. A lower pressure (relative to the base) develops at the top and leeward side of a particle as a flow moves over it. This creates a pressure gradient extending upwards from the base of the particle, hence the term 'lift'. Lift varies with flow condition (Einstein and El-Samni 1949; Coleman 1979). As particle Reynolds numbers increase, lift increases, becoming almost equivalent to drag; Chepil (1961) found lift to account for 75% of the drag force on average when acting on a (gravel) particle at rest. However, the lift force is not fully understood in relation to the initiation of sand size particles and is often disregarded in threshold derivations.

The moment of fluid forces (lift and drag) must be equal to the moment of resisting forces (gravity, interparticle forces) holding the particle in place for a particle to pivot about neighbors (Bagnold, 1936; Middleton and Southard, 1978; Kok et al., 2012) . Gravitational forces act through the center of the particle (Figure 3c). Based on sediment density and gravitational forces, the overall specific gravity of the grain is the most limiting factor in transport conditions of dry, cohesionless particles.
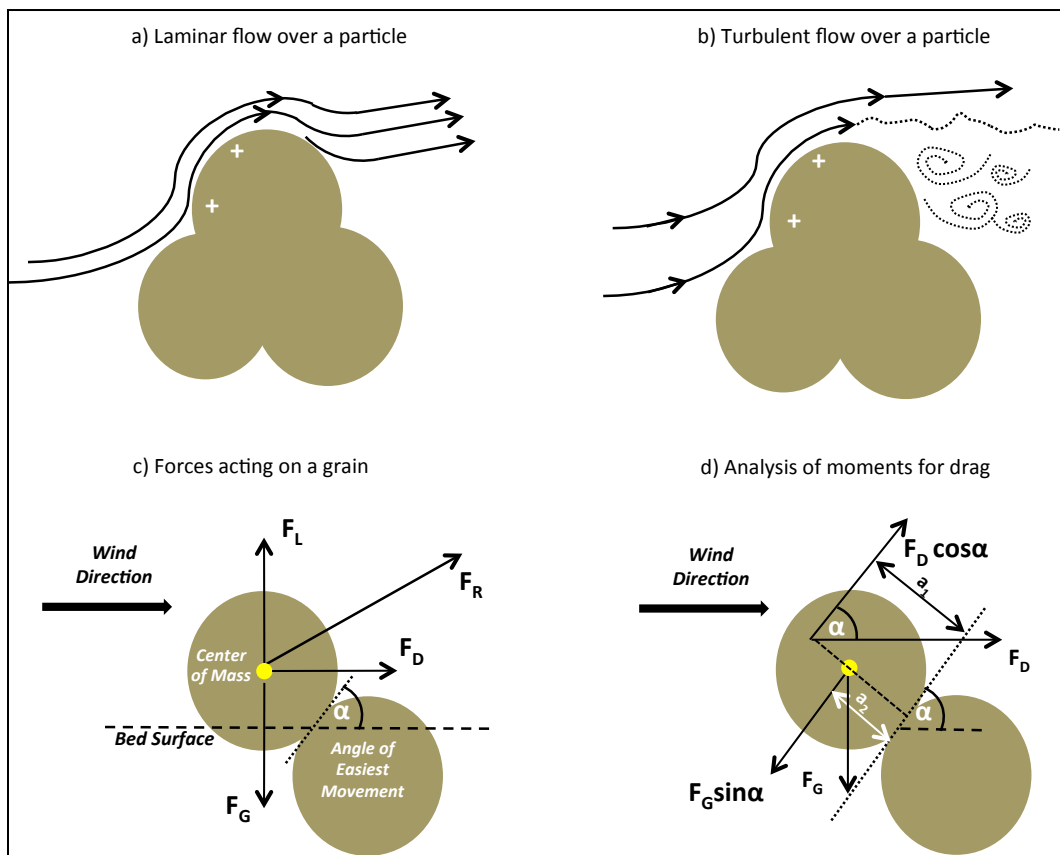
Figure 3: Flow around a particle: a) laminar flow over a particle $\left(Re_p < 5\right)$, b) turbulent flow over a particle $\left(Re_p < 70\right)$, c) forces acting on a dry, cohesionless particle, and d) analysis of moments for drag about a particle. Modified from Middleton and Southard (1978).

Recent work has shown interparticle forces play an important role in the threshold of motion (Iversen et al., 1976; Kok and Renno, 2008; Duan et al., 2013; Massey, 2013), but are often disregarded in threshold derivations. Three distinct interparticle forces may be involved in particle entrainment: van der Waal's force, electrostatics and cohesion. The van der Waal force describes the attractions (and repulsions in rare cases) between neighboring bodies of a known volume (Hamaker,1937; Cornelis and Gabriels 2004). The total van der Waal force can be found by summing all interatomic/intermolecular parts of two adjacent sand particles. A linear relationship with particle size and distance between two particles (Hamaker, 1937; Langbein, 1970; Kok et al., 2012) determines the magnitude of this force. However, van der Waal's forces are typically assumed negligible and not included in many threshold studies.

Electrostatic forces arise from two particles in rubbing contact (Corenlis and Gabriels, 2004; Kok and Renno, 2008) causing an electrically charged attraction or repulsion between the two particles. The distance between and charge of each particle determines the magnitude of the electrostatic force. However, saltation is needed for the electric field to substantially influence sand entrainment which does not occur at the initiation of bedload (Duan et al., 2013).

The third interparticle force is brought about by the cohesive bonds between moisture films coating a particle (Belly, 1964; Iversen and White, 1982; McKenna-Neuman and Nickling, 1989; Wiggs et al., 2004a). Field experiments have shown variability in moisture content that strongly inhibit transport. Surfaces with moisture content exceeding 4-6% significantly reduce transport via fluid forces alone (Sarre, 1988; Sherman et al., 1998; Wiggs et al., 2004a). Recent work found threshold shear velocity doubles for sand with 0.6% moisture content (Ellis and Sherman, 2013).

For the simplest case, excluding lift and extraneous forces for a dry cohesionless particle, we can balance the moments of drag and gravitational forces acting on a particle (Shields, 1936):

$$a_1(F_G sin\alpha) = a_2(F_D cos\alpha) \tag{9}$$

where

$$F_G = c_1 d^3 g(\rho_s - \rho) \tag{10}$$

and

$$F_D = c_2 d^2 \tau_0 \tag{11}$$

where α is the angle of easiest movement (Figure 3d), c_1 and c_2 are coefficients accounting for particle shape, packing, and geometry (Shields, 1936). a_1 and a_2 are moment arm lengths between the pivoting axis and the line of movement. Substituting Equations 10 and-11 into Equation 9 and replacing τ_0 with τ_c for the threshold of motion, gives:

$$a_1 c_1 d^3 g(\rho_s - \rho)sin\alpha = a_2 c_2 d^2 \tau_c cos\alpha \tag{12}$$

Solving for the critical shear stress yields:

$$\tau_c = \frac{a_1 c_1}{a_2 c_2} dg(\rho_s - \rho) \, tan\alpha \tag{13}$$

Dividing both sides of Equation (13) by $dg(\rho_s - \rho)$, we arrive at Shields' dimensionless critical threshold parameter, β:

$$\beta = \frac{\tau_c}{dg(\rho_s - \rho)} = \frac{a_1 c_1}{a_2 c_2} \tan\alpha \qquad (14)$$

The Shields' parameter set the foundation for the threshold of motion in fluvial environments, and to some degree, aeolian environments, as Bagnold (1936) references Shields' work in his threshold derivation. Bagnold's A coefficient is the square root of β, and both vary with particle Reynolds number.

Particle shape, pivoting angle, and degree of exposure can also alter the threshold required to initiate grain movement (Shields, 1936; Miller et al., 1977; Wiberg and Smith, 1987; Wilcock, 1988; Duan et al., 2013). Differences in shape and size can either increase or decrease the probability of entrainment (Wiberg and Smith, 1987). Particles with less angularity (or more sphericity) on loosely packed surfaces are more conducive to incipient motion (Buffington and Montgomery, 1997). Conversely, greater angularity and increased sorting requires a greater shear velocity for particle entrainment. Additionally, particles with lower (higher) pivoting angles and larger (smaller) exposed areas are more (less) susceptible to fluid forces and correspond to a lower (greater) threshold shear velocity (Miller et al., 1977; Wiberg and Smith, 1987; Wilcock, 1988). However, modification of threshold shear velocity from particle shape, pivoting angle and degree of exposure is largely dependent upon the grain population. One example of this is the fluvial concept of equal mobility.

The equal mobility concept maintains that the initiation of grain movement for any grain in a mixed size population corresponds to the threshold of the largest fraction (Parker and

Klingeman, 1982; Wiberg and Smith, 1987; Wilcock, 1988; Wilcock and Southard, 1988; Wilcock, 1993). For instance, a particle in a unimodal grain size distribution will have similar pivoting angles and degrees of exposure to its neighbors requiring a similar threshold to initiate grain movement. Consequently, threshold shear velocity increases with the average size in unimodal populations (Bagnold, 1936). However, in a bimodal grain size distribution coarser (finer) particles have a lower (higher) pivoting angle than the surrounding finer (coarser) particles. This makes coarser (finer) particles more (less) susceptible to fluid forces and easier (more difficult) to roll over a surface of finer (coarser) particles (Wiberg and Smith, 1987). Consequently, the threshold shear velocity required to initiate grain movement of the smaller fraction in a bimodal distribution may be greater than the threshold shear velocity for the same size fraction in a unimodal distribution. This is contrary to current aeolian models that quantitatively define the threshold as a function of the average grain size despite the distribution.

2.1.3 Threshold definitions

Defining the initial movement of particles has proven difficult. A continuum of threshold conditions characterizes the transition from the initial movement of particles to continuous movement as shear velocity is increased over a sandy surface (Figure 4). First, particles at rest begin to roll, slide, or jerk forward as bedload. As shear velocity is increased intermittent bedload movement of the average sized particles and saltation of the smallest particles begin (Figure 4). Saltating particles initiate bedload transport of the coarsest particles. These thresholds of transport mode and intermittency continue until continuous transport in space and time (no intermittency) is achieved (Figure 4). This continuum of movement makes it difficult to assign qualitative and therefore also quantitative definitions to the threshold (Lavelle and Mofjeld, 1987; Nickling, 1988). Yet, both qualitative and quantitative definitions are used

in the literature although no consensus regarding the fluid threshold has been achieved. Accordingly, a number of threshold definitions exist (Lavelle and Mofjeld, 1987).

	Smallest particles in bedload	Average size particles in bedload / Smallest particles in saltation	Largest particles in bedload / Average size particles in bedload or saltation / Smallest particles in saltation	Particles of all size in bedload or saltation
Gilbert, (1914)	Incipient Motion			
Kramer, (1935)	No Transport	Weak	Medium	General
Bagnold, (1936)	←———— Fluid Threshold ————→			
Shields, (1936)				Critical Threshold
Chepil, (1945b)	Minimal Threshold		Maximal Threshold	
Vanoni, (1964)	←——— Threshold ———→			
Iversen and White, (1982)	Fluid Threshold			
Jiang and Haff, (1993)				Critical Threshold
Cornelis and Gabriels, 2004)	Fluid Threshold			
Kok et al., (2012)	Fluid Threshold			

Increasing Shear Velocity →
Requires Shorter Time-Averaged Shear Velocity ←

Figure 4: Continuum of qualitative definitions for the threshold of motion comparing different threshold definitions.

Gilbert (1914, p. 68, 71) defined 'incipient' motion as several grains moving over a plane-bed surface. This has been referenced as synonymous with Kramer's (1935) definition of 'medium movement' (Buffington and Montgomery, 1997) (Figure 4). Kramer (1935) defined four types of threshold conditions for an entire test bed: (1) *no transport,* where no movement is observed throughout an entire test bed; (2) *weak transport,* where the finest grains are

intermittently transported; (3) *medium transport*, where a large number of the average grain size particles are in motion; and, (4) *general transport*, where particles are in continuous movement along the entire test bed and at all time periods. General movement here is qualitatively analogous to Bagnold's (1936, 1937a) dynamic threshold (as discussed above), and Shields' critical tractive force (Lavelle and Mofjeld, 1987).

Shields (1936) extrapolated the threshold from observed transport rates measured in a series of flume experiments. Shields' (1936) definition corresponds to full movement throughout the wind tunnel, in agreement with Kramer's (1935) 'general transport' and Jiang and Haff (1993). The critical threshold corresponds to the Shields' parameter $\beta = 0.06$ in the 'full rough zone'. However, Vanoni (1964) questioned this value as considerable transport was seen at $\beta = 0.03$. This reduction in the critical threshold value as suggested by Neil (1967) is due to the continuum of transport associated with early stages of movement. In support of Shields' conclusion, a range of threshold conditions are plotted and an interpolated line of best fit is drawn to determine the critical value for different particle Reynolds number. Neil (1967) and Neil and Yalin (1969) define the threshold by the number of particles moving in an area for a set time interval:

$$threshold\ constant = \frac{nd^3}{u_*} \tag{15}$$

where n is the number of grains displaced per unit area per unit time. However, this definition has not been widely adopted in either fluvial or aeolian environments. From this literature, a handful of quantitative definitions have been developed: Fletcher (1976) defined the threshold by the point when a particular transport rate was reached; Wilcock (1988) used a definition specifically for mixed-grain populations based on the number, size, and percent of population moving over a unit space per unit time; and Vanoni (1964) marked the threshold by continuous transport for 2 s at any space per unit time.

The observation of grain motion has also been used to define the threshold. Nickling (1988) observed the number of saltating grains passing through a vertical beam. Lyles and Krauss (1971) visually identified a continuum of threshold movement spanning particle vibration to the entrainment of saltation. Dong et al. (2003) defined the threshold as the instance when 5 grains became stuck to a thin strip of sticky tape set flush with the surface. A minimum and maximum threshold condition based on the size fraction moved was developed by Chepil (1945b). In wind tunnel and field experiments Chepil (1945a, p 309) noted particles first rolled (~2 cm), followed by a sudden vertical lift from the surface. These particles were accelerated downwind by the force of the wind (moving as saltation), impacting the surface between 6 and 12 degrees, causing more particles to move in either saltation or bedload. Chepil (1945a) found relative measures of surface creep to depend upon a grain population. The largest fraction of creep ranging from 7-25% of the total transport occurred for sizes greater than 0.5 mm. Increasing surface roughness results in a decrease in the percent of surface creep (Chepil, 1945a).

Iversen and White (1982), Corenlis and Gabriels (2004), and Kok et al. (2012) identify the fluid threshold as the initiation of saltation. Cornelis and Gabriels (2004) theoretically derive the threshold of motion for wind-blown sand based on the balancing of forces, degree of grain exposure, packing, sorting, and pivoting angle using the data from Iversen and White (1982). Jiang and Haff (1993) found the threshold of 'continuous' motion with particles moving at all times (Buffington and Montgomery, 1997), corresponding to Kramer's 'general transport' and Shields (1936).

The threshold has been described as a statistical problem that can only be evaluated using probability functions involving turbulent shear stress, grain population characteristics, and degree of particle exposure (Shields, 1936; Grass, 1970; Gessler, 1971; Paintal, 1971). The

arrangement (position, size, distribution type, interparticle forces) of particles on a surface makes it difficult to model the threshold of any individual particle within a population of sand grains. Instantaneous turbulent fluctuations in the fluid unevenly distribute shear stress over the surface. For a specific area, local shear stress fluctuations can be characterized by a probability distribution (Grass, 1970). Likewise, a sandy surface will have a population of grains with different shapes, positions, and sizes that can also be characterized by a probability distribution (Grass, 1970). Grass (1970) used these probability distributions to resolve the threshold conditions (Figure 5). When the distributions do not overlap, the threshold of motion is not exceeded (Figure 5a). However, as average shear velocity increases, the shear stress distribution begins to overlap with the fixed distribution of forces required to initiate particle movement, and incipient motion of select grain occurs (Figure 5b). As the two distributions increasingly overlap, more particles are entrained until 'general transport' is reached (Figure, 5c).
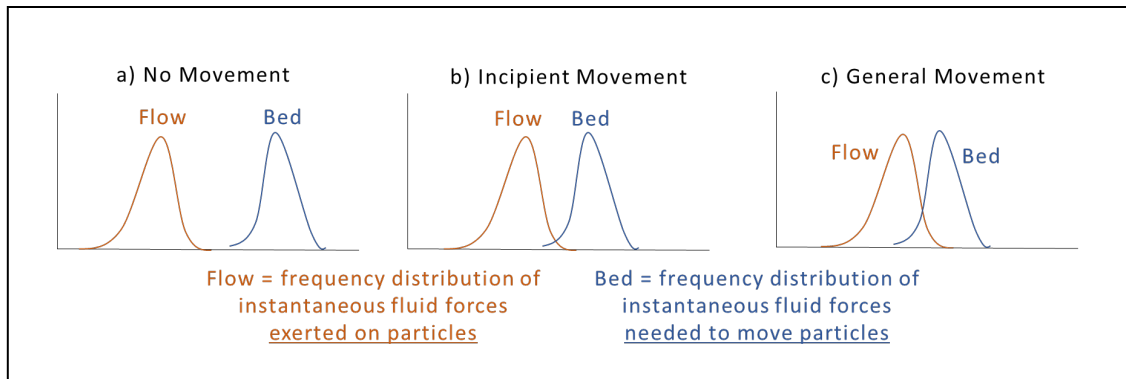
Figure 5: Stochastic nature of the threshold for motion as described by Grass (1970). The frequency distributions of instantaneous fluid forces exerted on surface particles and the frequency distribution of the instantaneous fluid forces required to initiate particle movement are shown: a) no movement, b) incipient movement, and c) general movement.

Bagnold (1955, p. 32-33) demarcates the threshold of motion based on the initiation of bedload and saltation via either the fluid force alone or the combination of the fluid force and the impact of saltating grains:

> *"When the wind speed was increased above the impact threshold the stimulating sand inflow being cut off- another critical wind speed was reached when the surface grains, previously at rest, began to be rolled along the surface by the direct pressure of the wind. The particular wind speed at which this happened was not so definite as in the case of the impact threshold, for the rolling started at different points in the tunnel according to the strength of the wind…..I have previously called this the 'static' threshold wind speed, to distinguish it from the 'dynamic', but I shall take this opportunity to re-name it the Fluid Threshold*

(that at which sand movement starts owing to the direct pressure of the fluid only)."

Here, Bagnold denotes the fluid threshold as movement of bedload: particles that roll, slide or move in small hops over the surface driven by the direct force of the wind (Bagnold, 1937a, 1937b; Leatherman, 1978; Anderson, 1987). The movement of particles in small hops is often referred to as reptation and is sometimes considered to be a mode of transport intermediate of bedload and saltation (Willetts and Rice, 1989; Anderson et al., 1991; Kok et al., 2012). The term, derived from the Latin verb *reptare,* meaning 'to crawl' (as in reptile), is also used interchangeably with bedload, or creep (Mitha et al., 1986; Ungar and Haff, 1987; Werner and Haff, 1988; Werner, 1990; Welland, 2011; Lämmel et al., 2012). Some define reptation as a mode of, or synonymous with, bedload transport (Bagnold, 1937a, 1937b; Owen, 1964; Leatherman, 1978; Anderson, 1987; Ellis and Sherman, 2013).

Thresholds are discussed as either the first motion over a bed of sand particles, or the first motion of a single sand particle. Sometimes it is unclear what scale threshold values represent (Miller et al., 1977; Lavelle and Mofjeld, 1987). Further problems arise with the inconsistent qualitative definition of factors contributing to field-derived thresholds (Einstein, 1942; Neil and Yalin, 1969; Lyles and Krauss, 1971; Lavelle and Mofjeld, 1987; Wilcock, 1988). These inconsistencies may include the mode of transport (bedload or saltation), area of transport, duration of transport, and/or the number of grains transported. Because of this, models are developed to represent the threshold of motion for a population of grains (Bagnold, 1936; Fletcher, 1976; Greeley and Iversen, 1985; Nickling, 1988; Shao and Lu, 2000; Kok and Renno, 2006). These [habits? There's a better word, but you know what I mean] are largely rooted in Bagnold's (1936) formulation of the threshold of motion. However, as outlined below, there are

a number of potential sources of error embedded in Bagnold's original methods and threshold derivation.

2.2 Bagnold's derivation of the fluid threshold

Bagnold derived Equation (1) from a series of wind-tunnel experiments using dry, uniform sand ranging from 0.18 – 0.3 mm. Beginning with conditions below the threshold, Bagnold slowly increased wind speed until movement began. First, Bagnold noted the development of small craters on the order of the average grain diameter. Second, particles intermittently moved in forward jerking motions and moving only a few millimeters before coming to rest. Intermittent jerking motions transitioned with increasing speed to particles rolling along, and staying in contact with, the surface. Bagnold defined this intermittent bedload movement as the fluid threshold. When the fluid threshold was reached, Bagnold read the pressure difference between a single pitot tube facing into the wind and a static tube built into the ceiling of the tunnel. The tubes were joined by a U-shaped manometer and pressure differences could be easily read on the gauge to later be converted to a velocity via:

$$ u = \sqrt{\frac{2(p_1 - p_{2)}}{\rho}} \tag{16} $$

where p_1 and p_2 represent static and pitot pressure. Bagnold measured the velocity profile at 4 different locations spaced 1 m apart along the 9.14 x 0.30 x 0.30 m tunnel. The velocity at each height and for each profile was measured independently using the manometer system; in other words, they were not measured simultaneously. The specific locations of measured velocity profiles are currently unknown and the measurement height of velocities was not consistent.

Based on the work of Owens (1908) and Jeffreys (1929) Bagnold aimed to find the threshold velocity at the top of a particle:

$$u^2 = A' \left(\frac{\rho_s - \rho}{\rho} \right) gd \tag{17}$$

where u is the wind speed and A' is a constant equal to:

$$A' = \frac{1}{3} + \frac{1}{9} \pi^2 = 1.43 \tag{18}$$

Bagnold collected two sets of observations to resolve the height where $v = 0$. The first sets of observations were collected over a fixed surface and the second over a mobile surface (see Bagnold, 1955, p. 58). The velocity at each height was averaged over the length of the tunnel, i.e. the average speed of 4 velocity readings at the same height spaced 1 m apart (Lagrangian spatial averaging). Bagnold does not report any time averaging of velocity measurements because he was reading point pressure differences at each height. Rather, his texts suggest he averaged repeated measurements (potentially 8 times for each along-tunnel location and height). Velocities were calculated for heights 2, 3, 4, 6, 8, 10, 15, 20, and 40 mm above the surface. However, no single velocity profile used all heights. Bagnold reports a minimum of 2 and maximum of 7 heights recorded for velocity profiles. The resulting velocity at each height was plotted against a logarithmic height, and extrapolated to find $v = 0$. Bagnold (1936, p. 603) found his profiles to correspond well with Prandtl (1925):

$$u_z = \sqrt{\frac{\tau}{\rho}} \left(5.75 \, log \frac{z}{k} + 8.5 \right) \tag{19}$$

to find the z where $u = 0$ to equate to $\frac{k}{30}$ in order to satisfy Equation (19). This height corresponded to the mean height of surface irregularity, $z_0 = \frac{k}{30}$, not the top of a particle. He theorized that no matter the shape of the profile, all velocity profile extrapolations to $u = 0$ would converge at a height k. With the velocity profile extrapolation to $v = 0$ for conditions when no transport was occurring, Bagnold finds the average $k \cong 0.0006 \, m$, a value that corresponds to the average between half the grain diameter and the size of the small craters on

the surface (Bagnold, 1936, p. 603). Before transport occurs, the height of the surface irregularity should be approximately z_0.

At this point in Bagnold's derivation, he had the measured the necessary variables to solve for the fluid threshold shear velocity, $u_{*t\ fluid}$. Using the identity $u_* \equiv \sqrt{\frac{\tau}{\rho}}$, Bagnold (1937a, p. 412, 414) solved for the fluid threshold shear velocity, $u_{*t\ fluid}$:

$$u_z = 5.75\ u_{*t\ fluid} log \frac{z}{z_0} \tag{20}$$

$$u_{*t\ fluid} = \frac{u_z}{5.75\ log\frac{z}{z_0}} \tag{21}$$

Bagnold uses the fluid threshold wind velocity, $u_z = 2.6\frac{m}{s}$ measured at the lowest height $z = 0.002\ m$, $k = 0.0006\ m$ extrapolated from velocity profiles, and $z_0 = \frac{k}{30} = \frac{0.0006}{30}$ (Bagnold, 1936 p. 603-604) that corresponds to the height of surface irregularity to solve for $u_{*t\ fluid} = 0.226\frac{m}{s}$. This fluid threshold shear velocity relates a velocity to the initiation of bedload movement independent from height.

With a known u_*, Bagnold was able to resolve the A parameter by combining Equations 17 and 21:

$$u_t = \ log \frac{30k_A}{d} \times A \sqrt{\left(\frac{\rho_s - \rho}{\rho}\right) gd} \tag{22}$$

where $k_A = 0.002\ m$ the height where $v = 0$ for a fixed bed. Solving for A:

$$A = \frac{u_t}{log\frac{30k}{d} \times \sqrt{\left(\frac{\rho_s-\rho}{\rho}\right) gd}} = 0.47 \tag{23}$$

$$u_{*t} = \frac{0.47}{5.75} \sqrt{\left(\frac{\rho_s - \rho}{\rho}\right) gd} \tag{24}$$

where $A = \frac{0.47}{5.75} = 0.082$ for the dynamic threshold. Bagnold originally (1936) found $A = 0.43$ from Equation 23, but subsequently changes his value in a footnote in Bagnold (1937a, p. 415),

which can be found by substituting k in Equation 19 for $k' = 0.003\ m$, the focal point for all velocity profiles when the sand was mobile.

Bagnold found A to be 0.082 for the dynamic threshold and 0.1 for the fluid threshold. Bagnold's fluid threshold is resolved by rearranging Equation 1 and incorporating $u_{*t\ fluid} = 0.226\ \frac{m}{s}$ found in Equations 20 & 21, we arrive at $A \cong 0.1$:

$$A = \frac{u_{*t\ fluid}}{\sqrt{\left(\frac{\rho_s - \rho}{\rho}\right)gd}} = 0.97 \cong 0.1 \tag{25}$$

and for $u_{*t\ dyamic} = 0.192\ \frac{m}{s}$:

$$A = \frac{u_{*t\ dynamic}}{\sqrt{\left(\frac{\rho_s - \rho}{\rho}\right)gd}} = 0.083 \cong 0.08 \tag{26}$$

It is common practice to use these two values to distinguish between each threshold by defining the A parameter as 0.1 for the fluid and as 0.08 for the dynamic. However, the A parameter is also a function of grain size as noted in Bagnold (1937a, p. 415-416):

"*The upper, or 'static threshold'* [fluid threshold]*, is that required to move the grains in the first instance by direct wind action alone. This static threshold wind is not very definite since it depends on several factors: on the former history of the surface and the extent to which sand removal has collected a protective layer of the biggest grains on the surface; on the surface turbulence of the wind, which may be accentuated by a large temperature difference between the air and the sand surface; and on the length of the exposed surface....Over the experimental distance of 10 meters the ratio of the static to the dynamic threshold gradient for sand of 0.024 cm was as 1.15 to 1. For coarse sand of 0.1 cm the ratio increased to 1.4 to 1.*"

For an average grain population of 0.24 mm, the ratio of static to dynamic thresholds was 1.15 to 1. For an average grain population of 1.0 mm, this ratio was 1.4 to 1. This is not noted in his 1936 publication, but is outlined in Bagnold (1937a). By extracting values directly from his original publication for the fluid and dynamic thresholds, one finds A to vary with grain size (Figure 6):

$$A_{fluid} = 0.1007\, d^{-0.011} \tag{27}$$

$$A_{dynamic} = 0.0806\, d^{-0.005} \tag{28}$$
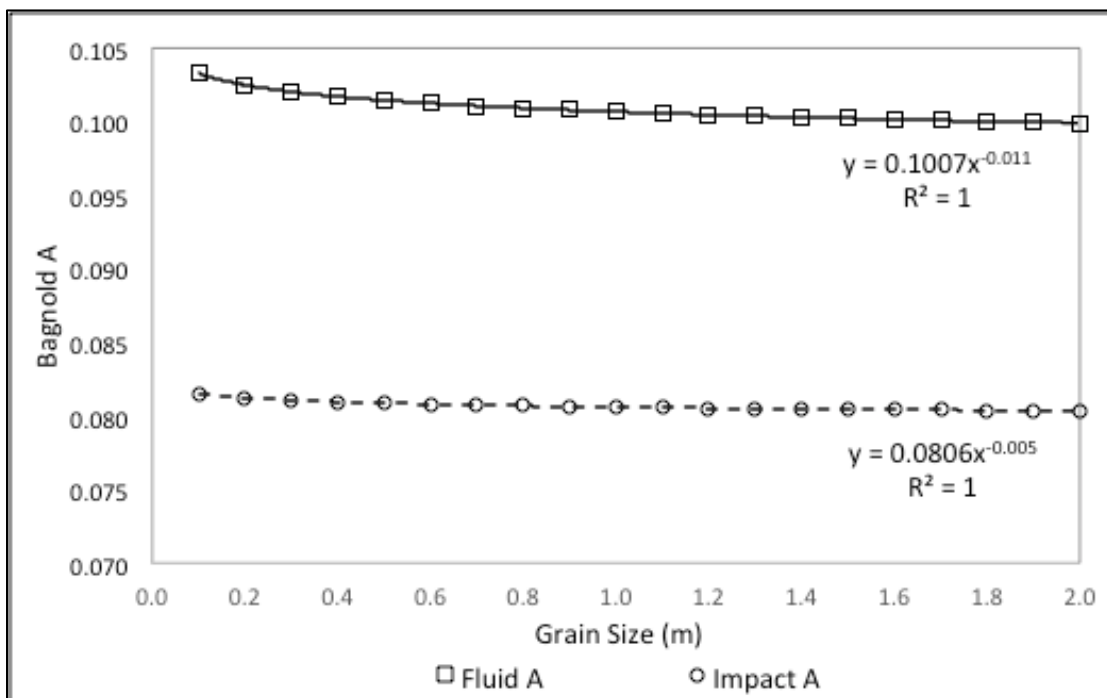
Figure 6: Relationship between grain size and Bagnold's A parameter.

The A parameter decreases with increasing grain size and appears to approach a limit at larger grain sizes for both the fluid and dynamic threshold. The A parameter is largest for small particles reaching 0.103 for particles of with $d = 0.1\ mm$ at the fluid threshold. However, this is often disregarded in the literature and A is used as a constant. Bagnold's A parameter is the only empirically-derived variable in his model and is also the only variable not a function of the second root, making small variability in A result in substantial errors in u_{*t}. Disregarding the variability of A with grain size from Bagnold's wind tunnel experiments results in errors in the prediction of threshold shear velocity.

Bagnold's model is a function of A and d, but is limited by the type of fluid flow. Surfaces with 'hydrodynamically smooth' flow, $Re_p < 3.5$, interact with particles differently than 'hydrodynamically rough' flow, $Re_p < 3.5$. Under smooth flow, either the particles do not protrude enough into the flow, or the shear velocity is not great enough to shed small eddies on the lee side of particles. This reduces drag on a particle. The A parameter increases for particles smaller than 0.1 mm and no longer varies with the square root of the grain diameter (Bagnold, 1955). Bagnold's fluid threshold shear velocity using A as derived in Equations 24 for 'hydrodynamically rough' conditions is expressed as (Figure 7):

$$u_{*t} = 0.1007 d^{-0.011} \sqrt{\frac{\rho_s - \rho}{\rho} g d} \tag{29}$$

and the dynamic threshold shear velocity as:

$$u_{*t} = 0.0806^{-0.005} \sqrt{\frac{\rho_s - \rho}{\rho} g d} \tag{30}$$

Note the slope coefficient is equal to 0.47; the adjusted value of the experimental A changed from 0.43 in the footnotes of Bagnold (1937a, p. 415).
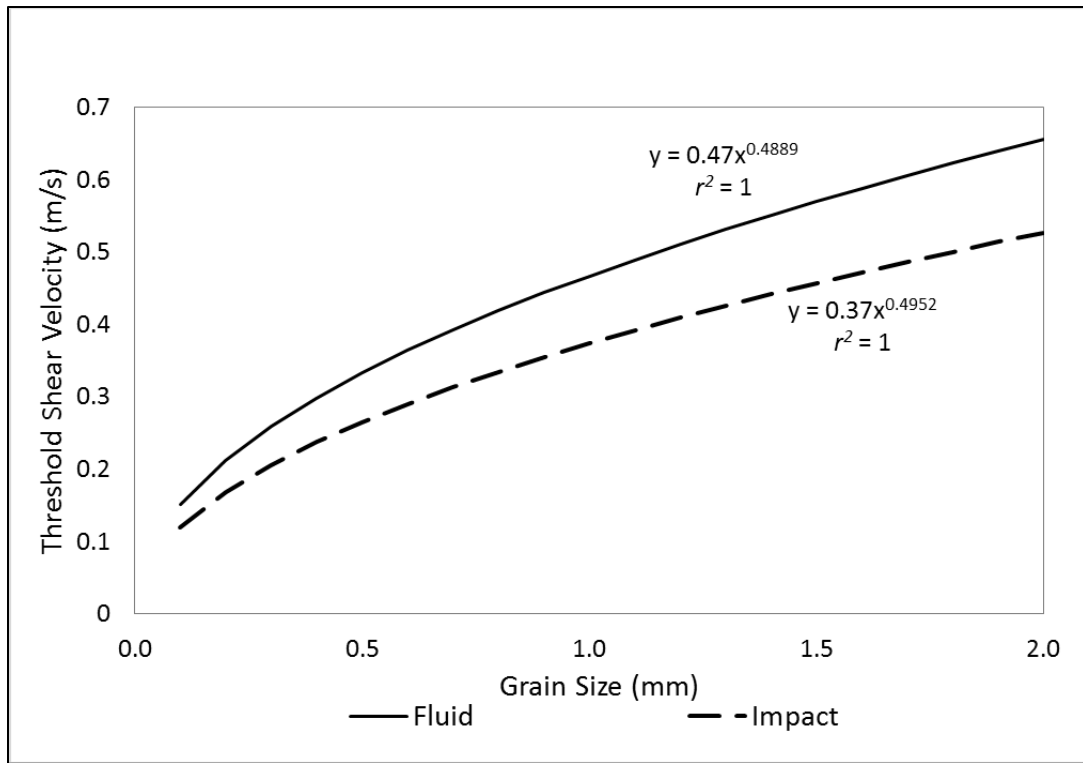
Figure 7: Bagnold's threshold shear velocity model derived from Equations 29 & 30.

2.3 Other threshold models

Since Bagnold's wind tunnel work, a number of models of the fluid threshold have been developed (Figure 8). Each model and its variables are outlined in Table 2. These are largely rooted in Bagnold's original methodology, subsequently re-evaluating, or adding to, Bagnold's model via the inclusion of additional forces (e.g. electrostatics). Fletcher (1976) used a low-turbulence wind tunnel to evaluate the influence of cohesion on the threshold for dust and fine grain particles. He defined the threshold as the point when $10 \frac{g}{m^2}$ was removed from a surface within 60 s. Using glass spheres ranging from 0.25-032 mm, Fletcher (1976) found the *A*

parameter equal to 0.13. Of the models presented here, Fletcher's model consistently predicts

greater threshold shear velocities (Figure 8).

Table 2 Threshold shear velocity models

Reference	Transport Model
Bagnold (1936)	$$u_{*t} = A \sqrt{\frac{\rho_s - \rho}{\rho} gd}$$
Fletcher (1976)	$$u_{*t} = \sqrt{\frac{\rho_s - \rho}{\rho}} 0.13 \sqrt{\frac{g}{d}} + 0.057 \sqrt[4]{\frac{C}{\rho_s}} \sqrt{\frac{v}{d}}$$
Greeley & Iversen (1985)	$$u_{*t} = \left(0.129 \sqrt{\frac{1}{\sqrt{1.92 Re_t(0.092 - 1)}}} \right) \sqrt{\frac{\rho_s - \rho}{\rho} gd}$$
Nickling (1988)	$$u_{*t} = b - \sqrt[6]{5a^2}$$
Shao and Lu (2000)	$$u_{*t} = \sqrt{A_n \frac{\rho_s}{\rho} gd + \frac{\gamma}{\rho}}$$
Kok & Renno (2006)	$$u_{*t} = \sqrt{\frac{A_n}{\rho} \rho_s gd + \frac{6\beta G}{\pi d} - \frac{8.22\varepsilon_0 E^2}{c_s}}$$
$An = 0.0123 \, ; \, G = 1; \, \beta = 1.2{\times}10^{-4}; \, e^0 = 8.85{\times}10^{-12}; E = 120 \, mV; \, c_s = 0.4671;$ $$\gamma = 1{\times}10^{-4}; C = 0$$	
A_n is a dimensionless parameter scaling with aerodynamic forces (Kok and Renno, 2006) G is a geometric parameter related to bed stacking (Shao and Lu, 2000) β is an empirical constant scaling to interparticle forces (Shao and Lu, 2000) ε_0 is the electric permittivity of the air; (Kok and Renno, 2006) E is the sum of the electric fields close to the surface (Kok and Renno, 2006) c_s is a scaling constant based on the non-sphericity of a particle (Kok and Renno, 2006) γ is a parameter associated with the interparticle forces (Shao and Lu, 2000)	
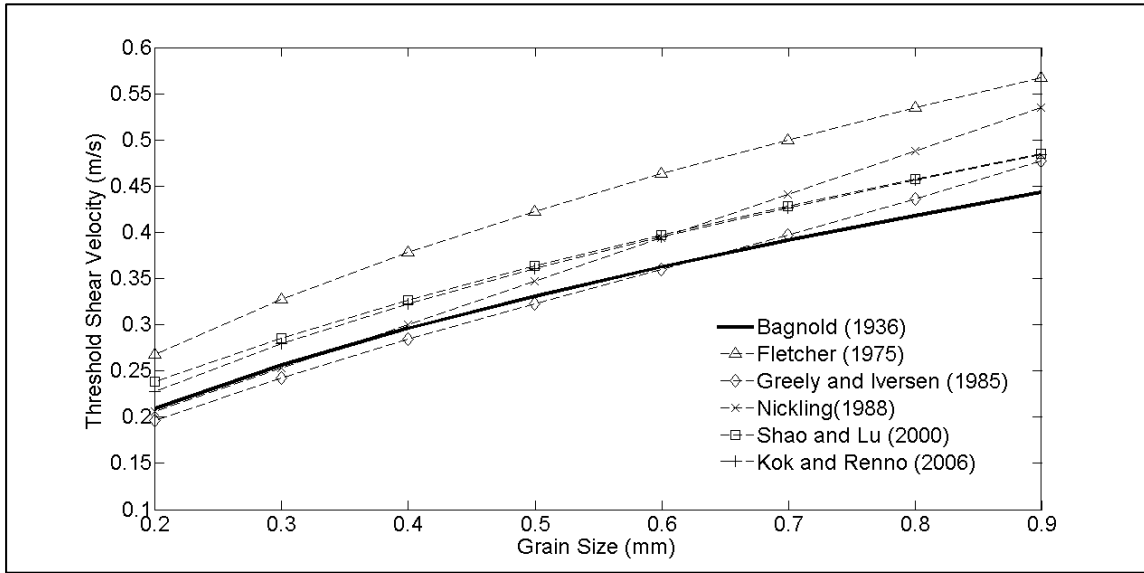
Figure 8: Models predicting the threshold shear velocity for wind-blown sand.

Greeley and Iversen (1985) re-evaluated Bagnold (1936) by redefining the *A* parameter in to account for cohesion and aerodynamic lift via two empirically-derived parameters: $F(Re_t)$ and $G(d)$. The function $F(Re_t)$ incorporates the particle Reynolds number at the threshold of motion as the Reynolds number is dependent upon aerodynamic drag (Shao and Lu, 2000). The function $G(d)$ in Greeley and Iversen's model represents interparticle forces and is a function of particle size. However, Shao and Lu (2000) suggest the function $G(d)$ in Greeley and Iversen's model is a result of a misfit in their data analysis, and questions the physical expression of these two functions. Consequently, Shao and Lu (2000) derived a 'simplified' threshold shear velocity model to account specifically for van der Waals and electrostatic forces. The formulation by Shao and Lu is very similar to Bagnold (1936) but has a greater overall threshold shear velocity for all sand size particles (Figure 8). Kok and Renno (2006) resolved a threshold shear velocity

model based on the work of Shao and Lu (2000). They directly measured the reduction in weight of a surface sample with different magnitudes of electrostatic force.

These models focus on incorporating interparticle forces to decrease uncertainty in predictions of threshold shear velocity. Yet, only Nickling (1988) focused on incorporating grain size distribution statistics other than the average grain size to reduce errors between predicted and observed threshold shear velocity. Nickling (1988) resolved the threshold shear velocity for different grain size distributions with a range of average grain sizes and sorting values. Defining the threshold by the number of grains moving as saltation, the resulting model employs two empirical constants requiring the average grain size and sorting. However, for bimodal distributions his a coefficient no longer holds. In comparison to other models, Bagnold's (shown by the solid line in Figure 8) typically predicts lower threshold shear velocities. These threshold models aim to reduce uncertainty in the threshold shear velocity and result in a greater shear velocity than Bagnold (Figure 8). Yet, considerable variation between each model is evident.

Discrepancies between predicted and observed threshold shear velocities at the early stages of transport propelled a recent trend to associate threshold wind speeds with the initiation of transport (Stout and Zobeck, 1997; Schönfeldt, 2004; Wiggs et al., 2004b; Davidson-Arnott and Bauer, 2009). Much of this work was based on transport intermittency at low transport rates where the fluid threshold is repeatedly exceeded and immediately followed by a lull in fluid flow not capable of sustaining motion (Schönfeldt, 2004). Stout and Zobeck (1997) developed the Time Fraction Equivalence Method (TFEM), subsequently revised and re-evaluated by Wiggs et al. (2004b) and Davidson-Arnott and Bauer (2009), that defines the threshold by an iterative function dependent on the fraction of time in which transport occurs and the fraction of time the threshold is exceeded. First, an intermittency factor is calculated via a binary series where 1 (0)

represents transport (no transport).   A second intermittency factor is also created that corresponds to an estimate of threshold wind speed where 1 (0) indicates wind speeds above (below) the estimated threshold. Second, the two intermittency factors are summed and divided by the number of observations in the sampling period. The estimated threshold wind speed is iteratively adjusted until the two intermittency factors are equal. As a result, threshold wind speeds are a function of the measurement height of wind speed, sampling interval, averaging period, sensor used to measure transport, and mode of transport measured (Sherman et al. 2014). Additionally, wind speed is dependent upon height. This makes it difficult for inter-study comparisons and repeatability, but more importantly, impractical for predicting the threshold and resulting sand transport in various environments (Sherman et al., 2014).   Yet, threshold wind speed can be used understand the range of thresholds over various surfaces, especially when minimum and maximum thresholds are defined (Davidson-Arnott and Bauer, 2009).   While threshold wind speed has some limitations it also provides insight into spatial and temporal variability at a particular site, over different types of surfaces (uniform versus mixed size), and with different controls on sand transport (cohesion, electrostatics, surface compaction).

The use of threshold wind speeds to describe the threshold arises from the inconsistency between predicted and observed threshold shear velocity in field environments. Some reasons for the discrepancy are the previous inability to separate bedload from saltation, different definitions of the threshold, and the use of an average grain size despite the distribution type (e.g. bimodal, polymodal). Additionally, there are sources of uncertainty in Bagnold's model that may result from his original experiments. The following text introduces these uncertainties as potential reasons for discrepancies in predicted and observed thresholds found in wind tunnel and field environments.

2.4 Sources of uncertainty in Bagnold's model

Errors are manifestations of an incomplete portrayal of physical processes governing phenomena. These may arise from inaccurate data collection procedures, inaccurate assumptions, incorrect theoretical development, or problems with analysis. One avenue to systematically identify and classify potential errors rooted within Bagnold's model is Allchin's (2001) taxonomy of error types. Error analysis similar to Allchin's (2001) taxonomy has been utilized previously in small-scale aeolian studies as a method to analyze and classify errors when comparing wind tunnel observations to field data (Sherman and Farrell, 2008). According to Allchin's error classification, potential errors in Bagnold's model could be a function of one or several types of errors: (1) material, (2) observational, (3) conceptual, and/or, (4) discoursive. A number of potential errors are found in Bagnold's model original experimental procedures.

Table 3 relates Allchin's (2001) framework for error analysis specifically to errors found in Bagnold's (1936) threshold shear velocity derivation. Each of these types of errors can overlap and contribute to each other. This is the case in Bagnold's (1936) threshold shear velocity model; errors include material used, inaccurate assumptions, reporting typos, and miscalculations.

Table 3 Potential sources of error for Bagnold's (1936) threshold shear velocity model relative to Allchin (2001) taxonomy of error types.

Error Analytics Framework by Allchin (2001, p 42)	Corresponding Sources of Uncertainty in Bagnold's (1936) Fluid Threshold of Motion
MATERIALS • Improper materials • Improper procedure • Perturbation of phenomenon by observer • Failure to differentiate similar phenomenon through controlled conditions	MATERIALS • Bedload trap captured saltating particles • Use of wind tunnel to simulate natural boundary layer conditions
OBSERVATIONAL • Insufficient controls to establish domain of data or observations • Incomplete theory of observation • Observer perceptual bias • Sampling error	OBSERVATIONAL • Visual demarcation of threshold conditions • Few experimental velocity profiles reported (some with different heights measured)

CONCEPTUAL
• Flaw in reasoning
• Inappropriate statistical model
• Inappropriate specification of model from theory
• Mis-specified assumptions or boundary conditions
• Theoretical scope (domain) over/undergeneralized
• Incomplete theory, lack of alternative explanations
• *Theory-based cognitive bias, entrenchment
	CONCEPTUAL
	• Use of average grain size to represent entire population of grains with different sizes
	• No specification of confidence limits or statistical uncertainty of u_{*t}
	• Uncertainty in extrapolation of velocity profile to find k' & z_0
	• Inaccurate assumptions:
	  (i) constant A may not be constant
	  (ii) u_{*t} may not be constant

DISCOURSIVE • Communication failures: incomplete reporting, obscure publication, translation hurdles, patchy citation/search system • *Mistaken credibility judgments • *Unchecked sociocultural cognitive biases • *Breakdown of systems for credentialing scientific expertise • *Public misconception of scientific results and misunderstanding of science (poor science education, poor science journalism, etc.)	DISCOURSIVE • Unreported number of samples used to calculate transport rates and threshold of motion estimates • Unclear qualitative definition corresponding to fluid threshold • Threshold shear velocity equation reported with typos in (1936) publication • Threshold shear velocity experimental constant changed from 0.43 to 0.47 without sufficient explanation in (1936) to (1937) publication • Unknown number of grain sizes and distributions tested

*Indicates errors reported in Allchin (2001) that do not specifically relate to Bagnold's (1936) threshold shear velocity model.

Material errors found in the original derivation of Bagnold's model are associated with his bedload trap and potential inability to recreate and subsequently measure boundary layer conditions. In wind tunnels it is necessary to 'trip' the boundary layer with roughness elements (often a roughness plate) placed at the mouth of the wind tunnel. Without such, it is difficult to simulate natural boundary layer conditions. Bagnold does not report using a roughness plate, or any equivalent, in his detailed description of his wind tunnel setup. Additionally, Bagnold's bedload trap captured both bedload and saltation, preventing measurement that corresponded to his qualitative definition of the fluid threshold.

Moreover, there are a series of observational errors associated with Bagnold's experiments. Bagnold does not report the number of profiles or samples used to calculate shear velocity. The number of velocity profiles used in his derivation is unknown; only a single profile for the fluid and dynamic threshold is published. The fluid threshold profile is marked as the profile over a fixed surface, where sand was made immovable. If the values plotted in his 1936 publications are all of the experimental runs, then only six velocity profiles that correspond to movement for specified shear velocities are used. These have various heights of velocity readings ranging between 2 and 7 point above the surface. Bagnold also found it difficult to define the fluid threshold due to inconsistency in k' extrapolated from velocity profiles. The height of k' consistently changed at the fluid threshold (as noted by Bagnold) and only at the dynamic threshold could he define a consistent k'. Bagnold's inability to extrapolate velocity profiles down to a consistent height k' suggests the fluid threshold is not constant. Wind tunnel experiments have shown variability in u_{*t} (Figure 1) and in A (Figure 2). Bagnold (1936, 1937a) was unable to explain why his A parameter differed from Shields' (1936) A parameter in water which ranged between 0.18-0.22 for turbulent flow. Chepil (1945b) and Zingg (1953) found A values similar to Bagnold's (Chepil's A = 0.09-0.11; Zingg's A = 0.12). However,

37

Lyles and Krauss (1971) found A to agree with Shields estimate for water and suggests no real difference exists. Chepil (1945b), Zingg (1953), Lyles and Krauss (1971), Iversen and White (1982), and Dong et al. (2003) have reported values of A greater than Bagnold's fluid A value of 0.1. However, these investigations do not separate bedload from saltation, and therefore, do not appropriately test Bagnold's A value according to his definition of the fluid threshold as the initiation of bedload particles by the fluid alone.

A conceptual and/or discoursive error revolves around time-averaging. No time-averaging period is reported, yet calculating shear velocity from profiles with $r^2 < 0.98$ results in considerable errors (Bauer et al., 1992). Bagnold spatially averages non-simultaneous point velocities and it is unknown the effect this may have had on this threshold derivation. In addition to potential velocity profile errors, the trap intended to capture only bedload also captured saltation transport (Figure 9). Bagnold's trap was built into the floor of his wind tunnel. The 5 by 20 mm, flow-transverse aperture was set below the surface at a distance equivalent to the thickness of the sand, and was liable to capture both saltation and bedload (Anderson et al., 1991; Tsoar, 2004; Wang et al., 2009). Bagnold (1937b) identified all sand captured in the trap as bedload, and reported bedload as comprising 25% of the total transport; an estimate still used in some aeolian studies (Welland, 2011; Zhang et al., 2012). Others, including Anderson et al. (1991) and Tsoar (1994), consider Bagnold's value to be an over-estimation arising from the trap capturing both bedload and saltation.
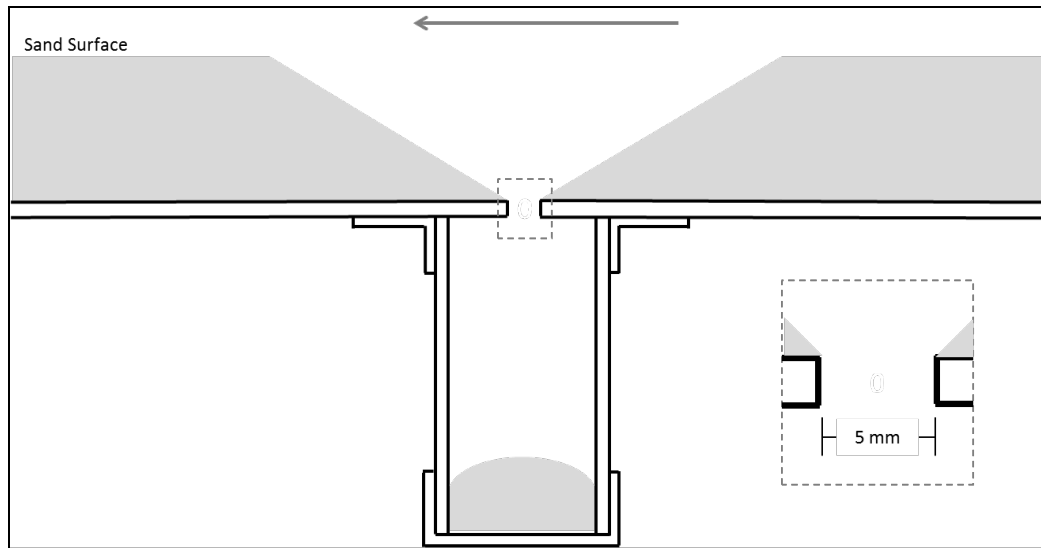
Figure 9: Bagnold 'surface creep' trap.

Conceptual errors are also found in Bagnold's wind tunnel experiments. The grain size distribution, in addition to the average grain size, of a surface can have considerable effects on the fluid threshold and resulting mode of transport (Willetts, 1983; Nickling, 1988; Wilcock, 1988). For instance, it is easier for coarser particles to roll, slide or jerk forward on a bed of finer particles than for finer particles to roll over a bed of coarse grains (Chepil, 1945b; Wiberg and Smith, 1987). Coarser particles can shelter finer grains from shear stress fluctuations. Bagnold's model was developed for uniform grains, but using the average grain size for a mixed population may significantly misrepresent the particle sizes on the surface.

Discoursive errors reside in Bagnold's work and make it difficult to recreate his wind tunnel experiments. Bagnold does not report the number of samples used to calculate transport rates nor velocity profile extrapolations for threshold estimates. He also does not report the reasoning behind changing his empirically-derived *A* constant from 0.43 to 0.47 between his

1936 and 1937b publications. These material, observational, conceptual and discoursive errors lend to misrepresentation of the fluid threshold shear velocity.

2.5 Summary

In 1936 most work on the threshold of motion had been conducted in subaqueous environments (Gilbert 1914; Jeffreys, 1929; Casey, 1935; Kramer, 1935). Bagnold built the wind-tunnel and a number of the instruments used in his experiments, conducting much of that research on his own time. His work is easily the most influential in aeolian geomorphology and the level of work he conducted in the 1930's was unprecedented. However, closely examining his work sheds light on a number of potential sources of error in his derivation of the fluid threshold. Errors residing in the derivation calls for a test of Bagnold's (1936) model of the fluid threshold in a field environment. The following methodology is designed to directly measure the fluid threshold shear velocity for wind-blown sand in a natural, open air environment.

CHAPTER III

STUDY SITE AND METHODOLOGY

3.1 Study site

Field observations of near surface boundary layer conditions and the initiation of bedload transport were measured to test Bagnold's model of the fluid threshold in a natural, noncomplex environment. Experiments were conducted on October 22nd, 2011 in the trough of a blown-out parabolic dune in Jericoaocara, Brazil, situated on a cuspate foreland in the northern state of Ceará (Figure 10), satisfying Objective 1. A unidirectional onshore wind consistently strengthened throughout the day. Wind speeds increased from below the threshold of motion to conditions exceeding the threshold. This area of Brazil is governed by strong northeasterly and southeasterly Atlantic trade winds, and during its dry season, August to December, onshore wind speeds average 7.75 ms^{-1} (Jimenez et al., 1999) with ~80°F temperature. Temperatures remained fairly consistent during data collection. A rainfall event occurred 2 days prior to data collection, but no rainfall occurred during data collection.

Field instrumentation was deployed in the middle of the 50 m wide parabolic trough, with an unobstructed upwind fetch approximately 75 m long (Figure 11). This particular field site has been used in small-scale aeolian transport studies due to the consistent wind over a flat, bare sandy surface (Li et al., 2010; Barrineau and Ellis, 2013). The trough provided a bare, flat open-air sandy surface with unidirectional winds.

Figure 10: Instrumentation deployment site (marked by the 'x') on a sand sheet with unidirectional northeast winds (indicated by arrow) in Jericoacoara, Brazil.

Figure 11: Oblique upwind image from instrumentation deployement. Instruments were placed in the middle of this 50 m wide parabolic trough. Photo credit: Robin Davidson-Arnott.

Unidirectional north-east winds ranged from 5 to 11 ms^{-1} during data collection. A bedload trap was deployed (buried below the surface) the morning of October 21st, 2011. Burial of the bedload trap disturbed the natural surface. Once buried, the surface was raked and ~24 hours was given for the natural surface conditions to return to a pre-distrubance surface where ripples on the order of 5 mm were present (Figure 12). These small ripples organized coarser material in the ripple and finer material in the troughs of ripples (Figure 12), similar to particle size segregation found in Bauer (1991). Data collection began under these surface conditions.
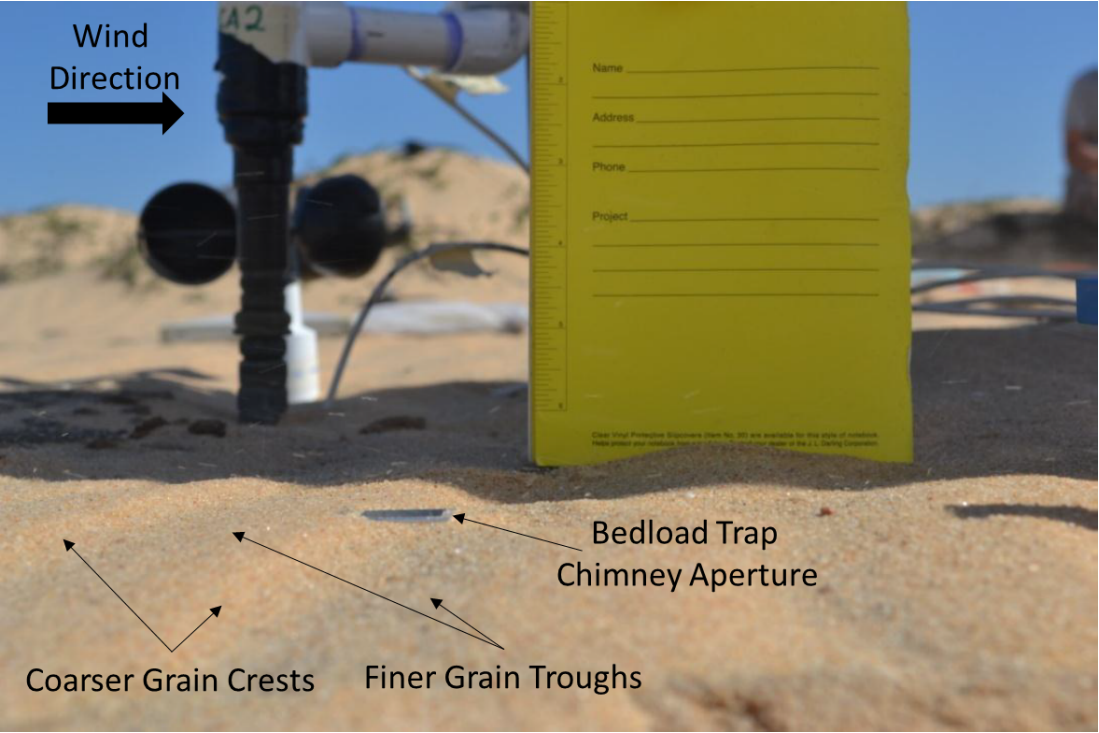
Figure 12: Natural surface configuration and bedload trap chimney opening where bedload particles entered the trap. Wind direction is from left to right and coarse grain crests and finer grain troughs are shown.

3.2 Instrumentation

A trap was designed to capture bedload separate from saltation, housing a piezo-electric sensor capable of high-frequency bedload sampling. Three-dimensional wind flow and a vertical profile of the inner boundary layer was observed to calculate threshold shear velocities associated with the initiation of bedload particles.

3.2.1 Bedload trap

Obtaining field-observed values of the fluid threshold mandates separation of bedload from saltation. A bedload trap was designed specifically for this dissertation to capture bedload while minimizing contamination of trapped samples with grains that are moving via saltation. The trap has three main components: (1) an adjustable chimney that segregates saltation from bedload; (2) a piezo-electric sensor that detects grain impacts and can be sampled at high frequencies; and (3) collection vessels that can be retrieved for sample weighing and grain size analysis.

The trap (Figure 13) was fabricated with a 1/4" aluminum alloy (6061-T6 Al). The alloy is strong enough to survive the stresses associated with long distance shipping and deployment in rigorous field conditions, while still allowing precision welding (a tolerance of about 1 mm) during fabrication. Reinforcement walls (Figure 13a) and a detachable door with a silicone rubber seal keep sand from clogging the access portal and prevent entry of water and sediment. The housing has a 15.6 mm (diameter) circular outlet with an adaptable compression fitting to accommodate power and signal cables and protect them from damages that might result from the stresses of installation during multiple field deployments (Figure 13b).

Within the housing case there is space for sample vessels to collect bedload and, if desired, saltation (Figure 13c). Sand is led from the surface aperture to the vessels through a

bifurcated chimney (Figure 14). The position of chimney is adjustable through a vertical range of 100 mm so that during measurement the aperture (with a 20 by 20 mm opening) can be set flush to the sand surface. After adjustment the chimney is secured with sliding thumbscrews along a double slotted wall in the outer housing. The side of the chimney intended to collect bedload includes a built-in funnel to guide grains to the face of a piezo-electric impact sensor (also known as a Buzzer Disk described in Li, 2010 and Sherman et al., 2011) that registers the grain impact. The resulting signal is amplified through a printed circuit board and transmitted to a data acquisition system.
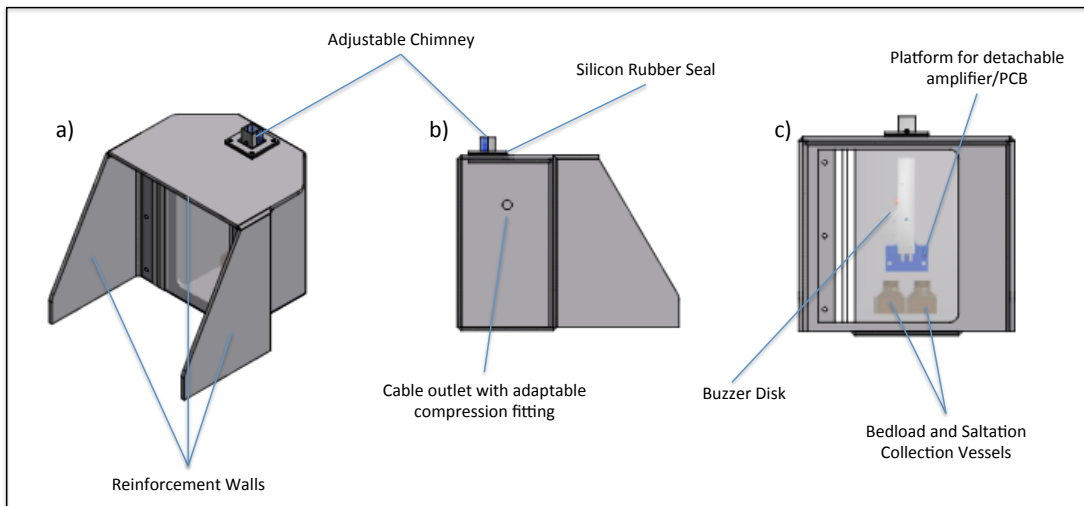
Figure 13: Bedload trap designed for this study. First introduced in Swann and Sherman (2013): a) outer housing case illustrating reinforcement walls to access bedload samples as well as aperture of the adjustable chimney; b) profile view of the trap showing cable outlet with compression fitting to reduce stress on power and signal acquisition cables; and c) profile view looking inside the housing case to show the bedload and saltation vessels, internal adjustment chimney, and piezo-electric *Buzzer Disk* sensor.
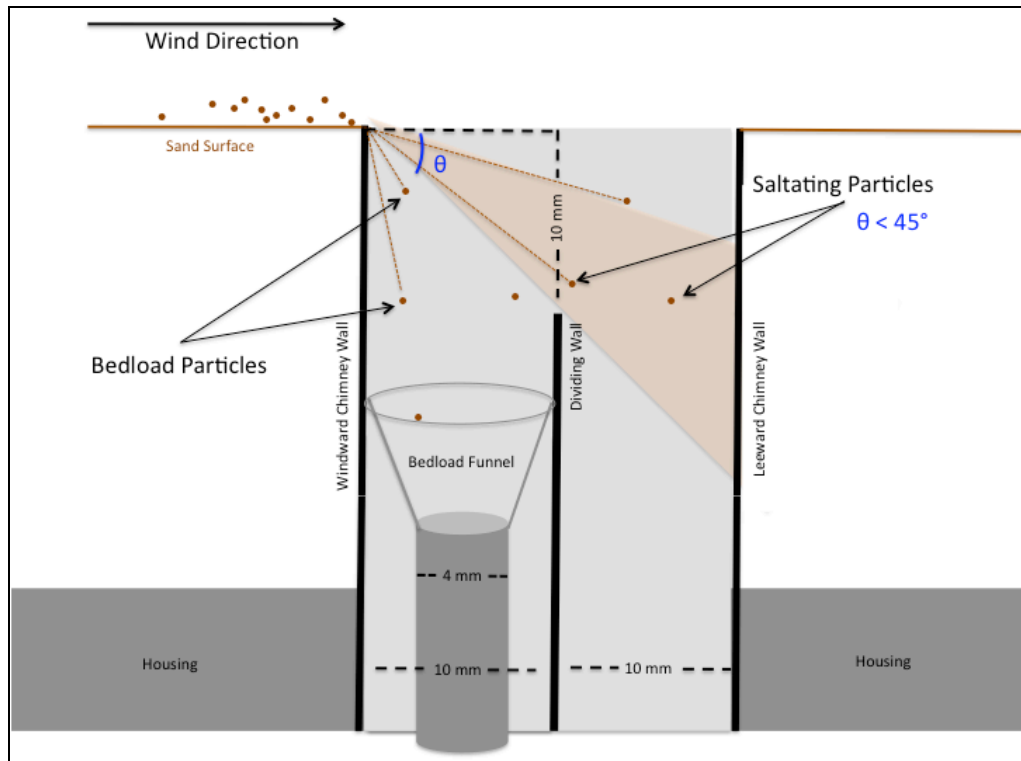
Figure 14: Schematic of internal adjustable chimney adjusted to the height of the surface. As saltation enters the trap between 10-16°, an internal dividing wall separates saltation from bedload particles. Bedload particles enter the trap at a much higher angle, and do not clear the internal dividing wall. These particles are funneled to the face of a piezo-electric sensor.

The main function of the partition within the chimney is to segregate grains moving as bedload from those moving in saltation. The design is based on the concept that saltating grains over a flat surface typically impact the bed at angles less than 16°. Therefore, saltation load should enter a surface-flush aperture at similar angles. A particle moving as bedload would fall into the opening at an angle with the surface much closer to 90° (Figure 14).

3.2.2 Anemometers

Two independent observations of wind flow were collected. A single R.M. Young ultrasonic anemometer (Model 81000) mounted at 1 m above the surface measured three dimensional fluctuations in velocity. Three opposing pairs of ultrasonic transducers record *u, v* and *w* directions providing three dimensional flow velocities. The analog voltage output is 0 to 5000mV with the maximum speed detected at 40 m/s with an accuracy $\pm3\%$. Sampling *u, v* and *w* at 32 Hz fluctuations in *u* and *w* were used to calculate shear velocity at the surface.

The second set of velocity data was collected using R.M. Young Gill-type 3-cup anemometers deployed at 0.10, 0.27, 0.52, 0.74 and 1.01 m above the surface, sampling at 32 Hz. These cup anemometers generate a maximum DC voltage of 2400 mV, and voltages are converted to wind speed using standard calibrations. Cup anemometers at 0.27 m and 0.52 m were calibrated in a wind tunnel prior to field deployment, and for these anemometers the wind tunnel calibration was used to convert signal voltage to velocity. Cup anemometers at 0.10, 0.74 and 1.01 m were not calibrated in the wind tunnel and the calibration outlined in the R.M. Young Gill-type cup anemometer manual was used to convert voltage to velocity.

3.3 Experimental design

3.3.1 Instrumentation deployment

A vertical profile of R.M. Young Gill-type 3-cup Model 12102 and an R.M. Young Ultrasonic Anemometer Model 81000 were deployed 0.5 m from the center of the bedload chimney aperture (Figure 15). The bedload trap aperture and anemometers were deployed in a straight line perpendicular to wind direction. Cup anemometers were mounted at heights 0.10, 0.27, 0.52, 0.74 and 1.01 m above the surface. The ultrasonic anemometer was deployed at 1 m above the surface.
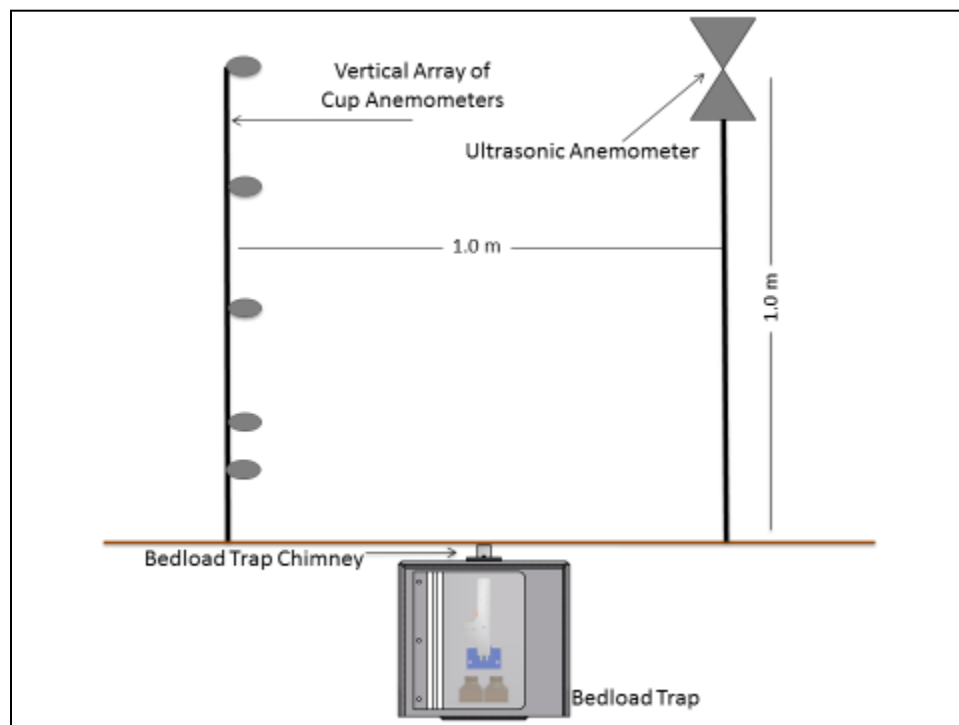
Figure 15: Field deployment diagram. The configuration of vertical array of R.M. Young cup anemometers, R.M. Young ultrasonic anemometer, and bedload trap is shown. Image is not-to-scale.

3.3.2 Data acquisition

The ultrasonic and five 3-cup anemometers were cabled to a National Instruments Data Acquisition System (NI-DAS), Model NI cDAQ-9178. The NI chassis has 32-bit counters accessed through digital modules. Using the National Instruments software LabView Signal Express, each signal was recorded at a frequency of 32Hz with a single ended ground reference (RSE), and stored as ASCII files. Bedload signals were acquired and stored using an M-Audio Delta 1010LT sound card system (SC-DAS) sampling at 44,000 Hz. The NI-DAS and SC-DAS were programmed to time-synced every 5 minutes. Bedload, sonic, and cup profile data were grouped in files as follows: runs 1-3, 4-7, 9-12 and 14-15.

3.4 Signal processing

3.4.1 Buzzer disk

Bedload particles are funneled to a 6.5 mm diameter Buzzer Disk (Audiowell Electronics (Guangzhou) Co., Ltd, Model AW1E6.5T-135E). After impacting the Buzzer Disk, grains are funneled through a 4 mm diameter funnel to a non-static tube (so that grains do not get stuck) that guides grains to a second collection vessel. Output from the sensor, after amplification, is sent to a +4dBu line level input of an M-Audio Delta 1010LT sound card system using a standard RCA plug. An external Peripheral Component Interconnect enclosure houses a sound card connected to a laptop with an ExpressCard adapter (PCI Expansion, Model PEX2PCI4), and the signal can be recorded at a sample rate up to 96,000 Hz.

The sensitivity of the Buzzer Disk was evaluated with momentum threshold tests. Single quartz sand grains, ranging in size from 0.106 to 0.5 mm, were dropped onto the face of the Buzzer Disk from heights of 20, 50 and 100 mm. From a height of 100 mm, the smallest particle that could be detected had a diameter of 0.118 mm. This information was used to set the

drop distance from the chimney aperture to the Buzzer Disk at 100 mm. For environments where finer grain sands are common, a more sensitive impact sensor (e.g., a miniphone, Ellis et al. 2009) or a greater drop height should be used. These same tests were used to resolve the background noise in the electronics. The voltage response of each grain impacting the sensor depended on the grain size and the location of impact on the sensor face and ranged from ~0.00037 to ~0.002 mV. All noise was less than 0.00025 mV.

The raw and unprocessed Buzzer Disk signals for the sample run are shown in Figures 16a-b. As a single grain hits the face of the Buzzer Disk, it causes a relatively large spike in the time series followed by a series of positive-negative oscillations over ~20 time steps when sampled at 44,000 Hz (Figure 17a). A six-step algorithm was written to reduce an oscillating signal to a single peak. Figures 17b-f illustrates the step-by-step processing used to identify grain impacts:

1) Differencing the signal magnifies the maximum positive/negative oscillation from a grain impact by subtracting the previous voltage from each observation (step 1) (Figure 17b);

2) The absolute value of the differenced signal is taken to create a continuous positive time series (step 2) (Figure 17c);

3) To isolate individual peaks, step 3 removes noise from the time series. The largest possible differenced noise was 0.00037 mV. Any values less than or equal to 0.00037mV are set to zero (step 3). In step 4, all voltages between successive voltage peaks are set to zero. After this step the time series consists only of peak values (Figure 17d).

4) The largest peak from the differenced signal is used to represent a grain impact. Steps 5 and 6 reduce adjacent peaks to zero (Figures 17e-f).

Peaks that remain after the signal processing are identified as individual grain impacts and counted to find the total number of grains impacting the sensor. Two grain impacts were counted for the example presented in Figure 16. The main assumption in this method is that there are not simultaneous grain impacts. The probability of this event is reduced by using a fast sample rate, 44,000 Hz in this case. The algorithm was tested by comparing visual versus algorithm counts during randomly sampled periods of transport. Each visual count used one second of the raw signal (44,000 observations) and identified the number of grain impacts. Manual counts were compared to the final output from the algorithm. Errors are associated with double impacts when two grains hit the sensor within 0.0001 s of one another. From these tests count differences were found to be always less than 10%, representing an under-count because the algorithm misses some near-simultaneous impacts. After processing the time series in Figure 16a, 2189 impacts were identified from the bedload signal in Figure 16b. The 10% underestimation of bedload grains from the 300 second run is about 220 grains, making the range of likely impacts between 2189 and 2409 grains. Grain impacts were aggregated to 1 s subsamples.
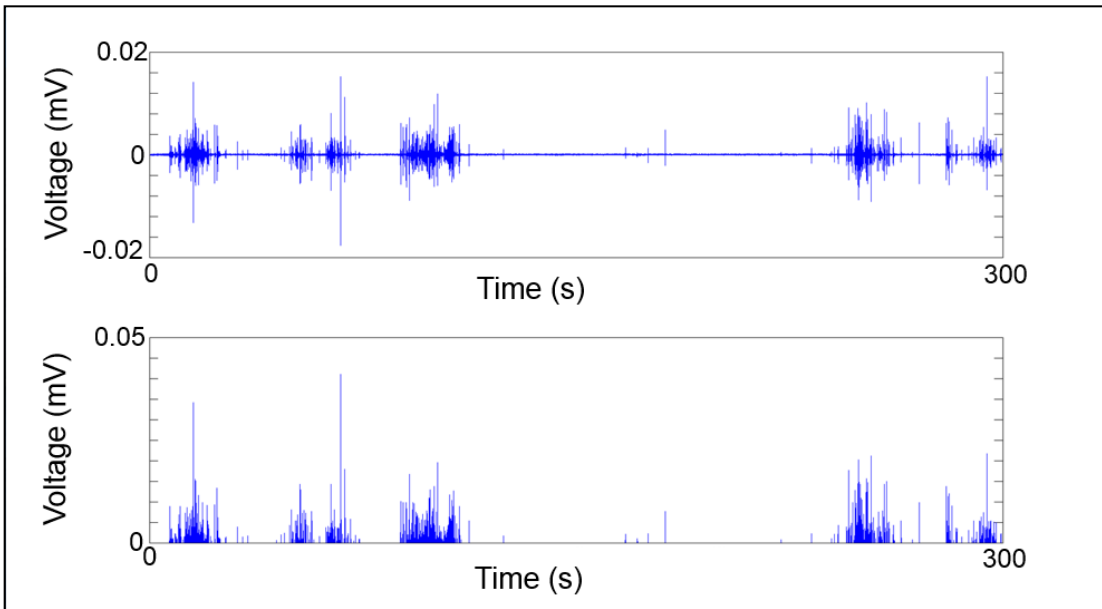
Figure 16: Buzzer Disk signal of bedload transport for a single run: a) unprocessed and b) processed data using impact detection algorithm.
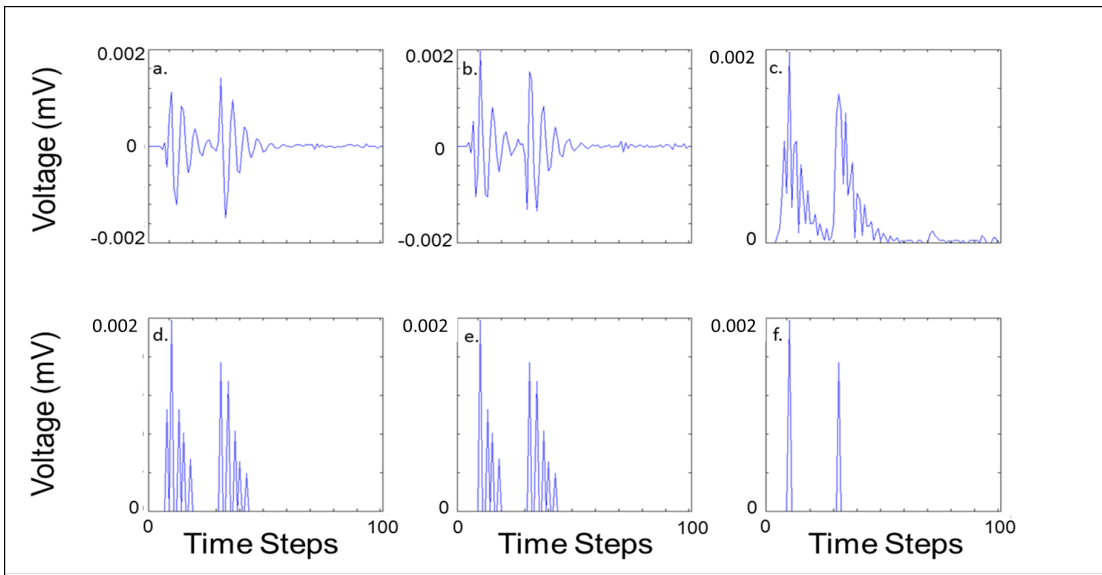
Figure 17: The 6-step post-processing algorithm written to reduce signal of single impacts to 1 peak. In this example, two peaks are identified from the algorithm.

3.4.2 Ultrasonic anemometer

Three-dimensional flow data from the ultrasonic anemometer are used to calculate shear velocity. Kaimal and Fannigan (1994) demonstrate shear velocity can be derived from Reynolds Stress (RS) calculations using high frequency, three dimensional velocity u and w,

$$u = \bar{u} + u^{'} \tag{31}$$

$$v = \bar{v} + v \tag{32}$$

$$w = \bar{w} + w \tag{33}$$

where $\bar{u}, \bar{v}$ and $\bar{w}$ are mean velocities and $u, v^{'}$ and $w^{'}$ are deviations from the mean velocities, or the eddy components of the velocity measurements. Shear velocity is a function of the horizontal shear stress imparted by the fluid flowing over the surface, and proper calculation of shear stress requires a 3-step rotation process of observed u, v and w to be appropriately oriented (Kaimal and Finnagan 1994; von Boxel et al., 2004). The following rotation process follows van Boxel et al. (2004, page 140) where observed u, v and w are denoted as u_0, v_0 and w_0. The first rotation orients u_0 into the wind direction by forcing $\overline{v_1} = 0$:

$$u_1 = u_0 \cos \theta + v_0 \sin \theta \tag{34}$$

$$v_1 = -u_0 \sin \theta + v_0 \cos \theta \tag{35}$$

$$w_1 = w_0 \tag{36}$$

where,

$$\theta = arctan \left(\frac{\overline{v_0}}{\overline{u_0}} \right) \tag{37}$$

The second rotation directs u_0 into sloping streamlines and w_0 perpendicular to streamlines where $w_0=0$:

$$u_2 = u_1 \cos \phi + w_1 \sin \phi \tag{38}$$

$$v_2 = v_1 \tag{39}$$

$$w_2 = -u_1 \sin \phi + w_1 \cos \phi \tag{40}$$

where,

$$\phi = arctan\left(\frac{\overline{w_1}}{\overline{u_1}}\right) \tag{41}$$

The third rotation orients v with streamlines and w perpendicular to streamlines forcing zero covariance between v and w i.e. $\left(\overline{v_3'w_3'}\right) = 0$:

$$u_3 = u_2 \tag{42}$$

$$v_3 = v_2 \cos\psi + w_2 \sin\psi \tag{43}$$

$$w_3 = -v_2 \sin\psi + w_2 \cos\psi \tag{44}$$

where,

$$\psi = 0.5 \; arctan\left(\frac{2\overline{v_2 w_2}}{\overline{v_2^2} - \overline{w_2^2}}\right) \tag{45}$$

After the 3-step rotation process, shear velocity will be calculated. Kaimal and Finnigan (1994; van Boxel et al., 2004) derive shear velocity via Reynolds Stress (RS):

$$RS = -\rho \overline{u'w'} \tag{46}$$

where,

$$u_* = \sqrt{\frac{RS}{\rho}} \tag{47}$$

so that,

$$u_* = \sqrt{-\overline{u'w'}} \tag{48}$$

Walker (2005) suggests a second derivation of shear velocity using the horizontal component of the RS$_\text{H}$:

$$RS_H = \rho\sqrt{\left(\overline{u'w'}\right)^2 + \left(\overline{v'w'}\right)^2} \tag{49}$$

$$u_{*RS(H)} = \sqrt{\frac{RS_H}{\rho}} = \left(\overline{u'w'}\right)^2 + \left(\overline{v'w'}\right)^2 \tag{50}$$

The three dimensional rotations minimizes the variance in the v and w components of the wind. Shear velocities calculated using Equations 48 and 50 are compared to the time-averaged shear velocity results of the vertical profile, log-linear regressions.

3.4.3 Cup anemometers

Velocity profiles were collected using cup anemometers at different heights above the surface. Cup anemometer data are first converted from voltage to wind speed (m/s) using calibration coefficients, and subsequently time-averaged. Bauer et al. (1992, p. 455) outline a simple method to take velocity profiles and calculate shear velocity based in Equation 4. In Method 1 of Bauer et al. (1992) average wind speed is plotted the y-axis of a log-linear plot with logarithmic height on the x-axis. Shear velocity is calculated using the slope, m, of a fitted linear regression, and the von Kármán constant, $K = 0.4$ as $u_* = mK$. Threshold shear velocities correspond to the initiation of bedload movement defined at specific averaging periods and threshold conditions (see section 3.5.3).

3.5 Variable derivation

3.5.1 Mean grain size, d

Grain size analysis was conducted using a laser diffraction particle size analyzer, CILAS 1180. As particles pass through a focused laser beam, the angle at which particles scatter light is inversely proportional to their size. Photosensitive detectors measured the angular intensity of scattered light to derive particle size. The output from the CILAS is a fine-scaled frequency distribution of grain counts.

Sand samples for Runs 3 and 4 were too small to be analyzed using the CILAS 1180. This necessitated a manual count and measure of these samples using ArcGIS software. Figure 18 is an example of the image used for the manual count. For each sand grain, the long and D_{50}

axis was measured. The D_{50} axis was used as this corresponds to common sieve method.   Run 3 consisted of 483 grains measured, with Run 4 consisted of 995 grains.

The grain size distribution output from the CILAS and manual counts from Runs 3 & 4 were entered into GRADISTAT, a program developed by Blott and Pye (2001). GRADISTAT outputs the average grain size, sorting, skewness and kurtosis of the sample using a number of different methods.   The volumetric percentage of each size fraction was analyzed in GRADISTAT for all runs except 3 and 4, where the frequency distribution was used.   The arithmetic Method-of-Moments calculated in GRADISTAT was used in this analysis.
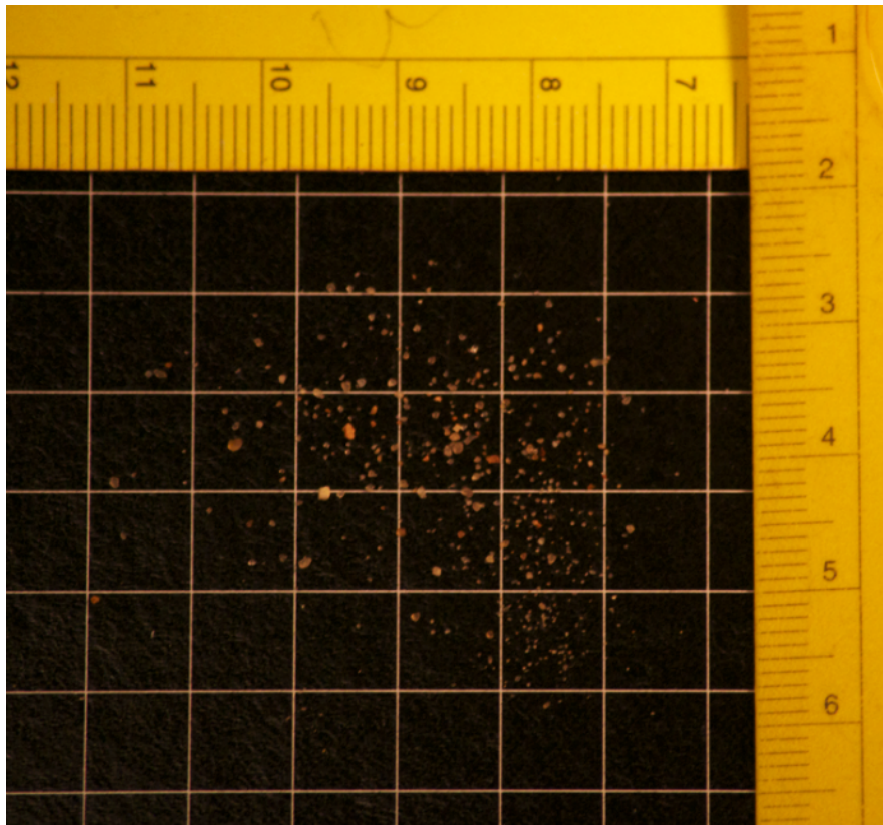
Figure 18: Manual count image for Run 3 sand sample.

Bagnold's model requires the average grain size of a population. In field tests it is common to use surface grab samples to find the average grain size. However, no surface samples were collected on the day of data collection. Captured bedload sample distributions were synthetically mixed to create a surface population sample. The percentage of each grain size fraction was converted to the equivalent weight of an theoretical 100 gram sample. The size fraction weight was then summed for all captured bedload samples. The percentage of each grain size fraction in the synthetic population was calculated and input into GRADISTAT to resolve grain size statistics.

3.5.2 Grain density, ρ_S, fluid density, ρ, and the gravitational constant, g

Global standards of particle and fluid density, as well as the gravitational constant, are known and commonly used in scientific and engineering applications. However, in error analysis it is important to briefly expand on these variables. The gravitation constant varies with altitude and latitude. At sea level, the gravitational constant ranges from 9.78 m/s^2 to ~9.84 m/s^2 from the equator to the poles. At the study site, ~2° latitude, the gravitational constant is 9.78 m/s^2.

Sand samples were examined under a microscope to determine the type of sand. Grains were angular quartz, in agreement with Jimenez et al. (1999). To confirm density estimates, a pycnometer was used to directly measure particle density. The results consistently indicated sand particles had a density of 2650 $\frac{\text{kg}}{\text{m}^3}$. Fluid density is dependent upon the temperature, pressure, and water vapor content. Standard atmospheric pressure at sea level is assumed constant at 14.695 psi. The average temperature during data collection was 80°F. The amount of water vapor in the air was not directly measured. The northeasterly winds observed were coming straight off the ocean, suggesting the air had a lower density (lighter air) due to the

presence of some percentage of water vapor. However, no direct measurements of humidity were measured and we assume dry air. The fluid density of dry air at 80°F is $1.204 \frac{\text{kg}}{\text{m}^3}$.

3.5.3 Threshold shear velocity, u_{*t}

Careful consideration was taken to define appropriate averaging periods to calculate shear velocity estimates corresponding to the threshold of motion. Near the threshold sand transport is intermittent (Butterfield, 1991, 1993; Stout and Zobeck, 1997; Schönfeldt, 2004; Wiggs et al., 2004b; Davidson-Arnott and Bauer, 2009). Shear velocities momentarily exceeding the fluid threshold (initiating transport) are followed by shear velocities decreasing below the dynamic threshold necessary to sustain movement (ceasing transport) (Schönfeldt, 2004). These high frequency fluctuations corresponding to the initiation of motion occur on time scales of tenths of a second (Rasmussen and Sørensen, 1999; Namikas et al, 2003). Yet, reliable estimates of shear velocity ($r^2 > 0.98$) often require averaging periods on the order of tens of seconds to minutes (Butterfield, 1991; Namikas et al., 2003; van Boxel et al., 2004). Longer averaging periods have greater variance and therefore a greater probability for error (Namikas et al. 2003). This creates a problem in choosing the appropriate averaging periods: shorter averaging periods have lower variance, smaller number of reliable velocity profiles and temporally correspond more closely to the threshold of motion, while longer averaging periods have a higher variance and a larger number of reliable velocity profiles but smooth out high frequency velocity fluctuations associated with exceedance of the threshold. While no general consensus has been made in specific reference to experiments concerning the threshold of motion, Rasmussen and Sørensen, (1999) suggest using shorter averaging periods to correspond with the time scale of transport, and Namikas et al. (2003) recommend an averaging period of 10-15 s for optimal reliability and reduced variance in deriving shear velocities from

conventional profile data. For this reason, threshold shear velocities were averaged over periods of 5, 10, 15 and 20 s.

Threshold exceedance occurred on time scales less than 1 s as detected by the bedload trap. The time series of observed bedload transport was aggregated from 44,000 Hz to 1 s and a binary time series of no transport (0) and transport (1) for each second was created to detect threshold exceedance. As stated above, shear velocities were time-averaged at 5, 10, 15 and 20 s to increase reliability and decrease variance in shear velocity estimates. However, defining the appropriate bounding seconds in the time series relative to second of threshold exceedance was difficult. If the averaging interval is centered over the second of transport, half of the averaging interval includes shear velocities when the threshold was not yet exceeded. If the averaging period begins with the second the threshold is exceeded, the averaging intervals includes only shear velocities once the threshold was exceeded. This debate was partially resolved by establishing multiple threshold conditions.

Three threshold conditions were defined (Figure 19): 'no transport', 'centered' and 'transport'.   At each of these conditions, 5, 10, 15 and 20 s averaging periods are used to derive threshold shear velocity. In other words, each condition has four time-averaged threshold shear velocities. 'No transport' refers to shear velocities averaged over the time period just prior to particle movement, where the last second in the averaging period (5, 10, 15, or 20 s) is the second before transport begins. During 'no transport' condition no bedload particles are in motion, and should be below Bagnold's predicted fluid threshold. 'Centered' is the threshold condition where shear velocity is averaged over periods centered on the second transport begins, i.e. no transport occurs half of the averaging period and half of the period transport is continuous. The 'transport' condition is averaged over periods beginning with the second of initiation. All seconds during the 'transport' condition must have at least 1 grain in motion.
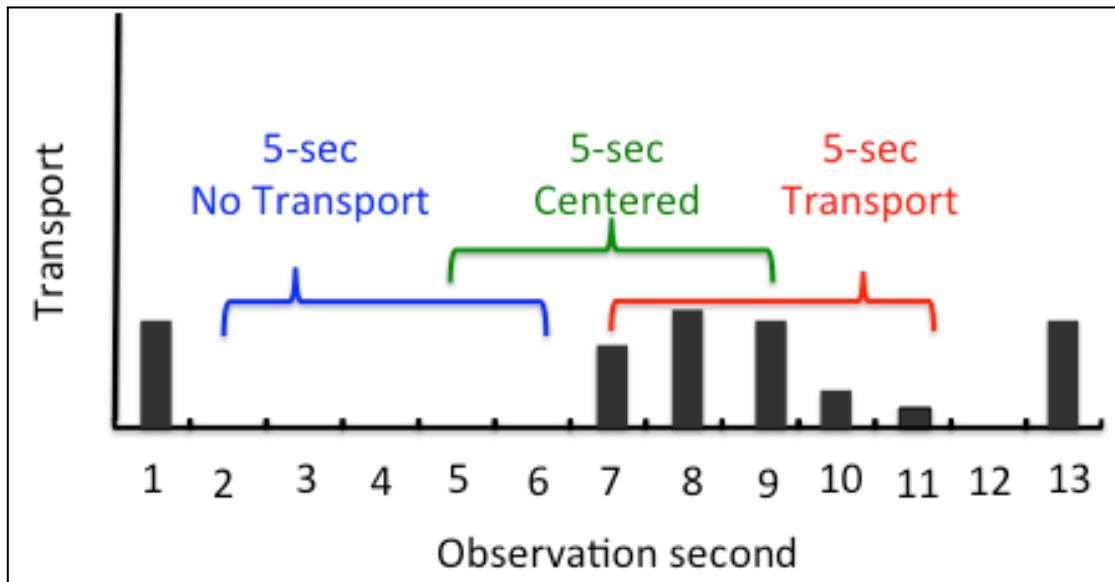
Figure 19: Schematic illustrating time-averaged shear velocity corresponding to the initiation of bedload transport. Black bars indicate transport amount. In this example, the initiation of bedload transport begins during the 7th second. The "No Transport' shear velocity averaging period is from second 2-6, 'Centered' is 5-9, and 'Transport' is observation 7-11.

Two sets of wind observations were collected to calculate shear velocity for each threshold condition and averaging period: (i) calibrated and rotated three-dimensional sonic anemometer data using Equations (34-36), and (ii) a vertical profile of cup anemometer data using von Karman's Law-of-the-Wall, (4). For the cup anemometer data, time-averaged velocity profiles with $r^2 > 98\%$ were used to calculate field-derived threshold shear velocities. Sonic and velocity profiles were compared to see if the two resolve the same shear velocity for each threshold condition and averaging period. The Root-Mean Squared Error (RMSE) was calculated for threshold shear velocities and observed A values to test errors between predicted

and observed u_{*t} (Hypothesis I). One and two-sample t-tests were used to test for statistical differences in mean values.

3.6 Threshold wind speed

Wind speed fluctuates near the threshold causing intermittent transport over a surface (Stout and Zobeck, 1997; Rasumessen and Sørensen, 1999; Schönfeldt, 2004; Davidson-Arnott and Bauer, 2009) and as such, wind speeds measured at the initiation of bedload movement were calculated to tests for trends between threshold wind speed and average grain size. The lowest anemometer (100 mm above the bed) is subsampled to 1 s to correspond to the bedload time series. The first second of detected transport in the 5 s averaging period for 'centered' and 'transport' threshold conditions was used in the 1 s wind speed analysis, and the last second prior to transport was used for 'no transport' condition. Threshold wind speeds correspond to the second of bedload initiation. Two-sample t-tests are used to test for differences between finer and coarser grain threshold wind speeds.

Additionally, the effects of gusts on the entrainment of particular particle sizes were tested using 5 s averaging of wind speed around the threshold of motion. Wind speed from the lowest anemometer was averaged during periods of time when the threshold was exceeded for 5 continuous seconds. The difference between these 5 s transport periods and the average speed without transport immediately prior particle initiation was used to test for grain size dependence on gusts. Two and five second averages were used to quantify the step increase, if any were detected, in wind speed associated with the initiation of motion.

3.7 Multiple regression and model comparison

Multiple linear regression is used to develop a model of the fluid threshold based on field-observed threshold shear velocities and grain size distribution statistics (mean, sorting, skewness and kurtosis). The highest temporal resolution of grain size data is 5 minutes. Because of this, threshold shear velocities for each threshold condition and averaging period are averaged separately for each 5-minute run to conduct the regression analysis.

Two dependent variables are modeled against grain size statistics in this analysis: (1) observed threshold shear velocity and (2) observed A. The predictive power of each descriptive statistic is modeled individually to elucidate the independent variables with the strongest relationship (r^2) and statistical significance $(\rho < 0.05)$ with each dependent variable. Subsequent analysis combines the most significant predictor variables to resolve the model with the greatest predictive power. If statistically significant, the model developed from the multiple linear regression analysis was tested against Bagnold's model, and all threshold shear velocity models presented in Table 2.

CHAPTER IV

EXPERIMENTAL RESULTS AND DATA ANALYSIS

Transport was intermittent throughout data collection yielding 95, 76 and 74 threshold exceedances for 'no transport', 'centered' and 'transport' conditions at a 5 s averaging period. A total of 12, 5-minute clean sample runs of vertical velocity profiles, three-dimensional flow velocities, and bedload transport were collected. Three 5-minute sample runs were excluded from analysis due to insufficient data collection. Bedload transport was captured in the bedload trap and subsequently analyzed for grain size distribution statistics. The following results and analysis presented here provide the means to test Hypotheses Ia-b and II. The null hypotheses in each case are:

$H_0(Ia)$: Bagnold's A constant 0.1 is equal to the observed A

$H_0(Ib)$: Equation 27 is equal to the observed A

$H_0(II)$: Bagnold's u_{*t} is equal to the observed u_{*t}

These hypotheses will be tested using a two-sample t-test to determine if predicted versus observed means are statistically different.

4.1 Average grain size, d

Captured bedload samples of the naturally-mixed sand of Jericoacoara, Brazil fall into two main groups: a set of coarser grains and a set of medium size grains. The grain size distribution statistics for each run are shown in Table 4. Coarser bedload samples have average grain sizes ranging from 0.79-0.88 mm and sorting values of ~0.0008 mm. These samples are consistently well sorted and characterized by a symmetrical, mesokurtic distribution (Figure 20).

The finer set of samples are moderately sorted, with average grain sizes ranging from 0.31-0.40

mm and sorting values ranging from 0.0002-0.0003 mm. The finer sample distributions are

finely-skewed to symmetrical and platykurtic. The finer sand distributions show slightly more

variability, but this variability is likely attributed to the manual counts of Runs 3 and 4 versus the

volumetric percentages from the CILAS for all other finer grain samples. The strong

similarities within the coarser and finer populations suggest selective transport either from the

fluid forces, surface configuration, or both.

Table 4: Arithmetic Method of Moments grain size distribution descriptive statistics

Run	Mean Size		Sorting		Skewness		Kurtosis	
1	0.83	Coarse Sand	0.24	Well Sorted	0.0008	Symmetrical	0.0034	Mesokurtic
2	0.31	Medium Sand	0.15	Moderately Sorted	0.0003	Symmetrical	0.0019	Platykurtic
3	0.34	Medium Sand	0.18	Moderately Sorted	0.0009	Symmetrical	0.0037	Platykurtic
4	0.40	Medium Sand	0.24	Moderately Sorted	0.0008	Fine Skewed	0.0032	Platykurtic
5	0.79	Coarse Sand	0.24	Well Sorted	0.0008	Symmetrical	0.0035	Mesokurtic
7	0.31	Medium Sand	0.15	Moderately Sorted	0.0003	Symmetrical	0.0019	Platykurtic
9	0.87	Coarse Sand	0.24	Well Sorted	0.0008	Symmetrical	0.0034	Mesokurtic
10	0.88	Coarse Sand	0.23	Well Sorted	0.0008	Symmetrical	0.0033	Mesokurtic
11	0.85	Coarse Sand	0.24	Well Sorted	0.0008	Symmetrical	0.0033	Mesokurtic
12	0.80	Coarse Sand	0.26	Well Sorted	0.0009	Symmetrical	0.0037	Mesokurtic
14	0.32	Medium Sand	0.15	Moderately Sorted	0.0002	Fine Skewed	0.0018	Platykurtic
15	0.32	Medium Sand	0.15	Moderately Sorted	0.0002	Fine Skewed	0.0019	Platykurtic
[†]Entire Surface	0.59	Medium Sand	0.32	Poorly Sorted	0.0005	Very Fine Skewed	0.0028	Platykurtic
[†] Surface populatoin statistics were calculated by synthetically mixing all bedload sample grain size distributions								
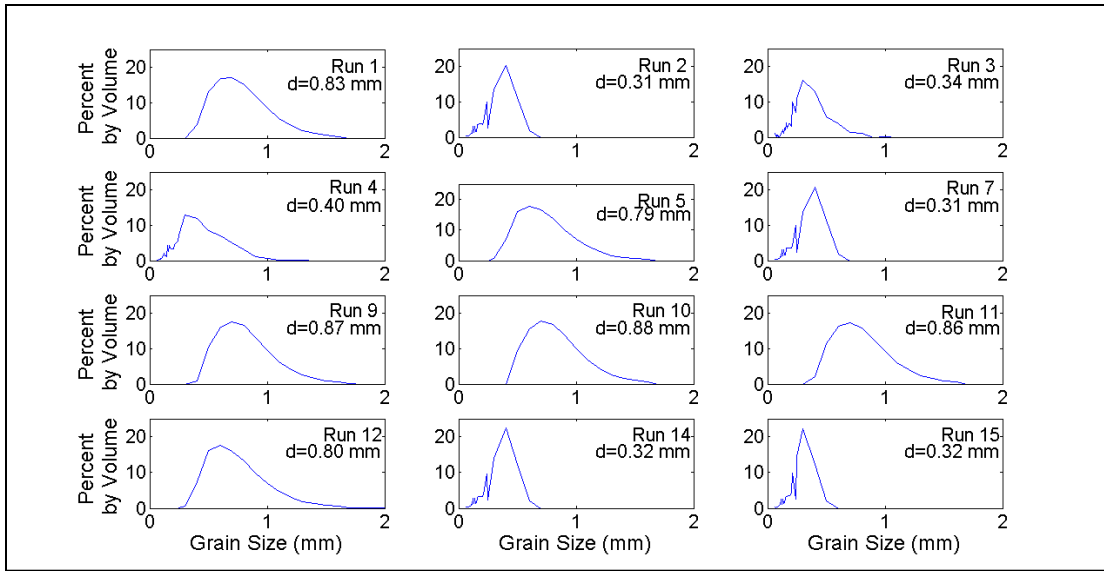
Figure 20: Variable bin width grain size distribution for each run with mean grain size used for threshold tests.

The surface population consisted of two groups of samples that are each independently unimodal with little variation in distribution type (Figure 20). These two populations, along with the visual evidence of size segregation shown in Figure 12, suggest the surface population was composed of a mixed size distribution. However, no surface grab samples were taken on the day of data collection. The absence of a grab sample prompted the artificial mixing of all bedload sample grain size distributions to recreate the surface population distribution. The synthetically mixed grain size distribution is polymodal, poorly sorted and platykurtic (Figure 21) with an average grain size of 0.59 mm and sorting of 0.32 mm (Table 4). Assuming the synthetically mixed population adequately represents the surface population, the average grain size is greater (less) finer (coarser) captured bedload populations. This suggests particles in motion are not of

the average grain size, but rather of the coarser and finer fractions that have been laterally segregated, similar to the results of Bauer (1991).
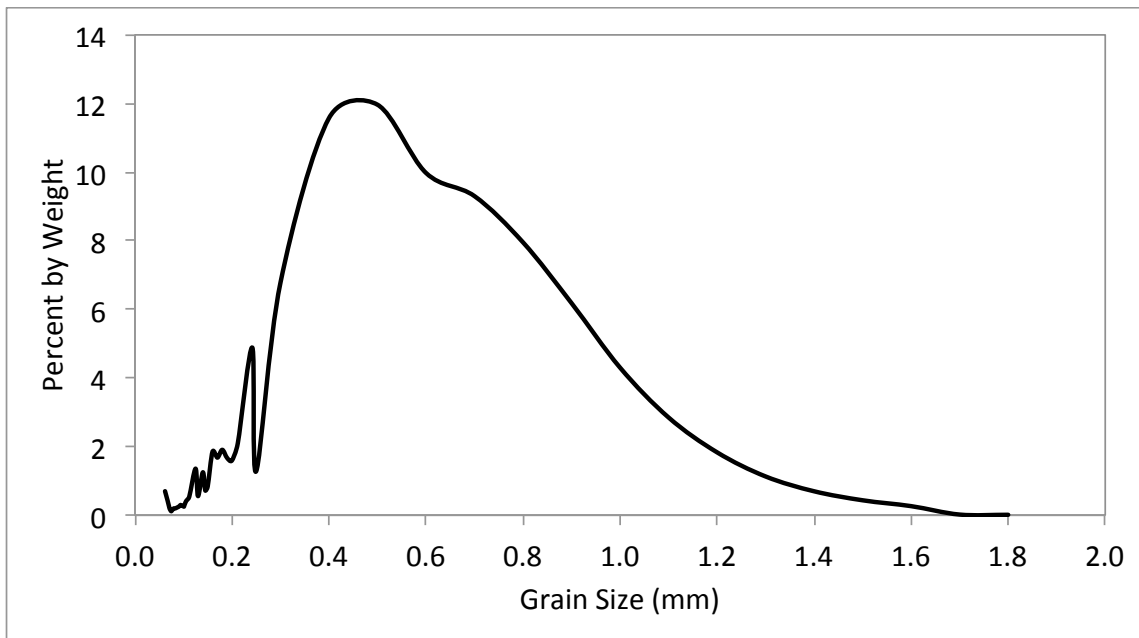
Figure 21: Synthetically mixed surface population using grain size distribution of all bedload samples.

Small scale ripples on the surface consisted of coarser particles in the crest with finer particles in the trough (Figure 12). This organization of coarser particles in the crests of ripples is in agreement with the findings of Willetts and Rice (1989). They found surface creep to dominate transport up the windward face of a ripple diminishing in speed as the particles reach the crest. This process creates a region of creep deposition at the crest, producing coarse grain ripples. Ripple migration throughout the experimental runs was minimal, but the presence of

ripples organizing coarser and finer particles may have caused the selective transport of coarser and finer material into the bedload trap. As finer particles lay in the troughs of the ripples, these particles would have been within the flow separation zone reducing the exposure to shearing forces. Shear stress imparting a greater fluid force on the windward face of the coarse grain ripples, may have propelled coarser particles to creep up and over the leeward face of the ripple and into the bedload trap. Coarser grains in the ripples were likely more exposed to shearing forces than finer particles. Additionally, coarser particles on a bed of fine particles inherently have a lower pivoting angle and thus are more susceptible to fluid forces. Finer particles in a bed of coarser particles also have a much higher pivoting angle (Wilcock, 1988). These particles may have only been moved under greater shearing forces than typically predicted for finer particles.

4.2 Observed u_{*t}

Bedload transport was highly intermittent throughout data collection which yielded a substantial number of threshold shear velocities corresponding to the initiation of bedload movement. The 300 s time series of bedload transport for each run is shown in Figures 22-23. The number of grains impacting the sensor in each second shows the magnitude of bedload transport. No specific number of grains corresponded to threshold exceedance (e.g 1, 10 or 100 grains). However, the first second of the threshold of motion being exceeded, the number of grain(s) ranged moved ranged from 1-34 with most initiation seconds having 1-10 bedload grains. A greater number of bedload particles impacted the Buzzer Disk per second than those impacting the sensor during finer grain runs (Figure 22-23). This suggests coarser bedload particles were more susceptible to movement than the finer grain particles.
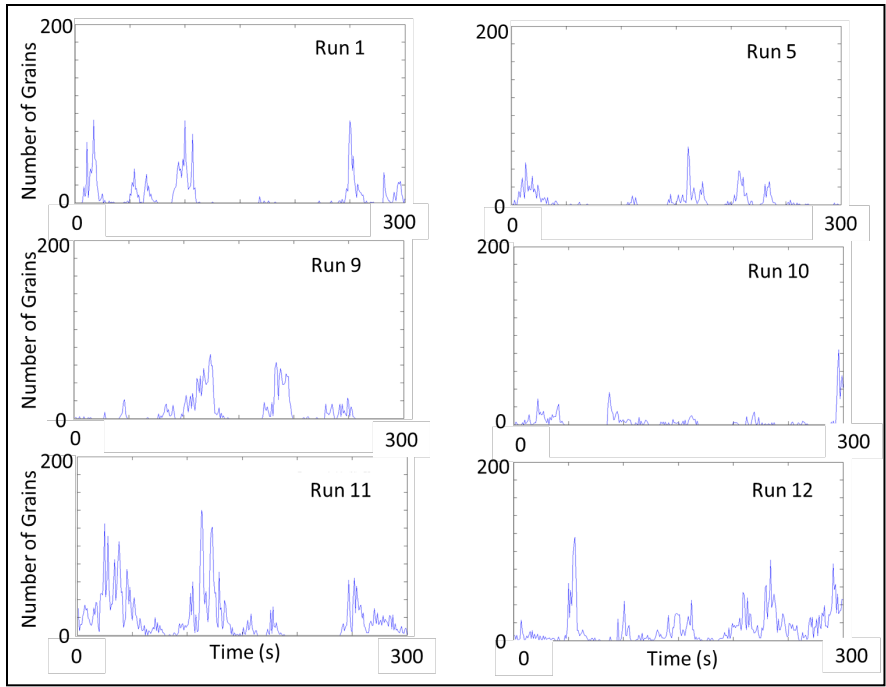
Figure 22: Time series of bedload transport during all coarser grain runs.
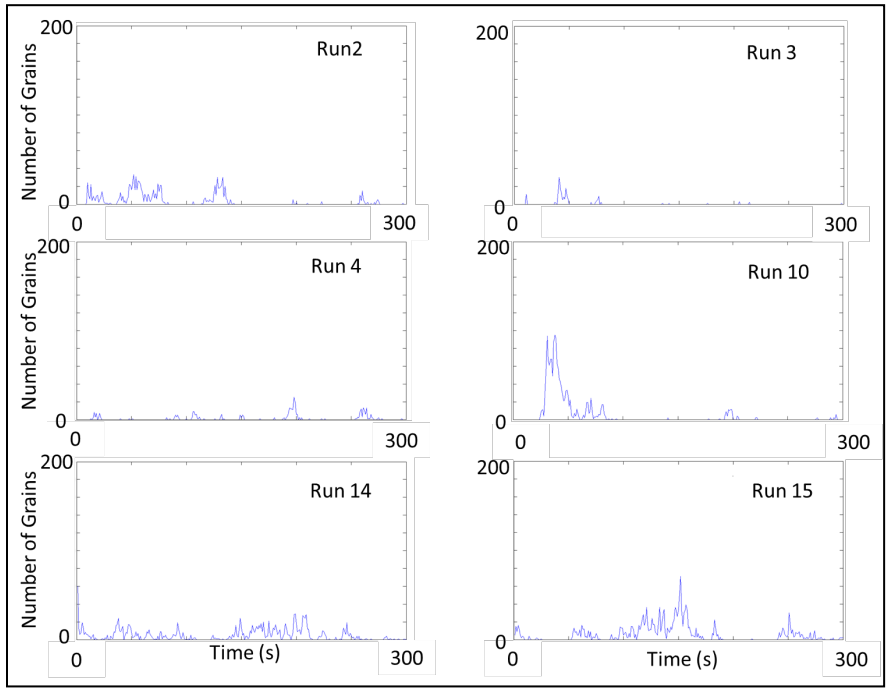
Figure 23: Time series of bedload transport during all finer grain runs.

Observed threshold shear velocity was calculated using only velocity profiles with $r^2 > 98\%$ via the methods of Bauer et al. (1992). Visual inspection of the 5-cup profile show a distinct kink at height 0.74 m (Figure 24). 30-minute averages of cup anemometer data indicate these profiles do not exhibit the typical logarithmic shape of a turbulent boundary layer. In Figure 24, the cup anemometer deployed at 0.74 m appears to have a systematic offset. Removing the 0.74 m cup anemometer for the same time period results in a series of profiles that conform to the expected shape of a velocity profile (Figure 25). The source of the kink in the 5-cup velocity profile is unknown, but may arise from mechanical differences between the anemometers or inappropriate calibration coefficients. To determine if the offset in the 5-cup profile resulted in a lower number of useable samples, the number of log-linear regressions with $r^2 > 98\%$ for the 5- and 4-cup profiles were counted, Table 5. The 4-cup profile consists of a greater number of profiles with $r^2 > 98\%$, and consequently, a larger number of threshold shear velocity samples to analyze Hypotheses I & II. Therefore, data collected using the 0.74m cup anemometer was removed from this analysis and only the 4-cup anemometer profiles shear velocities are used.
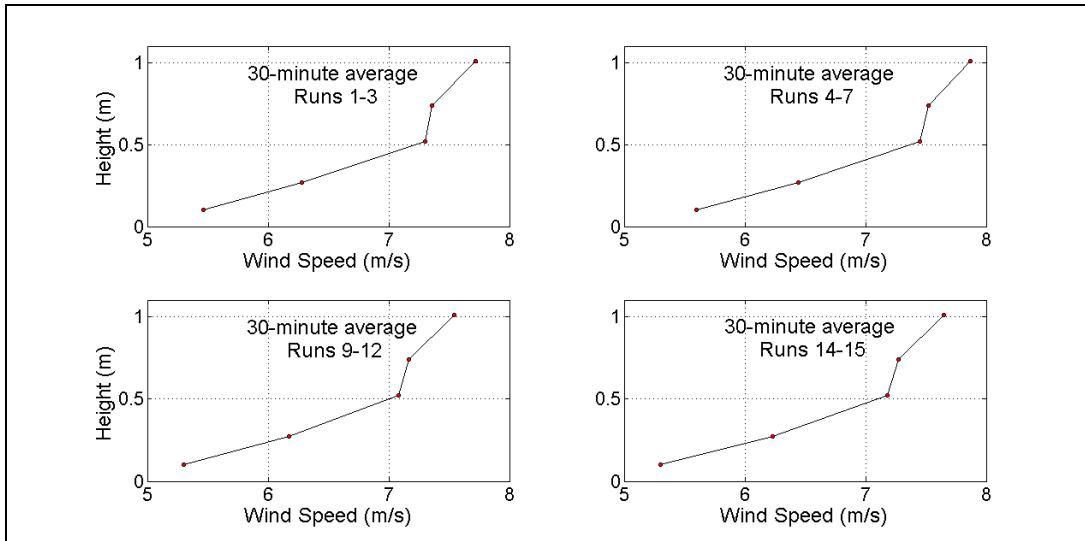
Figure 24: 5-cup, 30-minute averaged velocity profiles for all runs. Wind speed is plotted on the x-axis for easier visualization of the velocity profile. The anemometer at 0.74 m shows a distinct kink in the velocity profile with a systematic offset.
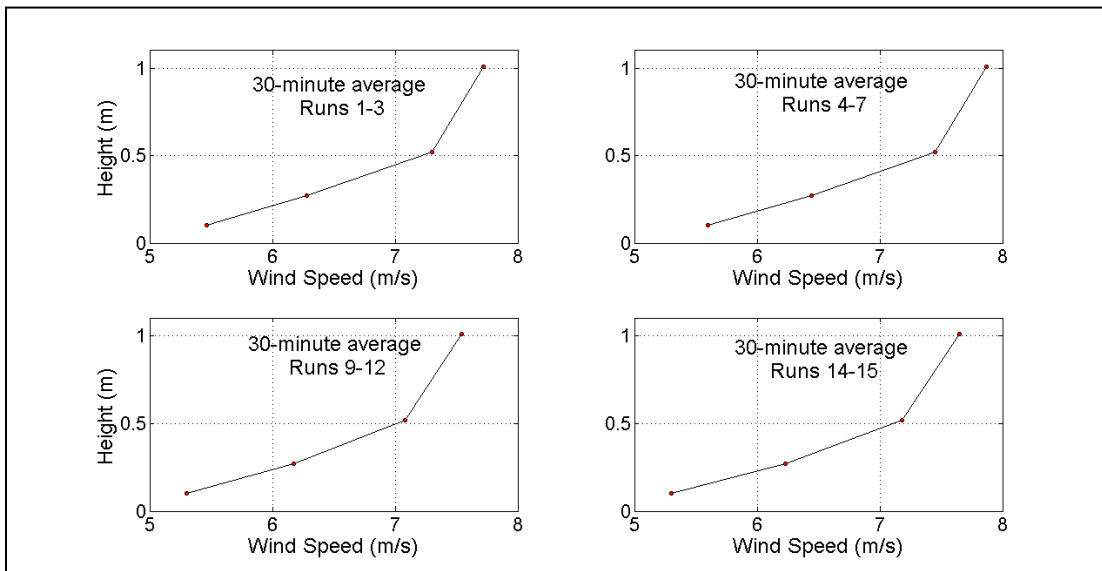
Figure 25: 4-cup, 30-minute averaged velocity profiles for all runs. Wind speed is plotted on the x-axis for easier visualization of the velocity profile.

Table 5: Comparison of 5-cup vs. 4-cup profile with $r^2 > 0.98$

Profile	No Transport	Centered	Transport
5-cup	142	69	118
4-cup	145	85	138

Three methods were used to resolve shear velocity calculations: (i) log-linear regressions of the vertical velocity profile following the methods of Bauer et al. (1992) (Figure 26a); (ii) Reynolds Stress decomposition, Equation (48) (Figure 26b); and (iii) Reynolds Stress decomposition rotated into the horizontal plane (Equation 50), (Figure 26c). Only shear velocities that correspond with velocity profile regressions having $r^2 > 98\%$ are shown. 'Transport' (points), 'centered' (plus signs) and 'no transport' (squares) thresholds conditions are plotted in Figure 26 for each calculation method over averaging periods of 5, 10, 15 and 20 s.
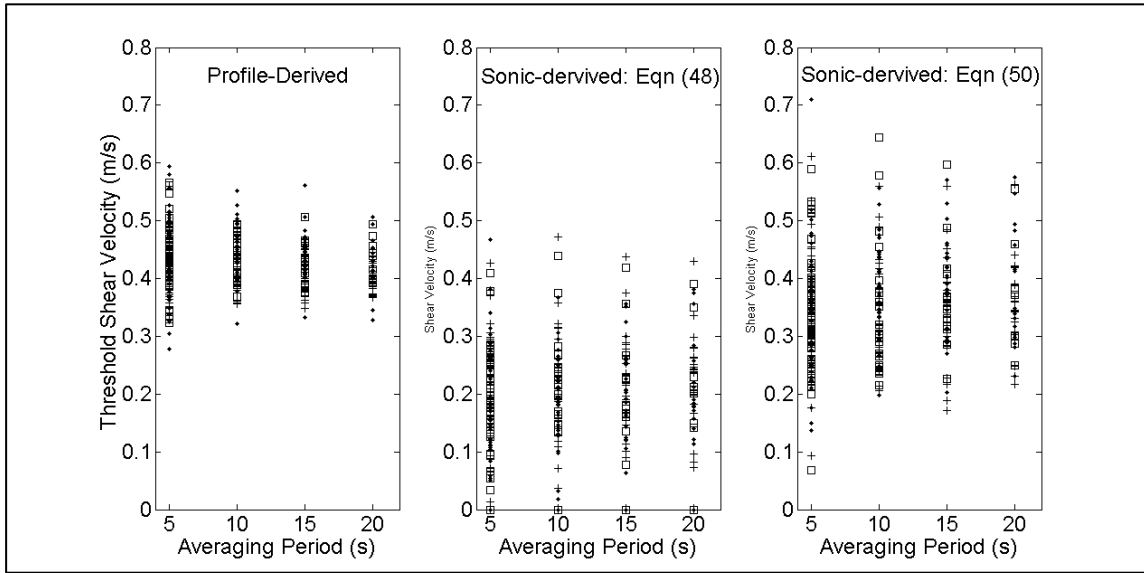
Figure 26: Shear velocity results for three different derivation methods for each threshold condition. 'Transport' periods are symbolized by points, 'centered' by '+' and 'no transport' by squares.   a) Log-linear regressions of the vertical velocity profile, b) ultrasonic data using Reynolds Stress from Equation (48), and c) ultrasonic data using Reynolds Stress rotated into the horizontal from Equation (50).

Several observations can be made from Figure 26. Increasing the averaging period results in a smaller variance, σ^2, of profile-derived shear velocity (Table 6), concurring with Namikas et al. (2003). However, this is not the case for ultrasonic-derived methods. Variance does not show a decreasing trend with increasing averaging period for shear velocities calculated via Equations 48 and 50. The only exception is the decrease in shear velocity variance calculated using Equation 50 during 'no transport' conditions.

Table 6: Average threshold shear velocity and variance of shear velocities for each calculation method.

Threshold Condition and Averaging Period	u_{*t} (m/s), σ^2 (m^2/s^2)		
	Profile-derived	Equation 48	Equation 50
No Transport			
5 s	0.43, 0.002	0.17, 0.014	0.34, 0.008
10 s	0.41, 0.001	0.19, 0.011	0.35, 0.007
15 s	0.41, 0.001	0.19, 0.013	0.34, 0.007
20 s	0.40, 0.000	0.21, 0.009	0.35, 0.006
Centered			
5 s	0.43, 0.003	0.15, 0.013	0.34, 0.011
10 s	0.43, 0.001	0.18, 0.014	0.34, 0.013
15 s	0.43, 0.001	0.20, 0.011	0.37, 0.008
20 s	0.44, 0.001	0.21, 0.013	0.37, 0.009
Transport			
5 s	0.43, 0.004	0.15, 0.012	0.33, 0.010
10 s	0.45, 0.002	0.19, 0.006	0.37, 0.006
15 s	0.44, 0.002	0.19, 0.008	0.39, 0.007
20 s	0.43, 0.002	0.21, 0.009	0.38, 0.010

Each method results in considerably different estimates of shear velocity (Table 6). Shear velocities from Equation 48 (50) are 35-49% (12-22%) smaller than profile-derived shear velocities. This suggests errors in the threshold shear velocity estimates for at least two of the methods. Using Reynolds Stress decomposition to derive shear velocity estimates from ultrasonic anemometer data has been reported to result in different estimates of shear velocity when compared to a co-located velocity profile collected via cup anemometers (Walker, 2005). Errors arising from ultrasonic anemometers have been attributed to distortion effects and turbulence dissipation typically found over complex terrain (Walker, 2005). Deployment height

and sampling frequency used here correspond with those suggested by van Boxel et al., (2004) and Walker (2005). However, van Boxel et al. (2004) found the shortest statistically significant averaging period for calculating shear velocity from ultrasonic anemometer data to be 120 s. Shear velocity calculated using ultrasonic anemometers here are much shorter than van Boxel et al. suggested averaging period. The increased variance in both ultrasonic anemometer method may be due to the short averaging periods used here.

On the other hand, velocity profiles collected via cup anemometers have offered reliable estimates of threshold velocities, and as such, are the most common method to derive shear velocity in field experiments. The profile method directly measures velocities at various heights above the surface and using the Law-of-the-Wall. At the moment, this concept has been repeatedly used to model the vertical deformation within the boundary layer. The reduced variance with the profile-derived shear velocities (Table 6) and the short averaging period for ultrasonic anemometers suggest this profile-derived shear velocity provides more stable estimates. Because of the potential sources of uncertainty in the ultrasonic anemometers and reduced variance of the profile-derived shear velocities, only profile-derived shear velocities are used to in this analysis.

The number of all profile-derived u_{*t} for each run is shown in Table 7. Bagnold's predicted threshold is based on the average grain size for each bedload sample, i.e. each run has a single average grain size, and therefore, a single predicted shear velocity (Table 7). Bagnold's model predicts threshold shear velocities ranging from 0.26-0.30 m/s for the finer bedload runs, and 0.42-0.44 m/s for the coarser grain runs. These two ranges are narrow and distinctly different due to the two separate grain size populations. If Bagnold's model is correct, observed values should match these two ranges. Histograms of observed shear velocities with $r^2 > 0.98$ for each averaging period and threshold condition are shown in Figure 27. With increasing

averaging period, the number of reliable shear velocities decreases. Shear velocities typically exhibit normal distributions. This is contradictory to Bagnold's distinct ranges of threshold shear velocities for these two grain populations. The only case that resembles a moderately bimodal distribution is the 5 s averaging period for 'centered' conditions.

Table 7: The number of velocity profiles $(r^2 > 98\%)$ u_{*t} for each averaging period and threshold condition.

Run	Average D (mm)	Bagnold fluid u_{*t} (m/s)	No Transport				Centered				Transport			
			5 (s)	10 (s)	15 (s)	20 (s)	5 (s)	10 (s)	15 (s)	20 (s)	5 (s)	10 (s)	15 (s)	20 (s)
1	0.83	0.43	11	5	2	2	7	3	1	0	7	4	2	2
2	0.31	0.26	9	6	5	5	2	2	1	1	4	3	3	3
3	0.34	0.28	9	8	7	7	2	0	1	0	1	1	0	0
4	0.40	0.30	14	8	4	2	6	1	1	1	4	2	1	1
5	0.79	0.42	10	6	4	3	6	2	0	0	5	4	3	3
7	0.31	0.26	8	6	5	4	7	2	1	1	3	2	2	2
9	0.87	0.44	9	5	2	1	6	4	3	1	6	4	3	3
10	0.88	0.44	6	5	4	3	14	2	1	1	8	3	1	1
11	0.85	0.43	2	1	1	1	4	2	2	1	6	6	4	4
12	0.80	0.42	5	0	0	0	6	2	0	0	9	5	4	2
14	0.32	0.27	5	3	0	0	8	2	1	0	13	8	4	0
15	0.32	0.27	7	3	3	3	8	3	2	2	8	4	4	0
Total	-	-	95	56	37	31	76	25	14	8	74	46	31	21
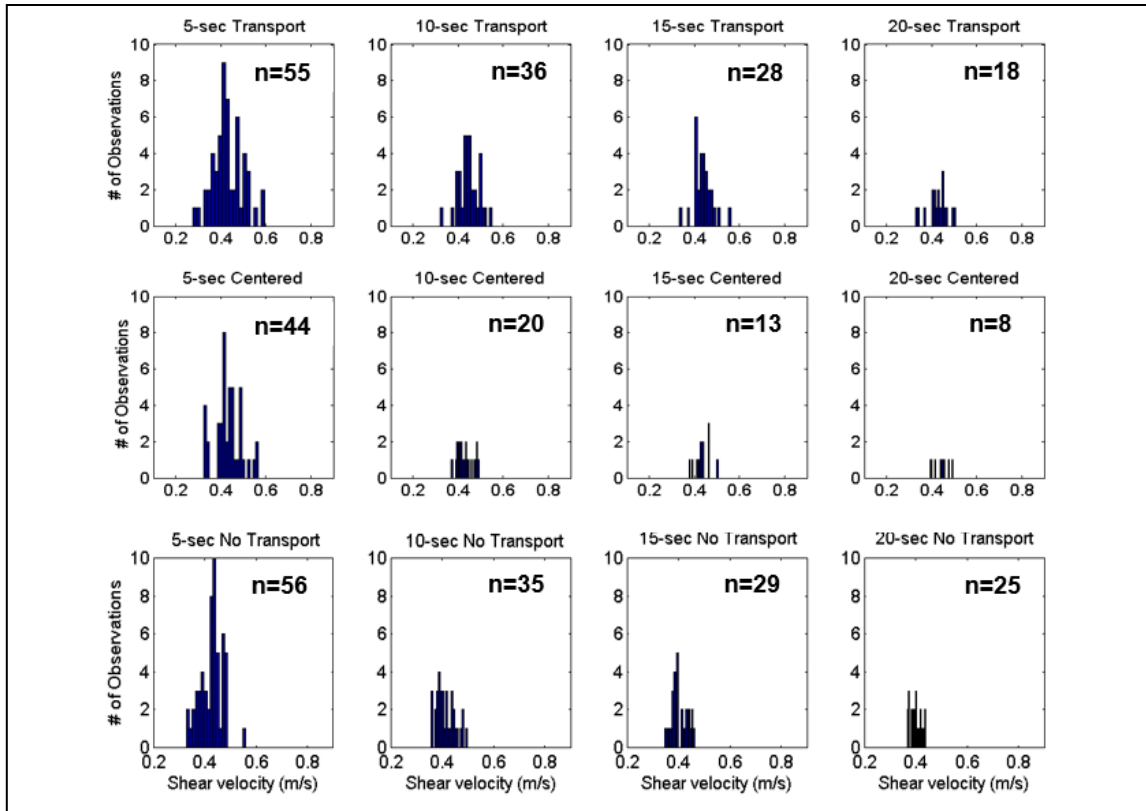
Figure 27: Histograms showing distributions of field-observed threshold shear velocities for each averaging period and threshold condition.

4.3 Observed *A*

The observed threshold shear velocities in Figure 27 are used to resolve observed *A* values based on the average grain size per run (Table 7). Observed *A* for 'transport' and 'centered' conditions are shown in Figure 28 and range from $0.07 - 0.23$. As the averaging interval increases, separation between observed *A* varying about 0.1 and 0.18 also increases. This suggests Bagnold's *A* is not constant or a function of Equation 27, and is marked by more (less) variability in the *A* parameter at shorter (longer) averaging periods. The finer grain

population has much greater observed *A* than Bagnold's constant and Equation 27 indicating

error in either Bagnold's model or his *A* parameter.
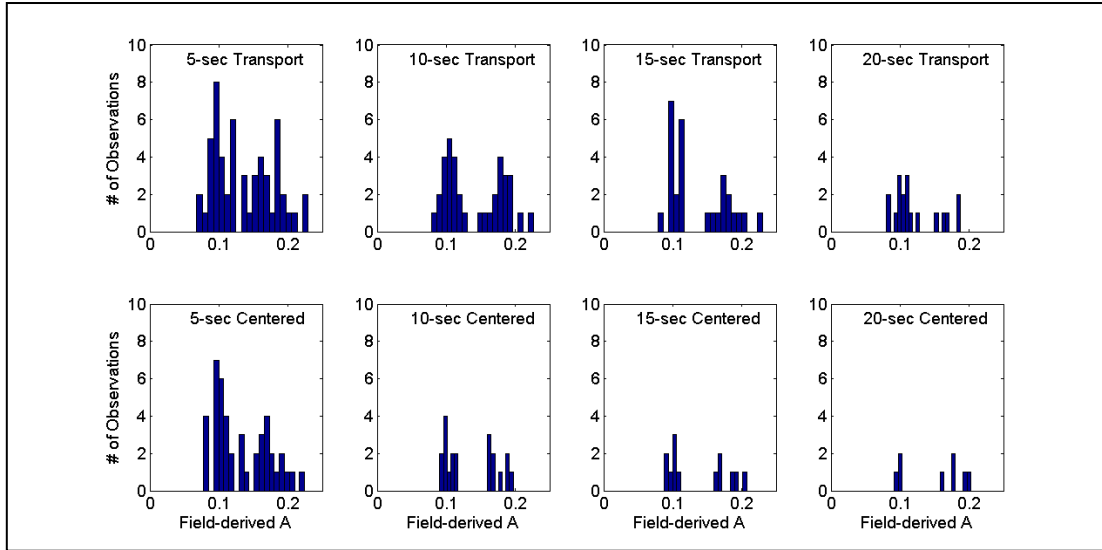
Figure 28: Histogram of field-derived *A* for observed threshold shear velocities for 'centered' and 'transport' conditions.

The RMSE between each individual field observation of *A* and Bagnold's *A* (Equation 27) was quantified to asses the visual variability of observed *A* from predicted seen in histograms (Figure 29). RMSE is approximately ~0.05 for all averaging periods for each threshold conditions. Interestingly, the 20 s averaging period exhibits the greatest and lowest RMSE with 'centered' conditions having an RMSE of 0.06, while RMSE for 'transport' conditions is 0.04. This is likely a function of the small sample size for each condition. The standard error plotted with Bagnold's *A* in Figure 29 shows field measurements within ±50% of Bagnold's *A*. Finer

grain shear velocities largely exceed 1 standard error of Bagnold's *A* value and imply these

populations are not well represented by Bagnold's model.
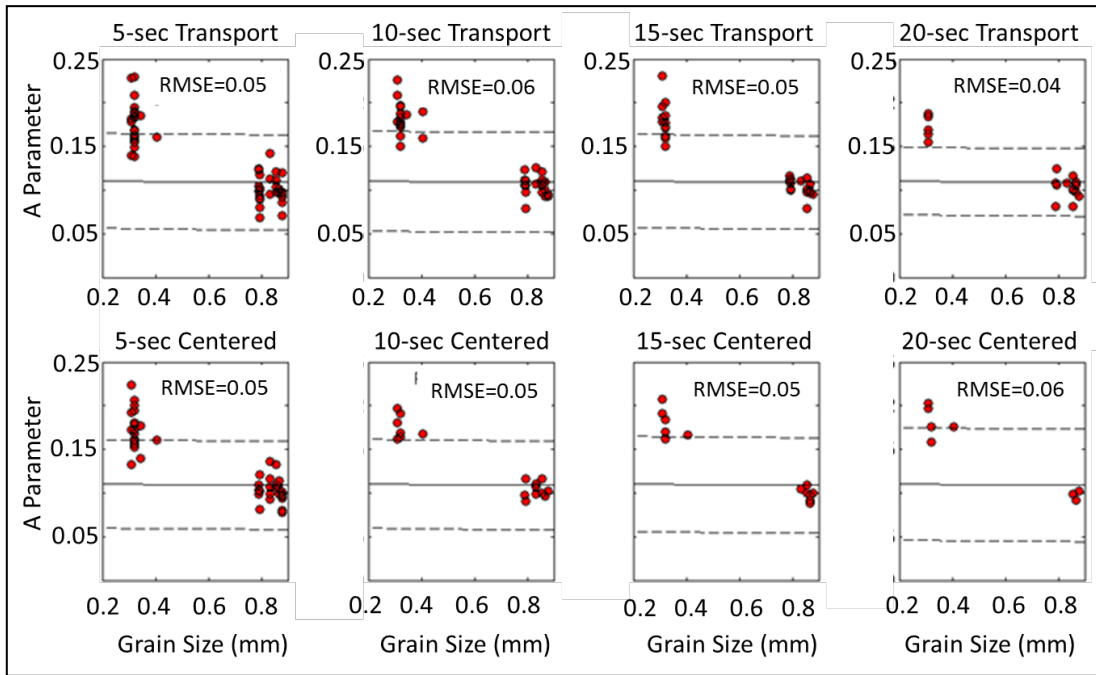
Figure 29: Root mean squared errors calculated between field-derived *A* and Bagnold's *A* parameter. The solid line is Bagnold's *A* parameter. Dashed lines are the prediction error based on the RMSE from field-observed values.

One-sample (where Bagnold's A = 0.1) and two-sample (Bagnold's A(d), Equation 27) t-tests between observed and predicted *A* were calculated separately for finer and coarser samples. One sample t-test showed observed *A* is only statistically different from 0.1 for finer grain samples, $(p < 0.00)$. Two-sample t-tests also only show a statistical difference between

observed and predicted A for finer samples ($p < 0.00$). This indicates Bagnold's A value is not appropriate for finer grain samples.

For the finer grain population, observed A agree closely with those of Lyles and Krauss (1971). They observed threshold shear velocities that were significantly greater than those of Bagnold and others. Lyles and Krauss (1971) tested threshold shear velocity and calculated observed A using Bagnold's fluid threshold from visually observing the initiation of quartz sand particles over a rough surface in a wind tunnel. The surface was composed of 6 mm glued sand to create considerable roughness. Their experiments showed particles ranging from 0.18-0.30 mm had threshold shear velocities at ~0.42 m/s, and an observed $A = 0.18$. In this study, observed A varied about 0.18, ranging from 0.14-0.23 for grain sizes ranging from 0.31-0.40 mm. The grain sizes in this analysis are slightly larger than those tested by Lyles and Kraus and the largest grains on the surface were much smaller than their 6 mm size particles. However, the 0.59-0.84 mm grains tested in Lyles and Kraus also resulted in an observed $A = 0.18$, much greater than the average observed A found here for comparable grain sizes.

Overall, the analysis of Bagnold's A suggests that the observed A is not constant at 0.1, but instead occurs over a range for both finer and coarser particles. Finer sample runs have observed A that are a statistically different from Bagnold's A constant and from Equation 27. This suggests Bagnold's A may not be representative when used as a constant, but rather a probability distribution of possible values of A for particular surfaces may better predict the range of threshold shear velocities.

4.4 Predicted vs. observed u_{*t}

Predicted and observed shear velocities were compared to assess potential errors between Bagnold's fluid threshold and thresholds observed in the field. The 1:1 correspondence

between predicted and field-observed u_{*t} is shown in Figure 30. Threshold shear velocity does not appear to vary with grain size for any threshold condition with averaging periods between 5 and 20 s. 5-minute average shear velocities for the each full sampling period are similar to 5-10 s averaging periods and range from ~0.38-0.41 m/s. 5-minute shear velocity also does not vary with grain size despite the distinct differences in grain size populations. Bagnold's model consistently under predicts the fluid threshold for finer grain samples, typically over predicts the threshold for coarse grain observations. This indicates threshold shear velocity for finer particles is considerably over predicted at averaging periods ranging from 5-300 s. Two-sample t-tests were used to test if the mean values of observed shear velocities are statistically different from Bagnold's model. The t-tests found only finer grain samples are statistically different from observed thresholds ($\rho < 0.05$).
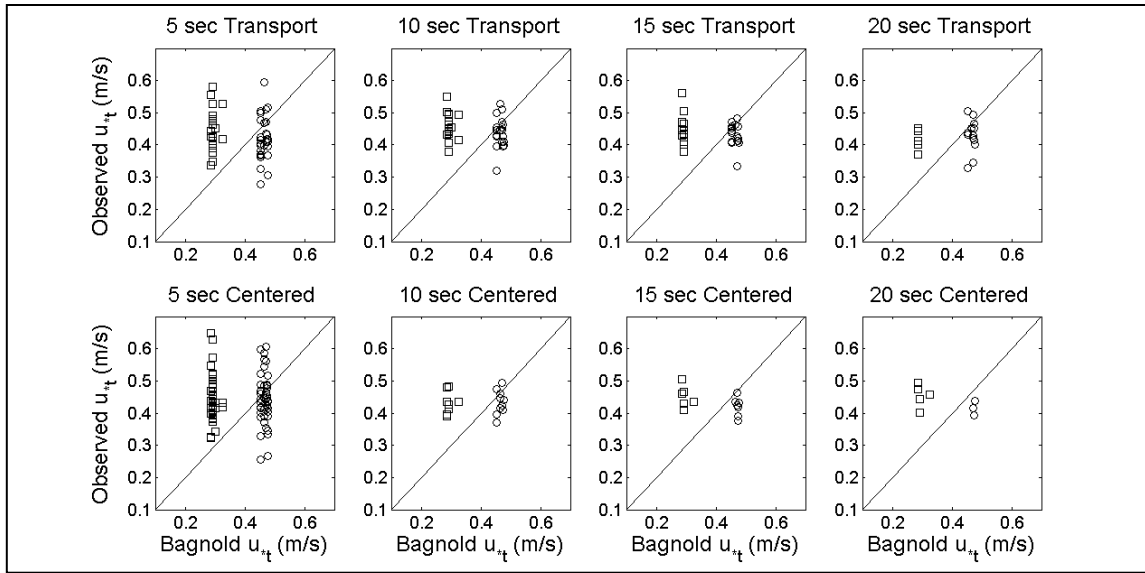
Figure 30: Field-observed versus Bagnold's (1936) predicted threshold shear velocity. The black line is the 1:1 correspondence between observation and prediction, finer grain populations are shown as squares and coarse grain populations are shown by circles.

The difference between Bagnold's model of the fluid threshold and observed u_{*t} is quantified via RMSE (Figure 31). RMSE range from 0.09-0.15 m/s, with the greatest error in u_{*t} occurs for the 20 s averaging period centered on the second of particle initiation (RMSE = 0.15 m/s). RMSE is approximately the same for 5-15 s averaging periods (RMSE = 0.12-0.13 m/s). This suggests prediction errors on the order of 23-35% of the fluid threshold shear velocity are expected in similar conditions to this field site.
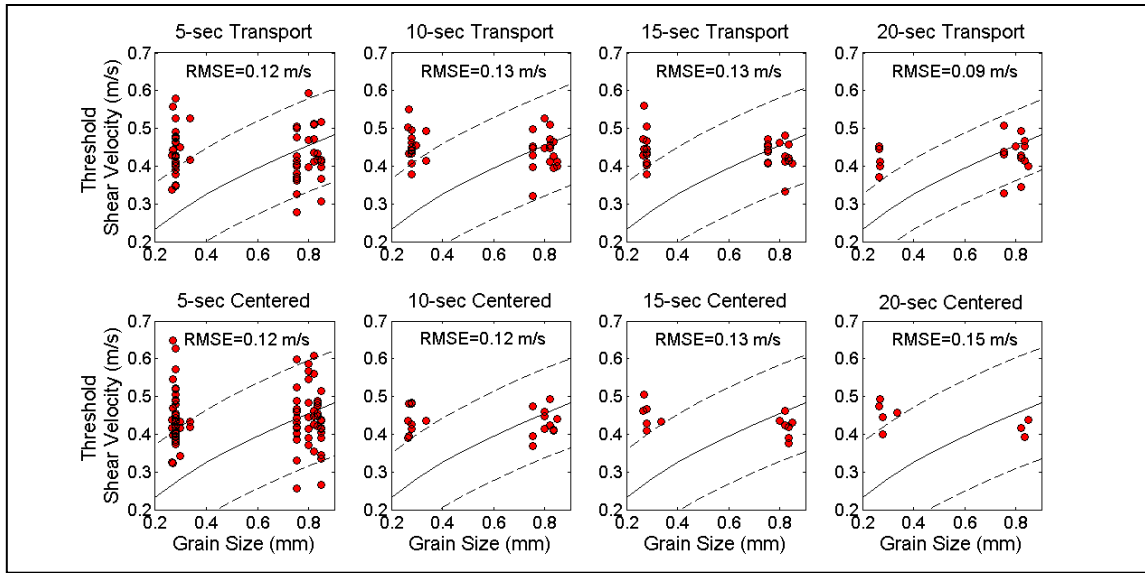
Figure 31: Field-observed u_{*t} versus grain size d for 'transport', and 'centered' conditions calculated over 5, 10, 15, and 20 second averaging periods. The solid black line in each subplot is Bagnold's (1936) fluid threshold and RMSE is the root-mean squared errors of predicted vs. experimental data. Dashed lines are the expected prediction error (+1 Standard Error) derived using the RMSE.

Threshold shear velocity occurs over a range and decreases with increasing averaging period (as does the variance, Table 6). However, this decreasing variability in observed u_{*t} is not attributed to smaller discrepancies in Bagnold's fluid threshold model and field observations. Average threshold shear velocity for 'transport' conditions show a greater range than 'centered'. Longer averaging periods (15-20 s) for finer samples typically have threshold shear velocities greater than 1 standard error, and coarser particles vary closer to Bagnold's predicted value. Bedload initiation occurs below Bagnold's fluid threshold for average threshold shear velocity centered on the second of transport show. Bedload initiation occurs below Bagnold's fluid

threshold for the 15-20 s 'centered' condition in all but one case. Longer averaging periods smooth out higher frequency fluctuations associated with the initiation of motion. The over prediction of the fluid threshold for coarser grains at longer averaging periods suggest high frequency velocity fluctuations are smoothed over by shear velocities lower than Bagnold's predicted threshold.

The over prediction of the fluid threshold for coarser grains at longer averaging periods suggests high frequency velocity fluctuations are smoothed over by shear velocities lower than Bagnold's predicted threshold. This was examined using shear velocities when no transport was occurring for long averaging periods. Figure 32 shows the 30 s averaging period of no transport relative to Bagnold's model. The average shear velocity during 'no transport' conditions was 0.38 m/s. During finer grain runs, Bagnold's model predicts threshold exceedance during periods when no transport was occurring. The same results were found for 'no transport' shear velocities calculated over shorter averaging periods (5, 10, 15 and 20 seconds) (Figure 33). For finer grain samples Bagnold's model predicted transport during conditions when the bed was stationary, i.e. no particles in motion.
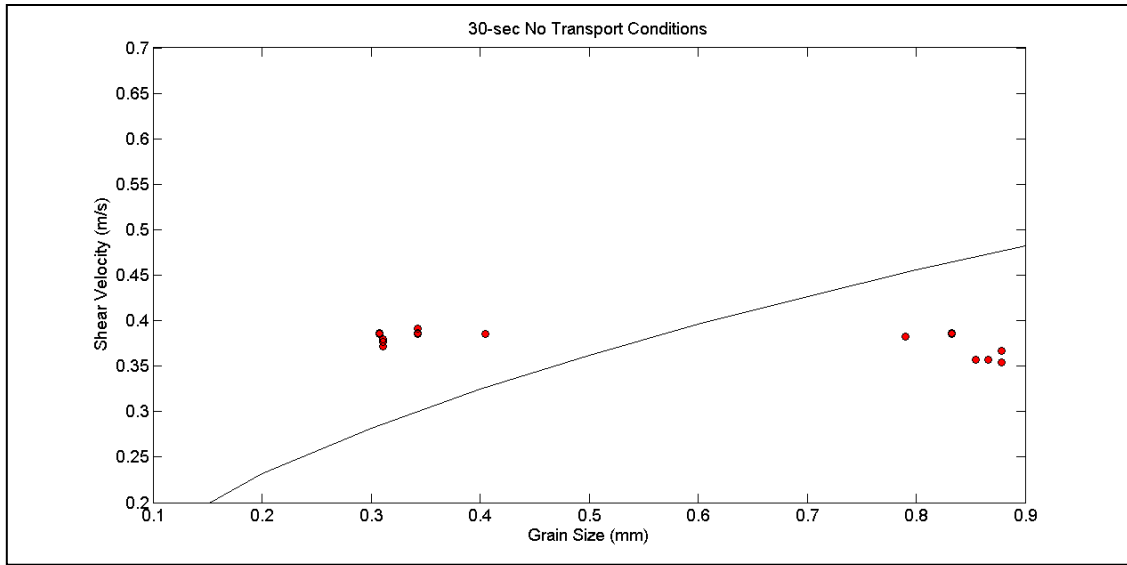
Figure 32: Observed shear velocity from 30 second periods of 'no transport'. The solid line is Bagnold's fluid threshold shear velocity model.
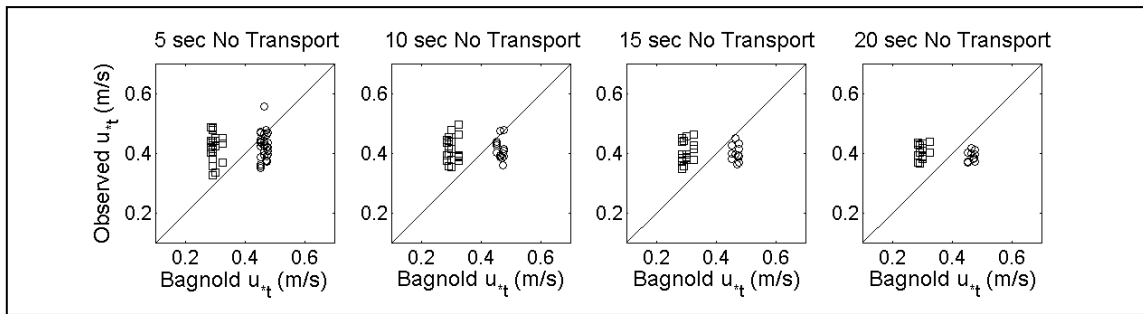
Figure 33: Observed shear velocity for 'no transport' for 5, 10, 15 and 20 second periods. The solid line is the 1:1 correspondence between Bagnold and field-observed threshold shear velocity.

Captured bedload transport consisted of two grain populations and resulted in two distinct predicted threshold shear velocities. Bagnold's model of the fluid threshold, largely a

function of grain size, did not reflect the grain size distinction in the observed values. Observed threshold shear velocity occurred over a range versus a single value as predicted by Bagnold. This is in agreement with previous literature (Shields, 1936; Einstein, 1942; Miller et al., 1977; Williams et al., 1994; Duan et al., 2013). Additionally, shear velocities averaged during periods of no movement should be less than Bagnold's fluid threshold, yet Bagnold's model predicted bedload initiation during no transport conditions at 5-30 s averaged shear velocities.

4.5 Threshold wind speed

The minimum, maximum and average threshold wind speeds for 'no transport', 'centered' and 'transport' conditions are shown in Figure 33. Using the lowest anemometer to the surface, 1 s speeds corresponding to each threshold condition were analyzed. A number of threshold events comprised each threshold condition: 95 'no transport' events , 76 'centered' events, and 74 'transport' events., Similar to the threshold shear velocity results, the threshold wind speed range did not vary with grain size or threshold condition. A wide range of wind speeds corresponded to the initiation of bedload movement, and have appear to have little dependence on finer versus coarser samples. Only 'transport' threshold wind speeds showed any grain size difference when a lower maximum speed for finer grain sample was detected (Figure 34).

Average and minimum threshold speeds for finer and coarser samples are shown in Table 8. Average threshold wind speed for finer grain particles was ~ 5.6 m/s with minimum speeds approximately 4 m/s. This agrees with Schönfeldt (2004) who found the average threshold to occur between 5 and 6 m/s for sand particles of 0.23 mm. Coarser samples had average threshold wind speeds of ~5.5-5.6 m/s with minimum also varying about 4 m/s. Two-

sample t-tests indicated no statistical difference between finer and coarser sample threshold wind speeds.
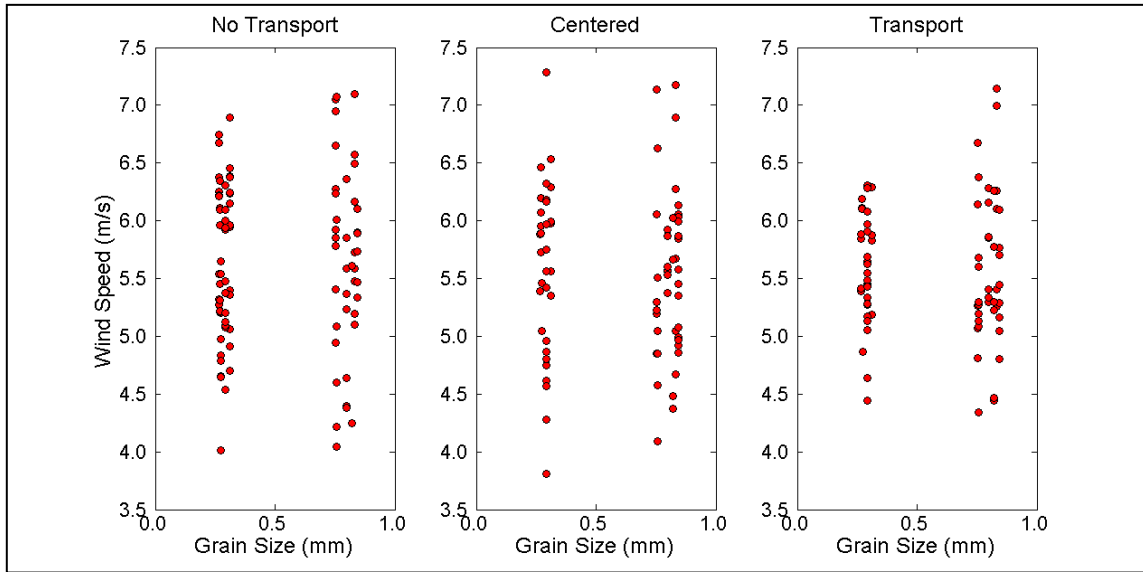
Figure 34: Threshold wind speeds versus average grain size.

Table 8: Average and minimum threshold wind speeds for finer and coarser populations

		Mean Speed (m/s)		Minimum Speed (m/s)	
Profile	n	Finer	Coarser	Finer	Coarser
No Transport	95	5.63	5.65	4.02	4.04
Centered	76	5.61	5.52	3.81	4.09
Transport	74	5.58	5.56	4.45	4.34

The spatial and temporal variability driving intermittency has been attributed to wind unsteadiness or gustiness (Bauer et al., 1998; Schönfeldt, 2004). It was of interest to explore the

relationship between sudden increases in wind speed (gusts) and grain size of particles moved. Figure 35 shows the difference in the 2 and 5 s average speed between 'transport' conditions and the period of no transport just prior to movement. The difference in wind speed ranged from about -0.5 m/s to 0.7 m/s at the 5 s averaging period, and from ~-0.8 to ~1.2 m/s for the 2 s averaging period. The 5 s averages show a considerable reduction in variability but no trend with grain size. Wind speed was shown to decrease from no transport to transport in nearly half the cases. This may be due to high frequency adjustments of wind speed at 100 mm to momentum transferred to the bed. Schönfeldt (2004) found decreases in wind speed averaged at 4 or more seconds driving a hysteresis effect between the wind speed and number of particles moved during intermittency. Similar to threshold shear velocities observed in the field, no apparent relationship with grain size was found.
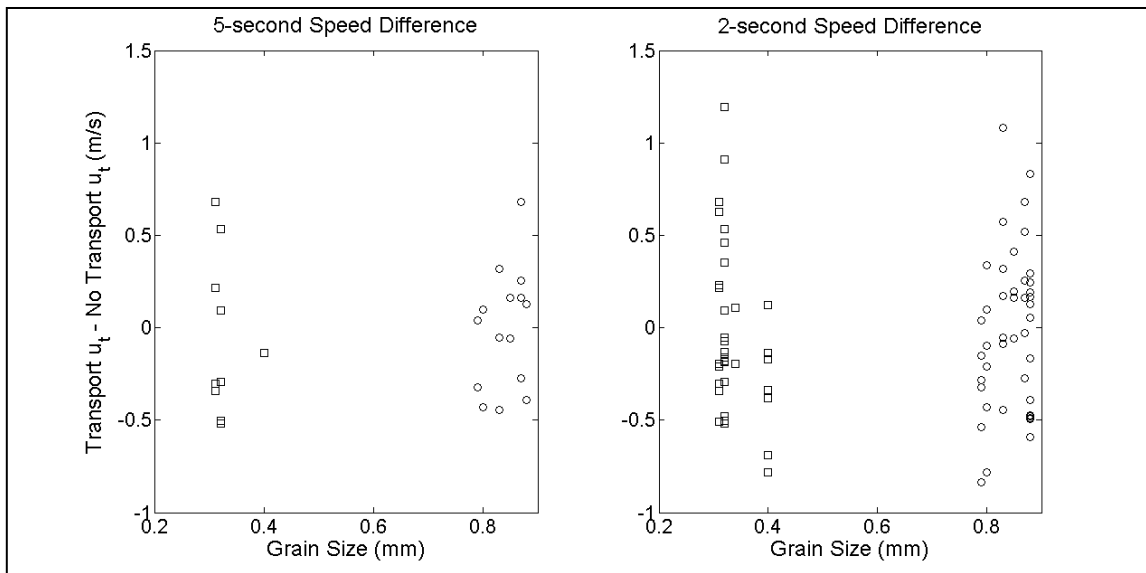
Figure 35: Wind speed difference between 2 and 5 s average between 'transport' conditions and 'no transport' prior to initiation of particles. Squares illustrate the finer grain populations while circles indicate the coarser population.

87

4.6 Multiple linear regression and model comparison

Bagnold's model does not predict threshold shear velocity for all observed grain populations. One reason for the discrepancy between predicted and observed thresholds is Bagnold's use of the average grain size to represent a population. The two sets of populations captured in the bedload trap each have slightly different grain size distributions; well or moderately sorted, mostly symmetrical and mesokurtic to platykurtic. A multiple linear regression analysis was conducted to develop a model predicting the fluid threshold shear velocity using observed thresholds from 'centered' and 'transport' conditions at all averaging periods and basic grain size distribution statistics (mean grain size, sorting, skewness and kurtosis) that may be more representative of the population.

Grain size statistics individually did not explain variability at a statistically significant level. Mean grain size, sorting, skewness, and kurtosis were individually tested to resolve its predictive power in modeling the fluid threshold and no significant correlations ($\rho < 0.05$) were found. A series of multiple regressions using different combinations of mean, sorting, skewness and kurtosis were tested for a statistically significant prediction of threshold shear velocity. Only one of these models were statistically significant at the 95% level. The 15 s 'transport' conditions explained 74% of the variability in fluid threshold shear velocity and was statistically significant ($p = 0.03$). This model predicts the fluid threshold shear velocity using mean grain size, skewness (γ) and kurtosis ($kurt$):

$$u_{*t} = \beta_0 + \beta_1 d + \beta_2 \gamma + \beta_3 kurt \tag{51}$$

where model coefficients are $\beta_0 = 0.8139$, $\beta_1 = 0.3013$, $\beta_2 = -6.2072$, $\& \beta_3 = 256.6955$. Observed threshold shear velocities at the 15 s 'transport' condition are plotted with predicted threshold shear velocity in Figure 36. The black line is the 1:1 correspondence between observed and predicted threshold shear velocity. This model indicates that incorporating more

than mean grain size quantifies statistically significant ($\rho < 0.05$) threshold shear velocity in a naturally mixed field environment.
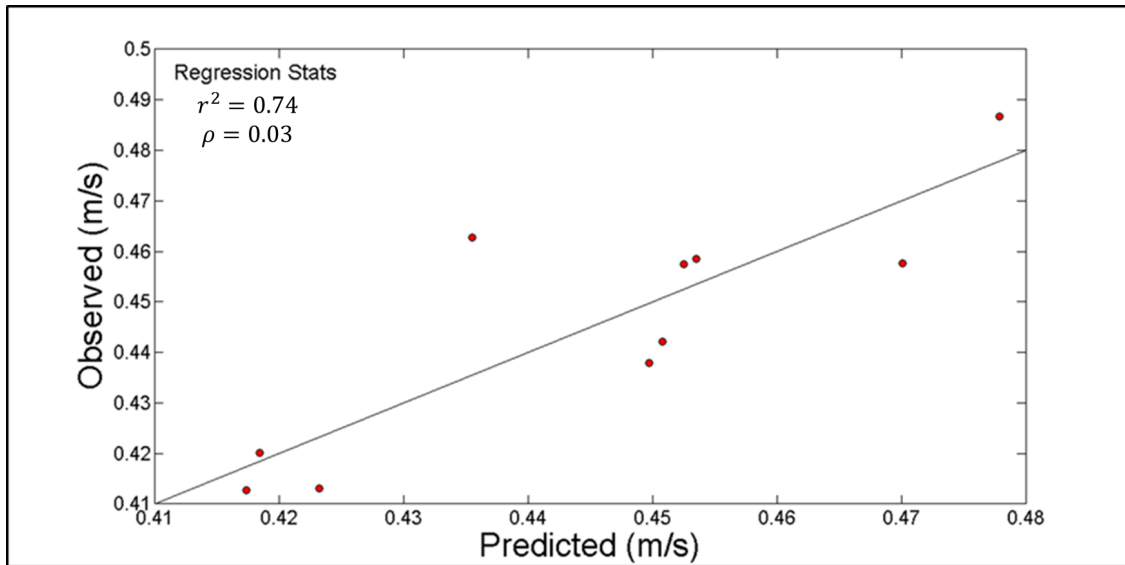
Figure 36: Predicted threshold shear velocity from Equation 51 versus observed thresholds for 15 sec 'transport' conditions.

Careful interpretation must be used as the grain size characteristics modeling the threshold in Equation 51 are from captured bedload particles, not the surface population as a whole. Interpreting the effects of mean size, sorting, skewness and kurtosis on governing particle initiation is difficult. Surfaces with large sorting values indicate highly mixed, poorly sorted grain size populations. Poorly sorted populations tend to shield finer particles from flow and reduce their susceptibility for entrainment. Coarser particles in a bed of finer grains are more susceptible to fluid forces as they have increased cross-sectional areas exposed to flow and

inherently lower (than finer grains) pivoting angles. The coarser and finer grains sizes seen in Figure 12 at the study site suggest the entire surface population has larger sorting values. However, the populations captured are well, to moderately, sorted and are likely a function of ripples organizing particles via mode of transport. This could lead to selective transport of coarser and finer grains particles moving as bedload, resulting in well to moderately sorted populations. Platykurtic (finer grain samples) and mesokurtic (coarser grain samples) distributions as found in the finer grain samples indicate a wider range of grain sizes. More particles of various size suggest particles may be subject to a wider range of threshold shear velocities. However, more data is required to ascertain the influences of sorting and kurtosis on the threshold of motion. Additionally, this model was the only statistically significant model out of the all combinations tested, and more observations with different mean, sorting and kurtosis distributions are required to solidify the influence of sorting and kurtosis on threshold shear velocity. However, Equation 51 is a result of directly measured field data of the fluid threshold.

Bagnold's model was compared to the models of Fletcher (1976), Greeley and Iversen (1985), Nickling (1988), Shao and Lu (2000), and Kok and Renno (2006), in addition to Equation 51 from this study. The RMSE between predicted and observed threshold shear velocity were calculated for model comparison to Bagnold (1936) for the 15 sec 'transport' conditions are shown in Figure 37. The Bagnold-predicted threshold shear velocity using the average grain size of the synthetically mixed surface population is also plotted in Figure 37. The Bagnold-predicted threshold for the entire surface is lower than nearly all observed threshold shear velocities. This suggests the average grain size of a mixed size surface results in an unrepresentative value for the grains in motion and a lower threshold shear velocity than observed for both finer and coarser particles.
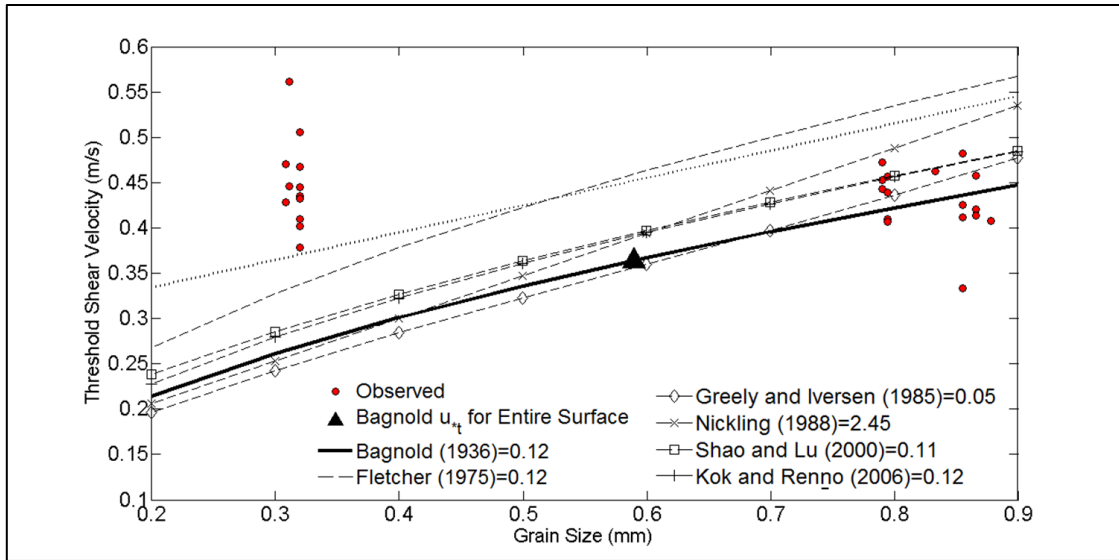
Figure 37: Model comparison with observed threshold shear velocity. RMSE between predictive models and experimental data (15 s 'transport' conditions, circles) is reported for each model.

Certain models have similar errors when compared to observed thresholds. Bagnold (1936), Kok and Renno (2006), Shao and Lu (2000) have RMSE ~0.11 m/s. These models all considerably under-predict the fluid threshold for finer particles. Bagnold (1936) and Shao and Lu (2000) are on the lower end of predicting the threshold for coarser particles, while Kok and Renno (2006) over predict coarser particles. Fletcher (1976) is close to these models with an RMSE of 0.12 m/s. Fletcher's (1976) model over-predicts all coarser grain samples more than all other models, while also predicting more closely thresholds for finer grain samples. Nickling (1988) tends to have the poorest correspondence with observed shear velocities with errors close to an order of magnitude greater than the other models. However, in Nickling's (1988) publication he distinctly states his bimodal surfaces do not fit his model. While no distributions in this field site are bimodal the coarser grain crests and finer grain troughs of ripples suggest

91

potential bimodality of the surface. This may be one reason for the large degree of error in Nickling's model.

Greeley and Iversen (1985) and Equation 51 from this study have the lowest and similar RMSE. Interestingly, these models correspond different to both the finer and coarser threshold samples. Greeley and Iversen (1985) seem to model the coarser samples much more closely than all other models. However, their model also is the worst at modeling the finer grain thresholds. Equation 51 from this study over predicts the threshold for coarser particles thresholds, yet it most closely models the finer sample thresholds.

No models here accurately predict the fluid threshold for both finer and coarser samples. In a naturally graded population of sand grains, coarser particles typically experience greater flow exposure and a higher pivoting angle, e.g. the equal mobility concept (Wilcock, 1993). This makes these particles easier to move than coarser particles. Likewise, finer particles in a mixed population are sheltered by coarser particles and inherently have lower pivoting angles making it more difficult to be initiated by the fluid alone. Wilcock (1993, p. 502) examined different sediment size distributions (skewed, lognormal, unimodal and weakly bimodal) in fluvial flow and found that despite the type of size distribution, all particles began moving at a similar flow strength. Here, finer particles correspond to a greater shear velocity than predicted by most models. This suggests a closer evaluation of the threshold of motion for finer particles in a naturally mixed environment should be conducted.

4.7 Summary

Bagnold's model of the threshold is dependent upon the average grain size and his *A* parameter, both which do not correspond to observed values as predicted by Bagnold's model. The greatest discrepancies between Bagnold's model and observed threshold shear velocity are

for finer grain thresholds, prediction of threshold exceedance during periods no movement, and the range of observed threshold values for any given grain size. Threshold wind speeds nor gusts correspond to grain size. Observed threshold shear velocity for finer grain populations are considerably larger than those predicted not only by Bagnold, but also threshold models of Fletcher (1976), Greeley and Iversen (1985), Nickling (1988), Shao and Lu (2000) and Kok and Renno (2006) (Figure 36). Based on field data presented here, the fluid threshold for a naturally mixed grain population requires greater shear velocities (i.e. greater shear stress) to set the finer particles of a mixed population into motion.

Observed threshold shear velocity did not vary with grain size as proposed by Bagnold (1936), but rather occurred over a range. This can been seen in the considerable scatter for any particular grain size in Figures 29, 30 and 31, supporting the findings from previous work (Shields, 1936; Einstein, 1942; Vanoni, 1964; Grass, 1970; Gessler, 1971; Miller et al., 1977; Williams et al., 1994; Duan et al., 2013). Threshold wind speeds also did not vary with grain size and occurred over a range as shown in Figure 34. The speed up of wind at the threshold (potential gusts) also does not show any dependence on grain size. No correlation was found between threshold wind speed averaged over 1 s and the threshold of motion. This is contradictory to recent studies who have identified the threshold of motion via wind speed versus shear velocity (Stout and Zobeck, 1997; Davidson-Arnott et al., 2005).

The models of Bagnold (1936), Kok and Renno (2006), Shao and Lu (2000) may be more representative for non-mixed, unimodal size populations. Over a mixed size grain population, these models had consistently large RMSE in comparison to other models. Greeley and Iversen (1985) and Equation 51 have a significantly reduced error and better model of threshold shear velocities for naturally mixed size grain populations similar to this study site.

CHAPTER V

DISCUSSION

Fluid threshold shear velocities observed on a surface composed of mixed size grains suggests errors exist in Bagnold's model and highlight discrepancies in predicting particle entrainment even under relatively simple field conditions. Three critical factors were found here to influence the fluid threshold in an environment of mixed-size sands: (1) increased flow resistance for finer grains in mixed size surface populations, (2) the presence of small scale ripples, and (3) the stochastic nature of resisting and fluid forces acting on individual particles.

The surface material was composed of a mixed size grain population. This is evidenced by the two different grain size distributions captured in the bedload trap (Figure 20), the polymodal characteristic of the synthetically mixed surface population (Figure 21), and Figure 12 where coarser and finer particles are shown to be laterally segregated. For this surface population, there is no clear relationship between threshold shear velocity and average grain size of particles initiated (Figures 29-31). This is contradictory to the relationship found in unimodal surface populations where threshold shear velocity varies as the square root of the average grain diameter (Bagnold, 1936; Shields, 1936). Instead, observed threshold shear velocity occurs over a range that varies around 0.41-0.43 m/s for both finer and coarser samples, consistently under predicting the threshold for finer grains (~0.27 m/s) and very close to the predicted threshold of coarser grains (~0.43 m/s). A limited number of studies on the threshold for mixed-size populations in aeolian environments has been conducted (Nickling, 1988). Yet, a number of fluvial studies concerning the threshold of motion in mixed size grain populations have found similar results (Parker and Klingeman, 1982; Parker et al., 1982; Wiberg and Smith, 1987;

Wilcock, 1988; Wilcock and Southard, 1988; Wilcock, 1993), and from those results developed the concept of equal mobility. Equal mobility, as noted above, describes the single threshold required to initiate movement on a surface of mixed size grains that does not increase with average grain size, but rather is function of the largest grain size in the mixed population (Wiberg and Smith, 1987; Wilcock, 1988; Wilcock and Southard, 1988; Wilcock, 1993). Entrainment of finer (coarser) particles in mixed grain populations correspond to a larger (smaller) critical shear stress than those found for the same grain size in a unimodal distribution (Lyles and Krauss, 1971; Parker and Klingeman, 1982; Wiberg and Smith, 1987; Wilcock, 1988; Wilcock and Southard, 1988; Wilcock, 1993). In a mixed size population there is a greater range of pivoting angles and exposure to flow that results in increases (decreases) in the threshold shear velocity for finer (coarser) particles (Wiberg and Smith, 1987; Wilcock, 1988; Wilcock, 1993). Equal mobility is based on the premise that critical shear stress increases (decreases) for finer (coarser) particles in a mixed population due to reduced (greater) exposure to flow and increases (reduced) resistance to fluid forces via lower (greater) pivoting angles (Wilcock, 1988). The single threshold for these populations are greater than the threshold for finer particles and slightly lower than the threshold for coarsest particles. Observed threshold shear velocity for coarser grain found in this study are frequently lower than Bagnold's predicted model during 'centered' conditions (Figures 29-31) and are typically lower than the models of Fletcher (1975), Nickling (1988) and Shao and Lu (2000) (Figure 36). Finer and coarser particle are initiated at approximately the same average threshold shear velocity (Table 6), in agreement with the fluvial concept of equal mobility.

The presence of coarse grain ripple crests with finer grain troughs also contribute to the discrepancies between predicted and observed thresholds. The development of coarse grain ripples moving over finer grains has also been observed on a beach and been attributed to

95

aeolian-driven decoupling of a unimodal sand source (Bauer, 1991). The deflation of a unimodal

grain population results in a coarser surface lag deposit. Bauer (1991, 299) explains that finer

particles have a higher shear velocity due to the presence of coarser grains, quoting Bagnold

(1938, p. 208) where he states, *'the presence of larger grains, even in very small proportions,*

appreciably raises the threshold shear velocity'. These coarser particles organize into ripples

and slowly move over the more stationary finer grains. Size segregations from Bauer (1991)

found the coarser ripples to be well-sorted while the finer grain interripple grains to be

moderately sorted. The grain size distribution sorting captured in the bedload trap are identical

to Bauer's surface conditions (Figures 12 and 20, Table 4) as well as the increased threshold

shear velocity for finer grain samples (Figures 29-31). Visually observing the movement of

coarser particles, Bauer (1991, p. 299) notices bedload movement:

> *"...the process of ripple migration involved individual grains being displaced*
>
> *from one ripple crest during high velocity gusts, and then rolling quickly across*
>
> *the interripple surface until they lodged against the downwind ripple. This*
>
> *indicates that coarse-particle transport was not driven substantially by saltation*
>
> *impacts as observed by others, but rather wind stress."*

Bauer (1991) has nearly identical surface conditions as found in this study and observes the fluid

threshold. The visual and quantitative observation of bedload transport during field conditions in

an aeolian environment as seen in Bauer (1991) and this study suggests that the fluid threshold

for surface populations of mixed sizes correspond to that of the largest grains. This corroborates

the fluvial concept of equal mobility, but based on the premise of lateral segregation. Equal

mobility hypothesis states the increased (decreased) exposure to flow and decreased (increased)

pivoting angles for finer (coarser) particles generate a single threshold value for the surface corresponding to the threshold required to initiate largest grain. However, this can only partially be the case for the surface conditions found here. The mixed size population was not evenly distributed over the surface, but rather laterally organized with coarse grain ripples and finer grain troughs. Bedload movement on the windward face of coarse grain ripples presents coarse particles with a greater pivoting angle. This increase in pivoting angle requires a greater shear velocity to initiate movement for coarser particles, partially opposing the premise behind equal mobility in the fluvial literature. However, this greater pivoting angle may be more easily overcome by the considerably greater exposure to flow on the upwind face of ripples. More data is needed to describe the small scale physics of the initiation of motion in mixed populations with lateral segregation of particle size.

The greater shear velocity required for the initiation of finer particles in mixed size populations by the fluid alone is supported by the findings in both the fluvial literature via the equal mobility concept and visual field observations from Bagnold (1938) and Bauer (1991). Here, the average threshold shear velocity corresponds to the average grain size of coarse particles. The greater shear stress required for the initiation of finer grain particles explains Bagnold's prediction error for transport (or threshold exceedance) during periods of no movement (Figures 32-33). This also explains the poor correspondence between grain size and threshold wind speed and/or gusts (Figures 34-35). Average wind speeds at 100 mm in this study are approximately 5.5 m/s. The single threshold corresponding to the coarsest particle for these surface conditions explains the poor performance of Bagnold (1936), Greeley and Iversen (1985), Nickling (1988), Shao and Lu (2000) and Kok and Renno (2006) at predicting threshold exceedance for finer particles. However, this also suggests the model developed in this study (Equation 51) that uses average grain size, sorting and kurtosis to predict the fluid threshold is

only applicable in similar surface conditions. The grain size distributions here are a function of the populations transported, not of the entire surface population. This suggests Equation 51 is rather limited and more research is needed to verify its applicability in other field locations.

Generalizations required by transport models to represent fluid-grain interactions of an entire surface population, despite the surface configuration, with a single threshold. This research suggests attention should be paid to the surface configuration. At a grain scale, the entrainment of particles is a function particle size, shape, pivoting angles, exposure to flow, interparticle forces, drag and lift (Shields, 1936; Middleton and Southard, 1978; Willetts, 1983; Greeley and Iversen, 1985; Cornelis and Gabriels, 2004; Kok et al., 2012). These parameters change with different environmental conditions, grain size distributions, and the presence of ripples. These parameters are difficult to measure at the grain scale, but the various arrangement of these parameters on any particular surface can result in a range of threshold shear velocities (Einstein 1942; Grass, 1970; Miller et al., 1977). Additionally, in natural environments instantaneous shearing forces intermittently exceed the threshold of motion and cause non-uniform bursts of movement that vary in duration and magnitude (Lyles and Krauss, 1971; Lyles et al., 1971; Williams et al., 1990, 1994; Ellis et al., 2012). Further complexity arises as ripples develop on the surface, increasing the spatial variability of shear stress. The spatial variability of the resisting forces holding individual grains in place and the fluid forces acting on any individual particle, make it difficult to measure the threshold at a grain-to-grain scale. For this reason, threshold shear velocities occur over a range, and from this study, correspond closely to the threshold shear velocity of the largest particles. Yet, transport models require a single value to represent the entire surface. Stochastic transport models incorporating a range of shear velocities (versus a single value) to predict the wind-blown sand transport rates for the coarsest

particles may provide a series of transport rates more representative of observed rates found near the threshold of motion.

Before this work, bedload transport was not separated from saltation and most tests of the fluid threshold defined movement by the initiation of saltation. Thresholds are also defined by the number of grains moved over a surface area (Neil and Yalin, 1969), yet it is still debated what constitutes an appropriate number of entrained grains to exceed the threshold (1, 10, or 100) (Lavelle and Mofjeld, 1987). This is it difficult to assess as the sensitivity, sampling area, and height of saltation sensors can produce radically different results. Here, the fluid threshold was defined by the shear velocity corresponding to the initiation of at least 1 bedload particle following a period of no transport. The number of particles moved in the initial second of fluid threshold exceedance was 1-34 with most initiation seconds having 1-10 particles in motion.

Careful attention should be paid to the surface particle distribution and surface configuration when using Bagnold's model of the fluid threshold. In environments with size segregation, the coarsest fraction of the sand may be more representative of threshold shear velocity for the entire surface. Threshold shear velocity should be tested in a number of different natural field configurations, such as those with: (1) ripples of varying heights, wavelengths, and grain size segregations; and, (2) varying grain size population distributions, e.g., bimodal or polymodal. The threshold shear velocity corresponding to the coarsest particles of a surface as opposed to the average grain size results in a higher threshold shear velocity. Greater threshold shear velocities result in lower predicted transport rates and could account for the current over prediction in transport models at low transport rates (Sherman et al., 1998; Dong et. al., 2003; Sherman et al., 2011; Ellis and Sherman, 2013).

Better prediction of the fluid threshold shear velocity has far reaching implications. The ratio of the fluid to dynamic threshold is a fundamental relationship necessary to model the

transition from intermittent bursts of movement at low transport rates to sustained movement. Reducing or uncovering errors in the fluid threshold provides a method to estimate or reduce errors in the dynamic threshold. This increases our ability to model transport at larger scales. Increasing the accuracy of transport models affords better prediction of dune migration and/or susceptibility, erosion on agricultural fields, and coastal dune recovery and development. The frequency and magnitude the threshold of motion is exceeded determines the frequency and intensity of dust emissions (Tegen et al., 2004; Kurosaki and Mikami, 2007), providing a measure for forecasting global energy budgets and reductions in air quality. Earth-based models provide the basis for developing threshold models to help predict transport rates on other planetary bodies. One example of this is the work that has been conducted on Mars since the 1970's where Bagnold's threshold model has served as the basis for model development (Iversen et al., 1976; Iversen and White, 1982; Greeley and Iversen, 1985). Resolving greater accuracy with Earth-based models improves the foundation for these studies to base their model derivations.

CHAPTER VI

CONCLUSION

Bagnold's (1936) model of the fluid threshold was compared to observed values collected over a flat, dry surface to test for prediction errors in a natural, noncomplex environment on October 22nd, 2011in Jericoacoara, Brazil. This study tested for errors in Bagnold's (1936) fluid threshold shear velocity model in a field environment of a naturally mixed grain size population. A field campaign designed specifically to elucidate errors in Bagnold's model was conducted which included the development of a bedload-specific trap used to correlate measurement of near surface flow conditions to the fluid threshold. The results of this study suggest that Bagnold's (1936) model is not a strong predictor of the fluid threshold shear velocity for mixed size populations, particularly for finer grains. This is due to the use of the average grain size to predict particle movement. Here, the fluid threshold did not vary with grain size but rather was a function of the average threshold shear velocity corresponding to the coarser particles. Two main conclusions are established from this work:

1. Bagnold's model is not adequate for surfaces of naturally mixed sand sizes, and;

2. For naturally mixed sand, the fluid threshold for all particle sizes corresponds to the threshold shear velocity of the largest particles.

Establishing suitable values for the threshold shear velocity is required to accurately model the point at which the wind becomes geomorphically effective in open-air sandy environments. Lateral segregation of a mixed size surfaces is a common feature of aeolian systems (Bauer, 1991) and may increase the threshold shear velocity for finer grains. The current over prediction of transport rates may be a function of using the average grain size for the threshold versus the

larger threshold shear velocity corresponding to the largest particles. Greater thresholds result in

lower predicted transport rates and have the potential to reduce error in transport models.

REFERENCES

Allchin, D. (2001). Error Types. *Perspectives in Science*, 9, 38-59.

Andersson, R.S. (1987). Eolian sediment transport as a stochastic process: the effects of a fluctuating wind on particle trajectories. *The Journal of Geology,* 95, 497-512.

Anderson, R.S., Sørensen, M. & Willetts, B.B. (1991). A review of recent progress in our understanding of aeolian sediment transport. *Acta Mechanica Supplement, 1,* 1-19.

Andreae, M.O. (1996). Raising dust in the greenhouse. *Nature,* 380, 389-390.

Bagnold, R. A. (1936). The movement of desert sand. *Proceedings of the Royal Society of London A, Mathematical and Physical Sciences*, 157, 594–620.

Bagnold, R. A. (1937a). The Transport of Sand by Wind. *The Geographical Journal*, 89(5), 409-438.

Bagnold, R. A. (1937b). The Size-Grading of Sand by Wind. *Proceedings of the Royal Society A: Mathematical, Physical and Engineering Sciences*, 163(913), 250–264. doi:10.1098/rspa.1937.0225

Bagnold, R.A. (1938). The measurement of sand storms. *Proceedings of the Royal Society of London, Series A,* 167, 282-301.

Bagnold, R. A. (1955). The Physics of Blown Sand and Desert Dunes (reprint). Dover Pulications, Inc: Mineola, New York, p. 265.

Barchyn, T.E., & Hugenholtz, C.H. (2010). Field comparison of four piezoelectric sensors for detecting aeolian sediment transport. *Geomorphology,* 120(3), 368-371.

Barrineau, C.P. & Ellis, J.T. (2013). Sediment transport and wind flow around hummocks. *Aeolian Research* 8*,* 19-28.

Bauer, B.O. (1991). Aeolian decoupling of beach sediments. *Annals of the American Association of Geographers,* 81(2), 290-303.

Bauer, B. O., Sherman, D. J., & Wolcott, J. F. (1992). Sources of uncertainty in shear stress and roughness length estimates derived from velocity profiles. *The Progressional Geographer*, 44(4), 453–464.

Bauer, B.O., Davidson-Arnott, R.G.D., Nordstrom, K.F., Ollerhead, J., & Jackson, N.L. (1996). Indeterminancy in aeolian sediment transport across beaches. *Journal of Coastal Research*, 12(3), 641-653.

Bauer, B.O., Yi, J., Namikas, S.L., & Sherman, D.J. (1998). Event detection and conditional averaging in unsteady aeolian systems. *Journal of Arid Environments* 39(3): 345–375.

Bauer, B. O., Davidson-Arnott, R. G. D., Hesp, P. A., Namikas, S. L., Ollerhead, J., & Walker, I. A. (2009). Aeolian sediment transport on a beach: surface moisture, wind fetch, and mean transport. *Geomorphology*, 105(1), 106–116.

Belly, P. (1964). Sand Movement by Wind. U.S. Army Corps Eng. CERC. Technical Memorandum 1(1964), p. 38. Washington, D.C.

Blott, S.J. & Pye, K. (2001). GRADISTAT: A grain size distribution and statistics package for the analysis of unconsolidated sediments. *Earth Surface Processes and Landforms,* 26, 1237-1248.

Buffington, J.M. & Montgomery, D.R. (1997). A systematic analysis of eight decades of incipient motion studies, with special reference to grave-bedded rivers. *Water Resources Research,* 33(8), 1993-2029.

Butterfield, G. R. (1991). Grain transport rates in steady and unsteady turbulent airflows. In *Aeolian Grain Transport I: Mechanics*, eds. Barndorff-Nieldsen and B. B. Willetts. Wien: Springer-Verlag, p. 97–122.

Butterfield, G.R. (1993). Sand transport response to fluctuating wind velocity. In: Clifford, N.J.,

   French, J.R., & Hardisty, J. (Eds.) Turbulence: Perspectives on Flow and Sediment

   Transport. John Wiley & Sons.

Casey, J.G. (1935). Uver Geschiebebeegung (Concerning Geschiebe Movement). *Mitteilungen

   der Preussiischen Versuchsanstalt für Wasserbau and Schiffbau, 19, 86.*

Chepil, W. S. (1945a). Dynamics of Wind Erosion: I. Nature of Movement of Soil by Wind. *Soil

   Science*, 60(4), 305–320.

Chepil, W. S. (1945b). Dynamics of Wind Erosion: II. Initiation of Soil Movement. *Soil Science*,

   60(5), 397–411.

Chepil, W.S. (1961). The use of spheres to measure lift and drag on wind-eroded soil grains. *Soil

   Science of America Journal,* 25(5), 343-345.

Coleman, N.L. (1979). Bed particle Reynolds modelling for fluid frag. *Journal of Hydraulic

   Research,* 17(2), 91-105.

Cornelis, W.M. & Gabriels, D. (2004). A simple model for the prediction of the deflation

   threshold shear velocity of dry loose particles. *Sedimentology,* 51, 39-51.

Davidson-Arnott, R. G. D., MacQuarrie, K., & Aagaard, T. (2005). The effect of wind gusts,

   moisture content and fetch length on sand transport on a beach. *Geomorphology*, 68(1-2),

   115–129. doi:10.1016/j.geomorph.2004.04.008

Davidson-Arnott, R. G. D., & Bauer, B.O. (2009). Aeolian sediment transport on a beach:

   Thresholds, intermittency, and high frequency variability. *Geomorphology, 105,* 117-126.

Dong, Z., Liu, X., Wang, H., & Wang, X. (2003). Aeolian sand transport: a wind tunnel model.

   Sedimentary Geology, 161(1), 71-83.

Draxler, R.R. Gillette, D.A., Kirkpatrick, J.S. & Heller, J. (2001). Estimating PM10 air

> concentrations from dust storms in Iraq, Kuwait and Saudi Arabia. *Atmospheric*
>
> *Environment,* 35(25), 4315-4330.

Duan, S., Cheng, N. & Xie, L. (2013). A new statistical model for threshold friction velocity of

> sand particle motion. *Catena,* 104, 32-38.

Einstein, H. A. (1942). Formulas for the transportation of bed load. *Transactions of the American*

> *Society of Civil Engineers,* 107(1), 561-577.

Einstein, H. A., & El-Samni, E.A. (1949). Hydrodynamic forces on a rough wall. *Reviews of*

> *Modern Physics,* 21(3): *520.*

Ellis, J.T., Morrison, R.F., & Priest, B.H. (2009). Detecting impacts of sand grains with a

> microphone system in field conditions. *Geomorphology,* 105(1), 87-94.

Ellis, J. T., Shermran, D. J., Farrell, E. J., & Li, B. (2012). Temporal and spatial variability of

> aeolian sand transport: Implications for field measurements. *Aeolian Research,* 3, 379-387.

Ellis, J. T., & Sherman, D. J. (2013). Wind-blown sand. In Douglas J. Sherman & A. C. W. Baas

> (Eds.), *Treatise on Geomorphology: Aeolian Geomorphology* (pp. 85–108). San Diego.

Fletcher, B. (1976). The incipient motion of granular materials. *Journal of Physics D: Applied*

> *Physics* 9, 2471-2478.

Fryberger, S.G., & Dean, G. (1979). Dune forms and wind regimes. In:McKee, E.D. (Ed.), *A*

> *Study of Global Sand Seas*, 137-169. *United States Geological Survey, Professional Paper*
>
> 1052.

Gessler, J. (1971). Beginning and ceasing of sediment motion. In: H.W. Shen (Ed.) *River*

> *Mechanics: Fort Collins, Colo.,* H.W. Shen p. 1-22.

Gilbert, G.K. (1914). The Transportation of Debris by Running Water. G.K. Gilbert. & E.C.

> Murphy (Eds.), *United States Geological Survey, Professional Paper* 86, pp. 263.

Gillette, D.A. (1988). Threshold friction velocities for dust production for agricultural soils. *Journal of Geophysical Research: Atmospheres,* 93(D11), 12645-12662.

Gillette, D.A., & Passi, R. (1988). Modeling dust emission caused by wind erosion. *Journal of Geophyiscal Research: Atmospheres,* 93(D11), 14233-14242.

Gillette, D.A., Blifford, I.H. & Fryrear, D.W. (1974). The influence of wind velocity on the size distributions of aerosols generated by the wind erosion of soils. *Journal of Geophyiscal Research,* 79, 4068-4075.

Grass, A.J. (1970). Initial instability of fine bed sands. *Journal of Hydraulic Division, ASCE,* 96, 619-632.

Greeley, R., & Iversen, J.D. (1985). Wind as a Geological Process on Earth, Mars, Venus and Titan. Cambridge University Press: New York.

Hamaker, H.C. (1937). The London-van der Waals attraction between spherical particles. *Physica,* 4(10), 1058-1072.

Iversen, J. D. & White, B. R. (1982). Saltation threshold on Earth, Mars and Venus. *Sedimentology*, *29*(1), 111–119.

Iversen, J. D., Pollack, J., Greeley, R. & White, B.R. (1976). Saltation threshold on Mars: the effect of interparticle forces, surface roughness, and low atmospheric density, *Icarus,* 29(3), 381-393.

Jeffreys, H., (1929). On the transport of sediments by streams. *Proceedings of the Cambridge Philosophical Society,* 25(3), 272-276.

Jiang, Z. & Haff, P.K. (1993). Multiparticle simulation methods applied to the micromechanics of bed load transport. *Water Resources Research,* 29, 399-412.

Jimenez, J.A., Maia, L.P., Serra, J. & Morais, J. (1999). Aeolian dune migration along the Cearácoasta, north-eastern Brazil. *Sedimentology,* 46, 689-701.

Kadib, A. A. (1965). *A function for sand movement by wind*. Berkeley.

Kaimal, J.C. & Finnigan, J.J. (1994). Atmospheric boundary layer flows: their structure and measurement. Oxford University Press, New York.

Kawamura, R. (1951). Study of sand movement by wind. *Translated (1965) as University of California Hydraulics Engineering Laboratory Report HEL 2-8*, Berkeley.

Kok, J.F., & Renno, N.O. (2006). Enhancement of the emission of mineral dust aerosols by electric forces. *Geophysical Research Letters,* 33(19), L19S10.

Kok, J.F., & Renno, N.O. (2008). Electrostatics in wind-blown sand. *Physical Review Letters,* 100, 014501.

Kok, J.F. (2010). Difference in the wind speed required for initiation versus continuation of sand transport on Mars: Implications for dunesa nd dust storms. *Physical Review Letters,* 404(7), 074502.

Kok, J.F., Parteli, E.J., Michaels, T.I. & Karam, D.B. (2012). The physics of wind-blown sand and dust. *Progress in Physics,* 75(10), 106901.

Kurosaki, Y. & Mikami, M. (2007). Threshold wind speed for dust emission in east Asia and its seasonal variations. *Journal of Geophysical Research,* 112, D17202.

Kramer, H. (1935). Sand mixtures and sand movement in a fluvial model. *Transactions of the American Society of Civil Engineers,* 100(1), 798-838.

Lämmel, M., Rings, D. & Kroy, K. (2012). A two-species continuum model for aeolian sand transport. *New Journal of Physics,* 14(9), 093037.

Langbein, D. (1970). Reduced dispersion of energy beteen macroscopic bodies. *Physical Review B,* 2(8), 3371.

Lavelle, J. W., & Mofjeld, H. O. (1987). Do critical stresses for incipient motion and erosion really exist? *Journal of Hydraulic Engineering*, 113(3), 370–385.

Leatherman, S.P. (1978). A new aeolian sand trap design. *Sedimentology,* 25(2), 303-306.

Lettau, H. (1969). Note on aerodynamic roughness-parameter estimation on the basis of roughness-element description. *Journal of Applied Meteorology*, 6, 828–832.

Lettau, K., & Lettau, H. (1977). *Experimental and micrometeorological field studies of dune migration. Exploring the World's Driest Climate* (pp. 110–147).

Li, B., Sherman, D. J., Farrell, E. J., & Ellis, J. T. (2010). Variability of the apparent von Kármán parameter during aeolian saltation. *Geophysical Research Letters*, 37(15), n/a–n/a. doi:10.1029/2010GL044068

Lorenz, R.D., Wall, S., Radebaugh, J., Boubin, G., Reffet, E., Janssen, M., Stofan, E., Lopes, R., Kirk, R., Elachi, C., Lunine, J., Mithcell, K., Paganelli, F., Soderblom, L., Wood C., Wye, L., Zebker, H., Anderson, Y., Ostro, S., Allison, M., Boehmer, R., Callahn, P., Encrenaz, P, Ori, G.G., Francescetti, G., Gim, Y., Hamilton, G., Hensley, S., Johnson, W., Kelleher, K., Muhleman, D., Picardi, G., Posa, F., Roth, L., Seu, R. Shaffer, S., Stiles, B., Vetrealla, S., Flamini, E. & West, R. (2006). The sand seas of Titan: Cassini RADAR observations of longitudinal dunes. *Science,* 312(5774), 724-727.

Lyles, L., & Krauss, R. K. (1971). Threshold Velocities and Initial Particle Motion as Influenced by Air Turbulence. *Transactions of the American Society of Agricultural Engineers*, 14(3), 563–566.

Lyles, L., Disrud, L.A., & Krauss, R. K. (1971). Turbulence Intensity as Influenced by Surface Roughness and Mean Velocity in a Wind-Tunnel Boundary Layer. *Transactions of the American Society of Agricultural Engineers*, 14, 285–289.

Marticorena, B., Bergametti, G., Gillette, D. & Belnap, J. (1997). Factors controlling threshold friction velocity in semiarid and arid areas of the United States. *Journal of Geophysical Research,* 102(D19), 23277-23287.

Massey, J.C. (2013). A wind tunnel investigation to examine the role of air humidity in
controlling the threshold shear velocity of a surface and in controling the mass flux of
material from a surface. Dissertation, Texas Tech University, 59 p.

McKenna-Neuman, C. & Nickling, W.G. (1989). A theoretical and wind tunnel investigation of
the effect of capillary water on the entrainment of sediment by wind. *Canadian Journal of
Soil Science,* 69(1), 79-96.

Middleton, G. V., & Southard, J. B. (1978). *Mechanics of Sediment Movement*. Binghamton,
NY.

Miller, M.C., McCave, I.N. & Komar, P.D. (1977). Threshold of sediment motion under
unidirectional currents. *Sedimentology,* 24, 507-527.

Mitha, S., Tran, M.Q., Werner, B.T. & Haff, P.K. (1986). The grain-bed impact process in eolian
saltation. *Acta Mechanica,* 63, 267-278.

Namikas, S.L., Bauer, B.O., & Sherman, D.J., (2003). Influence of averaging interval on shear
velocity estimates for aeolian transport modeling. *Geomorphology*, 53, 235-346.

Geomorphology, 114(3), 303-310.

Nickling, W.G., (1988). The initiation of particle movement by wind. *Sedimentology,* 35, 499-
511.

Neil, C.R. (1967). Mean-velocity criterion for scour of coarse uniform bed-material. *Proceedings
of the 12th Congress of the International Association of Hydraulics Research,* 3, 46-54.

Neil, C.R. & Yalin, M.S. (1969). Quantitative definition of beginning of bed movement. *Journal
of Hydraulic Division, ASCE, 95(HYI),* 585-587.

Owen, P. R. (1964). Saltation of uniform grains in air. *Journal of Fluid Mechanics*, *20*, 225–242.

Owens, J.S. (1908). Experients on the transporting power of sea currents. *The Geographical
Journal,* 31(4), 415-420.

Ozer, P., Laghdaf, M.B.O.M., Lemine, S.O.M. & Gassani, J. (2006). Estimation of air quality
degradation due to Sahran dust at Nouakchott, Mauritania, from horizontal visibility data.
Water, Air, and Soil Pollution, 178, 79-87.

Paintal, A.S. (1971). A stochastic model of bed load transport. *Journal of Hydraulic Research,*
9(4), 527-554.

Parker, G. & Klingeman, P.C (1982). On why gravel bed streams are paved. *Water Resources
Research,* 18(5), 1409-1423.

Parker, G. Klingeman, P.C. & McLean, D.L. (1982). Bedload and size distribution in paved
gravel-bed streams. *Journal of Hydraulics Division,* 108(4), 544-571.

Prandtl, L., (1925). Report on the investigation of developed turbulence. National Advisory
Committee for Aeronautics Technical Memorandum 1231 (1949), Translation of "Bericht
uber Untersuchungen zur ausgebildeten Turbulenz." Zeitschrift fur angewandte
Mathematik und Mechanik, 5(2).

Rasmussen, K.R. & Sørensen, M. (1999). Aeolian mass transport near the saltation threshold.
Earth Surface Processes and Landforms, 24, 413-422.

Reynolds, O. (1883). An experimental investigation of the circumstances which determine
whether the motion of water shall be direct or sinuous, and of the law of resistance in
parallel channels. *Philosophical Transactions of the Royal Society* 174, 935-982.

Sarre, R.D. (1988). Evaluation of aeolian sand transport equations using intertidal zone
measurements, Saunton Sands, England. *Sedimentology,* 35, 671-679.

Schönfeldt, H. J. (2004). Establishing the threshold for intermittent aeolian sediment transport.
Meteorologische Zeitschrift, 13(5), 437-444.

Shao, Y., & Lu, H. (2000). A simple expression for wind erosion threshold friction velocity.
Journal of Geophysical Research: Atmospheres, 105, 22437-22443.

Shao, Y., Raupach, M.R. & Findlater, P.A. (1993). Effect of saltation bombardment on the

    entrainment of dust by wind. *Journal of Geophysical Research,* 98(D7), 12719-12726.

Sherman, D. J., Bauer, B.O., Gares, P.A., & Jackson, D.W.T. (1996). Wind blown sand at

    Castroville, California. *Coastal Engineering Proceedings,* 1(25), 4214-4226.

Sherman, D. J., Jackson, D. W. T., Namikas, S. L., & Wang, J. (1998). Wind-blown sand on

    beaches: an evaluation of models. *Geomorphology*, 22(2), 113–133. doi:10.1016/S0169-

    555X(97)00062-7

Sherman, D. J. & Farrell, E. J. (2008). Aerodynamic roughness lengths over moveable beds:

    comparison of wind tunnel and field data. *Journal of Geophyiscal Research*, SI 39.

Sherman, D.J. & Li, B. (2011). Predicting aeolian sand transport rates: A re-evaluation of

    models. *Aeolian Research*, 3(4), 371-378.

Sherman, D.J., Li, B., Farrell, E.J., Ellis J.T., Cox, W.D., Maia, L.P., & Sousa, P.H.G.O. (2011).

    Measuring aeolian saltation: A comparison of sensors. *Journal of Coastal Research,* 59,

    280-290.

Sherman, D. J., Li, B., Ellis, J. T., Farrell, E. J., Maia, L. P., & Granja, H. (2013a). Recalibrating

    aeolian sand transport models. *Earth Surface Processes and Landforms*, 38(2), 169–178.

Sherman, D. J., Houser, C., Ellis, J. T., Farrell, E. J., Li, B., Davidson-Arnott, R. G. D., Baas, A.

    C. W., & Parente Maia, L. (2013b). Characterization of aeolian streamers using time-

    average videography. *Journal of Coastal Research, Special Issue 65,* 1331-1336.

Sherman, D.J., Li, B. Ellis, J.T. & Swann, C. (2014). Quantifying saltation intermittency: A

    protocol for commensurability [abstract]. *The Eighth International Conference of Aeolian*

    Research, July 2014.

Shields, A. (1936). *Application of similarity principles and turbulence research to bed-load*

    movement. Mitteilungen der Preussiischen Versuchsanstalt für Wasserbau and Schiffbau,

Berling. In: Ott, W.P. & van Uchelen, J.C. (translators), California Institute of Technology, W.M. Keck Laboratory of Hydraulics and Water Resources, Report Number 167.

Sørensen, M. (1991). An analytic model of wind-blown sand transport. *Acta Mechanica Supplement, 1,* 67-81.

Stout, J. E., & Zobeck, T. M. (1997). Intermittent saltation. *Sedimentology*, 44(5), 959–970. doi:10.1046/j.1365-3091.1997.d01-55.

Stull, R. B. (1988). *An Introduction to Boundary Layer Meteorology* (p. 666). Boston: Kluwer Acaemic Publishers.

Swann, C. M., & Sherman, D. J. (2013). A bedoad trap for aeolian sand transport. *Aeolian Research*, 11, 61–66.

Thomas, D.S.G., Knight, M., & Wiggs, G.F.S (2005). Remobilization of southern African desert dune systems by twenty-first century global warming. *Nature,* 435(7046), 1218-1221.

Tsoar, H. (1994). Classics in physical geography revisited: Bagnold, R.A. 1941: the physics of blown sand and desert dunes. *Progress in Phyiscal Geography,* 18, 91-96.

Ungar, J.E. & Haff, P.K. (1987). Steady-state saltation in air. *Sedimentology, 34,* 289-299.

van Boxel, J.H., Sterk, G. & Arens, S.M. (2004). Sonic anemometers in aeolian sediment transport research. *Geomorphology,* 59, 131-147.

Vanoni, V.A. (1964). *Measurements of critical shear stress for entraining fine sediments in a boundary layer.* California Institute of Technology, W.M. Keck Laboratory of Hydraulics and Water Resources, pp. 47.

Walker, I.J. (2005). Physical and logistical considerations of using ultrasonic anemometers in aeolian sediment transport research. *Geomorphology,* 68, 57-76.

Wang, Y., Wang, D. & Zhang, Y. (2009). Measurement of sand creep on a flat sand bed using a high-speed digital camera. *Sedimentology,* 56, 1705-1712.

Welland, M. Sediment transport by wind and water: the pioneering work of Ralph Bagnold. In:

    V. Badescu, R.B. Cathcart (Eds.), *Macro-engineering Seawater in Unique Environments*,

    Springer-Verlag, Berlin, Heidelberg, pp. 399-429.

Werner, B.T. (1990). A steady-state model of wind-blown sand transport. *The Journal of*

    Geology, 98(1), 1-17.

Werner, B.T. & Haff, P.K. (1988). The impact process in aeolian saltation: two-dimensional

    simulations. *Sedimentology,* 35(2), 189-196.

Wiberg, P.L. & Smith, D.S. (1987). Calculations of the critical shear stress for motion of uniform

    and heterogeneous sediments. *Water Resources Research,* 23(8), 1471-1480.

Wiggs, G. F. S., Baird, A.J. & Atherton, R.J. (2004a). The dynamic effects of moisture on the

    entrainment and transport of sand by wind. *Geomorphology,* 59(1), 13-30.

Wiggs, G. F. S., Atherton, R. J., & Baird, A. J. (2004b). Thresholds of aeolian sand transport:

    establishing suitable values. *Sedimentology*, 51(1), 95–108.

Wilcock, P.R., (1988). Methods for estimating the critical shear stress of individual fractions in

    mixed-size sediment. *Water Resources Research,* 24(7), 1127-1135.

Wilcock, P.R. (1993). Critical shear stress of natural sediments. *Journal of Hydraulic*

    Engineering, 119(4), 491-505.

Wilcock, P.R. & Southard, J.B. (1988). Experimental study of incipient motion in mixed-size

    sediment. *Water Resources Research,* 24(7), 1137-1151.

Wilkinson, R. H. (1984). A Method for Evaluating Statistical Errors Associated with

    Logarithmic Velocity Profiles, *GEO-MARINE Letters* 3(5), 49–52.

Willetts, B.B. (1983). Transport by wind of granular material of different grain shapes and

    densities. *Sedimentology,* 30(5), 669-679.

Willetts, B.B. & Rice, M.A. (1989). Collisions of quartz grains with a sand bed: the influence of

    incident angle. *Earth Surface Processes and Landforms,* 14(8), 719-730.

Williams, J. J., Butterfield, G. R., & Clark, D. G. (1990). Rates of aerodynamic entrainment in a

    developing boundary layer. *Sedimentology,* 37, 1039-1048.

Williams, J. J., Butterfield, G. R., & Clark, D. G. (1994). Aerodynamic entrainment threshold:

    effects of boundary layer flow conditions. *Sedimentology,* 41, 309-328.

Zhang, K., Qu, J., Han, Q. & An, Z. (2012). Wind energy environments and aeolian sand

    characteristics along the Qinghai-Tibet Railway, China. *Sedimentary Geology,* 273, 91-96.

Zingg, A. W. (1953). Wind tunnel studies of the movement of sedimentary material. *Proceedings*

    of the 5th Hyraulic Conference Bulletin, 34, 111–135.

Zobeck, T.M., & van Pelt, S.V. (2006). Wind-induced dust generation and transport mechanics

    on a bare agricultural field. *Journal of Hazardous Materials,* 132(1), 26-38.